UNIVERSITÀ DEGLI STUDI DI PADOVA

Dipartimento di Fisica e Astronomia "Galileo Galilei"

Master Degree in Physics

Final Dissertation

The marked power spectrum of cosmological large scale structure

Thesis supervisor

Prof. Michele Liguori

Thesis co-supervisor

Dr. Marco Marinucci

Candidate

Luca Fusaro

Academic Year 2024/2025

A chi è in questo viaggio con me,
vicino o lontano, oggi o ieri.
Perché è nella condivisione che ogni cammino trova il suo senso.

Acknowledgements

I would like to thank my supervisor, Prof. *Michele Liguori*, and my co-supervisor, Dr. *Marco Marinucci*, for their guidance and constant support throughout the development of this thesis.

I am grateful to *Francisco Villaescusa-Navarro* for providing the simulations used to validate the code I developed.

A special thank you goes to my *family and friends*: I am truly grateful to have them as part of my journey. Their presence has made this path *unique* and undoubtedly *more meaningful*.

Abstract

Understanding the large-scale structure (LSS) of the universe is key to constraining fundamental physics, including the nature of inflation and primordial non-Gaussianity (PNG). This thesis begins with a theoretical review of cosmological structure formation, including perturbative modeling of the power spectrum at one-loop order and the bispectrum at tree level. Building on this foundation, we focus on the marked power spectrum—a modified two-point statistic that incorporates local environmental information by weighting cosmic tracers. While a perturbative model for this observable has been proposed in recent literature, in this work we extend it to include the effects of non-local PNG in redshift space.

A full numerical implementation of the model was developed and validated using measurements from the Quijote simulations, showing excellent agreement up to mildly non-linear scales. This implementation is then used to perform a Fisher forecast for a BOSS-like survey. We assess the constraining power of the combined power spectrum and marked power spectrum, showing that this approach can improve sensitivity to non-local PNG. In contrast to the bispectrum, the marked power spectrum—being a two-point correlation function—offers a more tractable alternative, with reduced sensitivity to observational systematics and covariance modeling. These results highlight the marked power spectrum as a promising and complementary probe for extracting non-Gaussian information from upcoming large-scale structure surveys.

Contents

Thesis Overview

In recent years, cosmology has entered an era of precision, thanks to the wealth of high-quality data from galaxy surveys, the cosmic microwave background, and gravitational lensing. Future and on going experiments such as Euclid [1], DESI [2] and the Vera C. Rubin Observatory's LSST [3] will map the large-scale structure of the Universe across unprecedented volumes and redshifts. These surveys are expected to significantly improve our ability to test fundamental physics — from neutrino masses to the nature of dark energy and dark matter the properties of the initial conditions of the Universe.

To match the observational progress, there is a growing need for theoretical tools that can extract cosmological information from the mildly nonlinear regime, where most of the signal resides. This is particularly relevant for detecting subtle imprints of the early Universe, such as *primordial non-Gaussianity* (PNG), which cannot be fully captured by standard two-point statistics and therefore require higher-order correlators for their characterization.

Understanding the large-scale structure of the Universe is a fundamental challenge in modern cosmology. The evolution of cosmic structures, driven by gravitational instability, plays a crucial role in shaping the observable Universe. Over the past few decades, both analytical and numerical techniques have significantly advanced our understanding of structure formation, refining key physical principles and cosmological parameters.

One of the most powerful tools for studying large-scale structure is the *power spectrum*, the Fourier transform of the two-point correlation function, which quantifies the statistical distribution of matter fluctuations. However, higher-order correlators such as the *bispectrum*, the Fourier transform of the three-point correlation function, contain additional information and are essential for constraining deviations from Gaussianity in the early Uni-

verse. Despite their theoretical importance, the practical implementation of the bispectrum beyond leading perturbative order becomes increasingly complex. An alternative approach involves modifying the traditional two-point correlator through the *marked density field*, which incorporates local density weighting to enhance sensitivity to nonlinear structure formation. This technique offers a novel and promising way to extract additional cosmological information.

This thesis explores the development and application of *perturbation theory in cosmology*, focusing on the *marked power spectrum* for galaxies and its implementation in both real and redshift space. Furthermore, it examines the effects of *primordial non-Gaussianity of the non-local type* on the marked power spectrum. The numerical implementation of the model, previously validated against measurements from the *Quijote* suite, a dark matter only set of N-body simulations, is then used to perform a Fisher forecast, providing an estimate of the statistical constraints achievable with this approach.

- **Chapter 1** introduces fundamental concepts in cosmology, including the *Cosmological Principle*, the geometry of spacetime, and the *Friedmann equations*. The thermal history of the universe is outlined, highlighting key epochs such as *nucleosynthesis* and *recombination*. The concept of *cosmic inflation* is discussed as a solution to the horizon and flatness problems, and as the mechanism responsible for generating the primordial fluctuations that seed large-scale structure.

- **Chapter 2** focuses on the *theory of gravitational instability*, which describes the formation of cosmic structures from primordial density fluctuations. The *Vlasov equation* and its implications for the evolution of collisionless dark matter are examined. *Perturbation theory* is introduced to describe the evolution of density fields, starting with the standard *Eulerian framework* and extending beyond the pressureless perfect fluid approximation by incorporating the *stress tensor, a momentum cutoff, and additional corrective terms*. Additionally, observational challenges such as *galaxy bias* and *redshift-space distortions* are discussed. Key statistical tools, including the *power spectrum* and *bispectrum*, are presented in detail.

- **Chapter 3** introduces the concept of *marked density fields* as a method to enhance sensitivity to non-Gaussian features in the matter distribution. The perturbative framework for marked density fields is devel-

oped, incorporating effects such as *biases, small- corrections, and shot noise*. For the first time, this work includes the contribution of *primordial non-Gaussianity of the non-local type*—specifically equilateral and orthogonal shapes—within the marked power spectrum in redshift space, accounting for all relevant terms in the perturbative expansion. The chapter also presents numerical evaluations of the marked power spectrum in both *real and redshift space*, based on a dedicated code developed for this thesis, which computes the full expression of the marked power spectrum including primordial non-Gaussianity effects.

- **Chapter 4** focuses on the *Fisher matrix formalism*, a powerful statistical tool to forecast the constraining power on cosmological parameters. The chapter begins with a validation of the theoretical model and its numerical implementation using measurements from the *Quijote* simulations. The *Cramér-Rao bound* is then introduced as a means to quantify the precision of parameter estimates. Fisher forecasts for a *BOSS-like survey* are performed, comparing the results obtained when using the *power spectrum plus marked power spectrum* as observables, instead of the traditional *power spectrum plus bispectrum* approach.

- **Chapter 5** presents the conclusions of this work. It summarizes the main theoretical and numerical developments, including the extension of the perturbative model for the marked power spectrum to incorporate non-local PNG in redshift space, and the validation of the implementation using *Quijote* simulations. The chapter discusses the Fisher forecast results, highlighting the advantages and practical relevance of marked statistics as complementary observables to the standard power spectrum and bispectrum. Limitations of the current framework are acknowledged, and future research directions are proposed, including the treatment of observational effects and the use of optimization techniques to enhance the information content of marked statistics.

This thesis aims to advance our understanding of cosmic structure formation through *analytical techniques, statistical modeling, and numerical implementation*. By refining perturbation theory predictions and incorporating marked density fields, this work contributes to the ongoing effort to *maximize the information extracted from upcoming large-scale structure surveys*.

Chapter 1

Introduction to cosmology and inflation

1.1 The Cosmological Principle

The Cosmological Principle forms the cornerstone of modern cosmology. It states that, on large scales, the universe appears the same regardless of an observer's position (*homogeneity*) or direction (*isotropy*). Formally, this can be expressed as:

> *Every comoving observer sees the Universe, at a fixed time in their reference frame, as homogeneous and isotropic.*

A comoving observer moves coherently with the cosmic fluid, which defines the universe's absolute reference frame. Observations of the *Cosmic Microwave Background* (CMB) support this idea. The CMB is observed as blackbody radiation with a temperature of $T_{\mathrm{CMB}} \approx 2.725\,\mathrm{K}$, but it also exhibits a dipole anisotropy of $\Delta T \approx 3.4\,\mathrm{mK}$ [4]. This dipole is caused by the Doppler effect, due to the Solar System's motion relative to the CMB. From this dipole, the Solar System's velocity relative to the CMB can be estimated as approximately 370 km/s. The Local Group, which includes the Milky Way, also moves relative to the CMB at roughly 620 km/s [4]. The absolute reference frame of the universe is thus experimentally defined as the frame in which the CMB dipole vanishes. Beyond this dipole anisotropy, the CMB is remarkably uniform. However, it contains very small anisotropies, with temperature variations of the order of $\Delta T/T \sim 10^{-5}$, that reflect the

primordial fluctuations that seeded the large-scale structure of the universe. The word "time" in fixed time refers to the proper time of a comoving observer, which is called *cosmic time*.
In summary, while the Cosmological Principle is expected to hold on very large scales, smaller scales reveal deviations due to local structures. Observational isotropy, combined with the assumption that we are typical observers, leads to the inference of homogeneity.

1.2 The geometry of spacetime

The most general form of a metric consistent with the universe being homogeneous and isotropic is given by the *Friedmann–Lemaître-Robertson-Walker* (FLRW) *metric*:

$$ds^2 = -c^2dt^2 + a(t)^2\left(\frac{dr^2}{1-kr^2} + r^2d\Omega^2\right), \tag{1.2.1}$$

with $d\Omega = d\theta^2 + sin^2(\theta)\, d\phi^2$ the angular part of the metric tensor on a unit sphere. The parameter k is a constant describing the spatial curvature, which can always be normalized to ± 1 or 0 with $k = 0$, $k = +1$, and $k = -1$ for flat, positively curved, and negatively curved space-like 3-hypersurfaces, respectively. It is important to notice that we can choose the normalization of k, but its sign is a constant.

$a(t)$ is called *scale factor* and incorporates the expansion of the universe, so that the relation between comoving coordinate (that doesn't change in time) and physical coordinate is given by

$$\lambda_{phys} = a(t)\,\lambda_{com} \tag{1.2.2}$$

We can introduce the conformal time τ, defined by

$$d\tau = \frac{dt}{a(t)}, \tag{1.2.3}$$

and with this time coordinate the metric can be written as

$$ds^2 = a(\tau)^2\left[-c^2d\tau^2 + \left(\frac{dr^2}{1-kr^2} + r^2d\Omega^2\right)\right]. \tag{1.2.4}$$

If we set $k = 0$ we obtain the Minkowski metric multiplied by the squared scale factor, making the propagation of light (null geodesic, $ds^2 = 0$) similar in the two metrics.

1.3 Friedmann equations

The dynamics of the universe evolution are determined by the Einstein equations (EE):

$$G_{\mu\nu} = R_{\mu\nu} - \frac{1}{2} g_{\mu\nu} R = 8\pi G\, T_{\mu\nu} \tag{1.3.1}$$

This relates the Einstein tensor $G_{\mu\nu}$, which is a measure of the "space-time curvature" of the FRW universe, to the stress-energy tensor where $T_{\mu\nu}$ describes the matter and energy content of the universe. $R_{\mu\nu}$ is the Ricci tensor, the contraction of the Riemann tensor, while R is the Ricci curvature scalar, defined again as the contraction of the Ricci tensor:

$$R_{\mu\nu} = g^{\rho\sigma} R_{\mu\rho\nu\sigma} \tag{1.3.2}$$

$$R = g^{\mu\nu} R_{\mu\nu} \tag{1.3.3}$$

The Riemann tensor is defined as

$$R^{\rho}_{\mu\sigma\nu} \equiv \frac{\partial \Gamma^{\rho}_{\mu\nu}}{\partial x^{\sigma}} - \frac{\partial \Gamma^{\rho}_{\mu\sigma}}{\partial x^{\nu}} + \Gamma^{\eta}_{\mu\nu}\Gamma^{\rho}_{\sigma\eta} - \Gamma^{\eta}_{\mu\sigma}\Gamma^{\rho}_{\nu\eta}, \tag{1.3.4}$$

where we define the Christoffel symbols as

$$\Gamma^{\rho}_{\mu\nu} = \frac{1}{2} g^{\rho\sigma} \left(\partial_{\mu} g_{\sigma\nu} + \partial_{\nu} g_{\sigma\mu} - \partial_{\sigma} g_{\mu\nu} \right). \tag{1.3.5}$$

Imposing the conditions of homogeneity and isotropy, the universe, on large scales, can be modeled as a perfect fluid. A perfect fluid is characterized by uniform properties such as energy density (ρ) and pressure (P), and no shear stress, viscosity, or heat conduction (i.e., it is "perfect"). Under the assumptions of homogeneity and isotropy the large-scale universe cannot support directional shear or flow irregularities because such features would violate isotropy. Likewise, gradients in density or pressure (which lead to complex flows) are incompatible with homogeneity. The form of the stress-tensor for a perfect fluid is [5]:

$$T_{\mu\nu} = (\rho + P)\, u_{\mu} u_{\nu} + P\, g_{\mu\nu} \tag{1.3.6}$$

where u_{μ} is the 4-velocity of the fluid element and in the comoving frame $u_{\mu} = (-1, \vec{0})$, $P = P(t)$ is the isotropic pressure and $\rho = \rho(t)$ is the background

matter-energy density.
So we obtain in the comoving frame:

$$T^{\mu}_{\nu} = \begin{bmatrix} -\rho & 0 & 0 & 0 \\ 0 & P & 0 & 0 \\ 0 & 0 & P & 0 \\ 0 & 0 & 0 & P \end{bmatrix} \tag{1.3.7}$$

that reflects the structure of the FLRW metric tensor $g_{\mu\nu}$.

From EE, (1.3.1), we get the first two independent Friedmann equations:

$$H^2 = \frac{8\pi G}{3}\rho - \frac{k}{a^2} \tag{1.3.8}$$

$$\frac{\ddot{a}}{a} = -\frac{4\pi G}{3}(\rho + 3P) \tag{1.3.9}$$

where $H = H(t) = \frac{\dot{a}(t)}{a(t)}$ is the Hubble parameter, a measure of the expansion rate of the universe, measured in $Km \cdot s^{-1} \cdot Mpc^{-1}$.

If we take the covariant divergence of the Einstein tensor $G_{\mu\nu}$ we get zero; so the stress-energy tensor must also have $\nabla_{\mu} T^{\mu\nu} = 0$. From this equation we get the third Friedmann equation:

$$\dot{\rho} = -3H(\rho + P) \tag{1.3.10}$$

These three equations are not independent, while (1.3.9) defines the dynamic of the system, equations (1.3.8) and (1.3.10) are just constraining equations. In the end we have three independent variables ($a(t)$, $\rho(t)$ and $p(t)$) but only two equations. We introduce the *equation of state* of the cosmic fluid, that relates ρ to P, and that take the general form

$$P = w\,\rho, \tag{1.3.11}$$

Plugging it in (1.3.10) we get:

$$\frac{\log \rho}{\log a} = -3(1+w) \implies \rho \propto a^{-3(1+w)} \tag{1.3.12}$$

The parameter w takes different values depending on which kind of matter/energy we are considering. In particular we have $w = 0$ for ordinary matter (with null or negligible pressure), $w = 1/3$ for radiation and $w = -1$

when the universe is dominated by an exotic fluid with constant energy density (*cosmological constant*). So we have:

$$\rho(a) \propto \begin{cases} a^{-4}, & \text{radiation: } w = \frac{1}{3}, \\ a^{-3}, & \text{matter: } w = 0, \\ \text{constant}, & \text{dark energy: } w = -1. \end{cases} \tag{1.3.13}$$

The decrease of the energy density of matter particles is only due to the expansion of universe, because the average number of particles per unit volume decreases ($V \propto a^3$). For relativistic particles we have to take in account also the relativistic Doppler shift, which increases the negative power of the scaling factor by one. Now, assuming for simplicity a flat universe and combining (1.3.12) with the first (1.3.8) and third (1.3.10) Friedmann equations we get the time dependence of the scale factor, energy density and Hubble parameter:

$$a(t) = a_0 \left[1 + \frac{3}{2}(1+w)H_0(t-t_0)\right]^{\frac{2}{3(1+w)}}. \tag{1.3.14}$$

$$\rho(t) = \rho_0 \left[1 + \frac{3}{2}(1+w)H_0(t-t_0)\right]^{-2}. \tag{1.3.15}$$

$$H(t) = H_0 \left[1 + \frac{3}{2}(1+w)H_0(t-t_0)\right]^{-1}. \tag{1.3.16}$$

These solutions are valid for $w \neq -1$. H_0 and a_0 are the Hubble and scale parameters defined at the time t_0, usually set as the present time.
Introducing the Big Bang time t_{BB}:

$$t_{BB} - t_0 = -\frac{2}{3H_0(1+w)}. \tag{1.3.17}$$

Defining the new time parameter $t' = t - t_{BB}$:

$$a(t') = a_0 \left[\frac{3}{2}(1+w)H_0 t'\right]^{\frac{2}{3(1+w)}}. \tag{1.3.18}$$

$$\rho(t') = \rho_0 \left[\frac{3}{2}(1+w)H_0 t'\right]^{-2}. \tag{1.3.19}$$

$$H(t') = \left[\frac{3}{2}(1+w)t'\right]^{-1}. \tag{1.3.20}$$

At $t' = 0$ ($t = t_{BB}$), the following limits hold:

$$a(t) \to 0, \quad \rho(t) \to \infty, \quad H(t) \to \infty. \tag{1.3.21}$$

This initial configuration of infinite energy density corresponds to the Big Bang.

The cosmological constant

When Einstein formulated his general theory of relativity, the prevailing belief was that the universe was static. However, the Friedmann equations derived from general relativity revealed that such a universe could not be static unless the acceleration of the scale factor, $\ddot{a}(t)$, was zero. This implied a peculiar relationship between the energy density ρ and pressure P:

$$\rho = -3P. \tag{1.3.22}$$

Since this condition seemed physically implausible, Einstein introduced the cosmological constant Λ to modify the Einstein field equations:

$$R_{\mu\nu} - \frac{1}{2} g_{\mu\nu} R = 8\pi G T_{\mu\nu} - \Lambda g_{\mu\nu}. \tag{1.3.23}$$

One can obtain a static solution with an appropriate choice of Λ. To rewrite the stress-energy tensor in a more compact form, Λ was incorporated into an effective stress-energy tensor:

$$\bar{T}_{\mu\nu} = T_{\mu\nu} - \frac{\Lambda}{8\pi G} g_{\mu\nu}. \tag{1.3.24}$$

This effective tensor can be expressed as:

$$\bar{T}_{\mu\nu} = (\bar{P} + \bar{\rho}) u_\mu u_\nu + \bar{P} g_{\mu\nu}, \tag{1.3.25}$$

where $\bar{P}$ and $\bar{\rho}$ are the effective pressure and density, related to their original counterparts by:

$$\bar{P} = P - \frac{\Lambda}{8\pi G}, \tag{1.3.26}$$

$$\bar{\rho} = \rho + \frac{\Lambda}{8\pi G}. \tag{1.3.27}$$

Following the discovery of the expanding universe in the late 1920s, the need for a cosmological constant to support a static universe disappeared. However, Λ has regained importance as the simplest explanation for the observed accelerated expansion of the universe. The modern cosmological model incorporating Λ is known as the ΛCDM model.

One specific cosmological model featuring Λ is the *de Sitter Universe*. In this model, the universe is dominated by a positive cosmological constant, with negligible contributions from matter and radiation. Under these conditions:

$$P = -\rho = -\frac{\Lambda}{8\pi G}, \tag{1.3.28}$$

that is the case we obtain setting $w = -1$ in the equation of state.

Substituting these relations into the Friedmann equation we find:

$$H^2 = \frac{\Lambda}{3}, \tag{1.3.29}$$

indicating a constant Hubble parameter H. The corresponding solution for the scale factor is:

$$a(t) \propto \exp\left(\sqrt{\frac{\Lambda}{3}}t\right). \tag{1.3.30}$$

This exponential expansion describes the repulsive gravitational effect of the positive cosmological constant.

1.4 Thermal history of the Universe

The thermal history of the Universe describes its evolution with temperature, which in turn reflects its energy density, particle content, and dominant interactions. We begin by considering the phase space distribution function $f(\mathbf{x}, \mathbf{p}, t, \mu)$, where μ is the chemical potential. Thanks to the Cosmological Principle and using the relation $E^2 = p^2 + m^2$ and considering that time and temperature are related as we will see shortly:

$$f(\mathbf{x}, \mathbf{p}, t, \mu) = f(p, t, \mu) = f(E, T, \mu). \tag{1.4.1}$$

This is the probability density of finding a particle with energy E and temperature T. If we assume to be at the thermodynamic equilibrium, f will

just be the statistical distribution of the considered particle species, either fermionic or bosonic:

$$f(\mathbf{q}, T, \mu) = \left[e^{\frac{E-\mu}{T}} \mp 1 \right]^{-1} \tag{1.4.2}$$

where $-$ stand for bosons and $+$ for fermions.

Then we introduce the particle number density

$$n(T, \mu) = \frac{g}{(2\pi)^3} \int f(E, T, \mu)\, d^3q \tag{1.4.3}$$

where g is the number of internal degrees of freedom for a particular particle species. For the energy density we have:

$$\rho(T, \mu) = \frac{g}{(2\pi)^3} \int E(\mathbf{q}) f(E, T, \mu)\, d^3q, \tag{1.4.4}$$

while the pressure is

$$P(T, \mu) = \frac{g}{(2\pi)^3} \int \frac{q^2}{3E(\mathbf{q})} f(E, T, \mu)\, d^3q, \tag{1.4.5}$$

Solving the integrals in the relativistic case ($T \gg m$) we obtain:

$$n(T) = \begin{cases} \frac{g\zeta(3)}{\pi^2} T^3 & \text{(Bosons)}, \\ \\ \frac{3}{4} \frac{g\zeta(3)}{\pi^2} T^3 & \text{(Fermions)}, \end{cases}$$

$$\rho(T) = \begin{cases} \frac{g\pi^2}{30} T^4 & \text{(Bosons)}, \\ \\ \frac{7}{8} \frac{g\pi^2}{30} T^4 & \text{(Fermions)}. \end{cases} \tag{1.4.6}$$

and $P = \frac{\rho}{3}$ as can be expected for a relativistic fluid.

In the non-relativistic case ($T \ll m$), the particle number density is significantly suppressed as:

$$n(T) \sim e^{-\frac{m}{T}} \tag{1.4.7}$$

The energy density and pressure follow the same behavior since:

$$\rho(T) = mn(T), \tag{1.4.8}$$

$$p(T) = n(T)T. \tag{1.4.9}$$

The early universe's thermal history can be understood by considering the evolution of temperature T with the scale factor $a(t)$. Conservation of entropy in an expanding universe gives [6]:

$$T \sim a^{-1} \tag{1.4.10}$$

Using the definition of the cosmic redshift:

$$1 + z = \frac{\lambda_o}{\lambda_e} = \frac{a_0}{a_e} = \frac{1}{a_e}, \tag{1.4.11}$$

where e denotes emitted and o denotes observed states, it follows that:

$$T \sim 1 + z. \tag{1.4.12}$$

This implies that as we move backward in time, the universe becomes hotter and denser. This forms the basis of the "Hot Big Bang" model. Some key points of the thermal history of the universe are represented in Fig.1.1 and are briefly described in the following:

1. **Baryogenesis**: During the radiation era at very high temperatures, a slight asymmetry between matter and antimatter led to the predominance of matter after annihilation processes. The universe was dominated by radiation, with energy primarily in the form of photons, neutrinos, and other relativistic particles.

2. **Neutrino Decoupling**: Around $T \sim 1$ MeV, neutrinos stopped interacting with other particles and began free-streaming.

3. **Big Bang Nucleosynthesis (BBN)**: At $T \sim 100$ keV, protons and neutrons fused to form light nuclei such as hydrogen, helium, and lithium, leaving an imprint on the chemical composition of the universe.

4. **Recombination**: At $T \sim 3000$ K ($z \sim 1100$), electrons and protons combined to form neutral hydrogen. This transition made the universe transparent to photons and defined the last scattering surface. The radiation emitted at this time has since cooled due to the universe's expansion and now forms the Cosmic Microwave Background (CMB) we observe today.

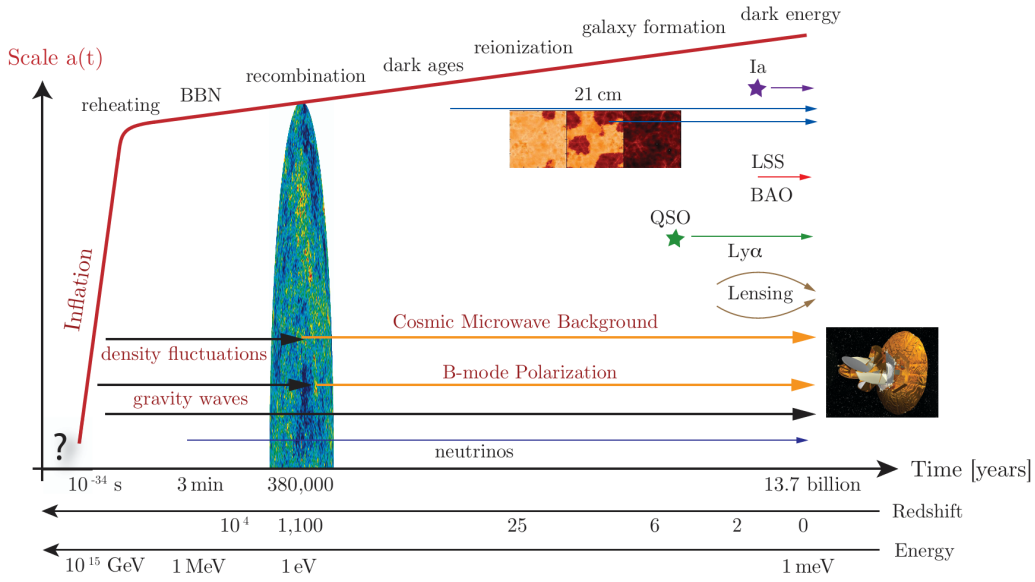

Figure 1.1: A schematic representation of the thermal history of the universe, illustrating key epochs and transitions. The timeline spans from inflation and reheating, through Big Bang nucleosynthesis (BBN), recombination, and the formation of the Cosmic Microwave Background (CMB), to later stages such as galaxy formation, reionization, and the onset of dark energy dominance. The evolution of the scale factor $a(t)$ is shown, highlighting the exponential growth during inflation and subsequent slower growth in later epochs. The image also connects observable signatures, such as CMB fluctuations, B-mode polarization, large-scale structure (LSS), and gravitational lensing, to their corresponding stages in cosmic history. This image is taken from [7].

5. **Structure Formation**: Following recombination, the universe entered the matter-dominated era. Gravitational instability during this epoch led to the formation of galaxies and large-scale structures.

6. **Dark Energy Domination**: At recent times ($z \sim 0.7$), the universe transitioned to the dark energy era, with dark energy driving its accelerated expansion.

This thermal evolution provides the framework for our understanding of cosmology and the observable universe.

1.5 The Energy Budget of the Universe

The Friedmann equations allow us to consider the contributions of various components to the universe's energy budget. We define the critical energy density as the one we obtain imposing the flat universe ($k = 0$ condition in the first Friedmann equation:

$$\rho_{\text{crit}} = \frac{3H^2}{8\pi G}. \tag{1.5.1}$$

We introduce the dimensionless density parameters:

$$\Omega_x \equiv \frac{\rho_x}{\rho_{\text{crit}}}, \tag{1.5.2}$$

where x stands for different components of the universe (e.g., radiation, matter, curvature, and dark energy). The Friedmann equation can then be rewritten as:

$$H^2(a) = H_0^2 \left[\Omega_{r,0} \left(\frac{a_0}{a} \right)^4 + \Omega_{m,0} \left(\frac{a_0}{a} \right)^3 + \Omega_{k,0} \left(\frac{a_0}{a} \right)^2 + \Omega_{\Lambda,0} \right], \tag{1.5.3}$$

where the 0-subscript represents the value at the present time. For simplicity, we drop the subscript 0 and normalize the scale factor today as $a(t_0) = 1$. This reduces the equation to:

$$\frac{H^2}{H_0^2} = \Omega_r a^{-4} + \Omega_m a^{-3} + \Omega_k a^{-2} + \Omega_\Lambda. \tag{1.5.4}$$

Evaluating the equation at the present time t_0 we obtain:

$$\Omega_{\text{total}} = \Omega_r + \Omega_m + \Omega_k + \Omega_\Lambda = 1. \tag{1.5.5}$$

This equation implies that the density parameter Ω_{total} represents the total energy content of the universe. Matter contribute is divided into baryonic matter, which consists of ordinary atoms forming stars, planets, and gas, and dark matter, an invisible, non-luminous component detectable only through its gravitational effects. The Planck sateliite mission's constraints the values for the density parameters at 68% confidence level [8]:

$$\Omega_b = 0.0490 \pm 0.0003, \tag{1.5.6}$$

$$\Omega_{cdm} = 0.2607 \pm 0.0020, \tag{1.5.7}$$

$$\Omega_\Lambda = 0.6889 \pm 0.0056, \tag{1.5.8}$$

$$\Omega_k = 0.001 \pm 0.002, \tag{1.5.9}$$

while radiation is negligible at present. As we see, curvature contributes less than 1% of the total energy budget. The baryonic matter density is constrained by observations of primordial nucleosynthesis, which relies on the density of protons and neutrons in the early universe. This affects the efficiency of fusion processes and determines the abundance of light elements. The remaining matter is cold dark matter Ω_{cdm}, one of the most enigmatic substances in the universe. Dark matter is classified as "cold" or "hot" based on its thermal motion at the time of decoupling in the early universe. Cold dark matter refers to non-relativistic particles moving slowly compared to the speed of light, whereas hot dark matter consists of relativistic particles, such as neutrinos, moving close to the speed of light. This distinction is crucial because cold dark matter clusters gravitationally, forming the seeds of large-scale structures in the universe, while hot dark matter, due to its high velocities, cannot efficiently form such structures. The ΛCDM model, on which the Planck mission is based, assumes that the dominant dark matter component is cold dark matter. This assumption provides the best fit to observed large-scale structures, the Cosmic Microwave Background (CMB) anisotropies, and galaxy distributions. Radiation energy density primarily arises from photons in the cosmic microwave background (CMB). However, experiments such as Planck have detected additional contributions from relativistic particles, consistent with the expected cosmic neutrino background.

1.6 Horizons and Cosmological Issues

As we have discussed, the Big Bang theory provides remarkable predictions, such as nucleosynthesis and the Cosmic Microwave Background, that are strongly supported by observational evidence. However, within the framework of this model, certain fundamental issues arise, particularly regarding the initial conditions of the universe. To address these challenges, we first need to introduce some key concepts.

Particle and Hubble horizons

The causal connection between points in space-time is determined by their position relative to each other's lightcone. Lightcones are defined by the

condition $ds^2 = 0$, where ds^2 represents, as usual, the space-time interval between two events. In essence, the lightcone of an event encompasses all other events that could potentially receive or send signals to it, assuming the signals travel at or below the speed of light. Events within the past lightcone of a given event can be causally influenced by it, while events outside its future lightcone lie beyond its causal reach. Considering the FLRW metric and the isotropy, that allow us to fix the angle variables and set $d\Omega = 0$, and imposing $ds^2 = 0$ we get:

$$\frac{dt}{a(t)} = \frac{dr}{\sqrt{1 - k\,r}}. \tag{1.6.1}$$

So, we define the comoving particle horizon as:

$$r_H(t) = \int_0^t \frac{dt'}{a(t')} \tag{1.6.2}$$

To obtain the physical distance we simply multiply the comoving quantity with the scale factor:

$$d_H(t) = a(t)\, r_H(t) \tag{1.6.3}$$

If two points are separated by a distance greater than $d_H(t)$ then they have never been in causal connection. Remembering Eq.(1.3.18), we know that $a(t) \propto t^\alpha$ with $\alpha = \frac{2}{3(1+w)}$, so we see that the above integral converges if $\alpha < 1$, i.e. if $w > -1/3$, and in this case we obtain:

$$d_H(t) = \frac{3(1+w)}{3w+1} t \tag{1.6.4}$$

The condition $w > -1/3$ implies, through the 2^{nd} Friedmann equation (1.3.9), that $\ddot{a} < 0$, meaning that we have a finite particle horizon only in the case of a decelerating universe.

Now, let's define the Hubble time as $\tau_H \equiv H^{-1}$. Remembering that H can be interpreted as the expansion rate of the Universe, τ_H can be seen as the characteristic time of expansion of the universe. Hence, the Hubble radius, in natural units, is given by:

$$R_H(t) = \tau_H = H^{-1}(t), \tag{1.6.5}$$

which represents the distance traveled by a photon in a Hubble time. The comoving Hubble radius is then:

$$r_H(t) = \frac{R_H(t)}{a(t)} = (aH)^{-1} = \frac{1}{\dot{a}(t)} \tag{1.6.6}$$

The Hubble radius represents the distance light or particles can travel within one Hubble time (the characteristic expansion time of the universe). It indicates whether two particles, separated by a certain comoving distance can causally communicate at the current time. In contrast, the particle horizon defines the maximum distance from which light or signals could have traveled to us since the beginning of the universe. It represents the cumulative extent of causal connection over the entire history of the universe. While both the Hubble radius and the particle horizon relate to causal connectivity, they differ conceptually: the Hubble radius concerns the present ability of particles to communicate, whereas the particle horizon measures the ultimate reach of signals over cosmic time Changing variable we can relate the particle horizon with the Hubble horizon:

$$d_H(t) = a(t) \int_0^t \frac{dt'}{a(t')} = a(t) \int_0^a \frac{da'}{a'} \frac{1}{\dot{a}'} = a(t) \int_0^a d(\log a)\, r_H, \qquad (1.6.7)$$

so the particle horizon is given by the logarithmic integral of the Hubble horizon. Comparing (1.3.20) with (1.6.4) we can easily see that, despite their conceptual difference, the Hubble horizon and the particle horizon have nearly the same value, differing only by a factor on the order of $\sim \mathcal{O}(1)$.

The Horizon, Flatness, and Unwanted Relic Problems

Let us now examine the challenges posed by the Hot Big Bang model and explore how they are addressed by the inflationary paradigm. One of the key issues is the **horizon problem**. A region of the universe with a characteristic length λ can only be causally connected, i.e. the particles within that region were in causal contact, if $\lambda < r_H$, where r_H is the comoving Hubble horizon. In simpler terms, regions separated by a distance greater than the Hubble horizon cannot have exchanged information or signals. At a specific time t_H, a region with $\lambda = r_H$ becomes causally connected. Before this time, regions with $\lambda > r_H$ would remain disconnected. Given the ongoing expansion of the universe, this suggests that some regions of the universe have only recently come into causal connection. However, observations of the Cosmic Microwave Background (CMB) reveal a remarkable homogeneity and isotropy across the entire visible universe, with temperature fluctuations of the order $\frac{\Delta T}{T} \approx 10^{-5}$, which implies that these regions must have been in causal contact in the past. How can this be, given their apparent disconnection? The inflationary model provides an elegant solution to this problem. Prior to the

radiation-dominated era, there was a phase during which the Hubble horizon $r_H(t)$ decreased over time ($\dot{r}_H(t) < 0$). This contraction of the comoving Hubble horizon, as illustrated in Fig.1.2, ensured that regions of the universe which have only recently come into causal contact were actually causally connected during the very early universe. This early connection allowed particles in those regions to interact and exchange information, leading to the homogeneous and isotropic conditions we observe today. We can see

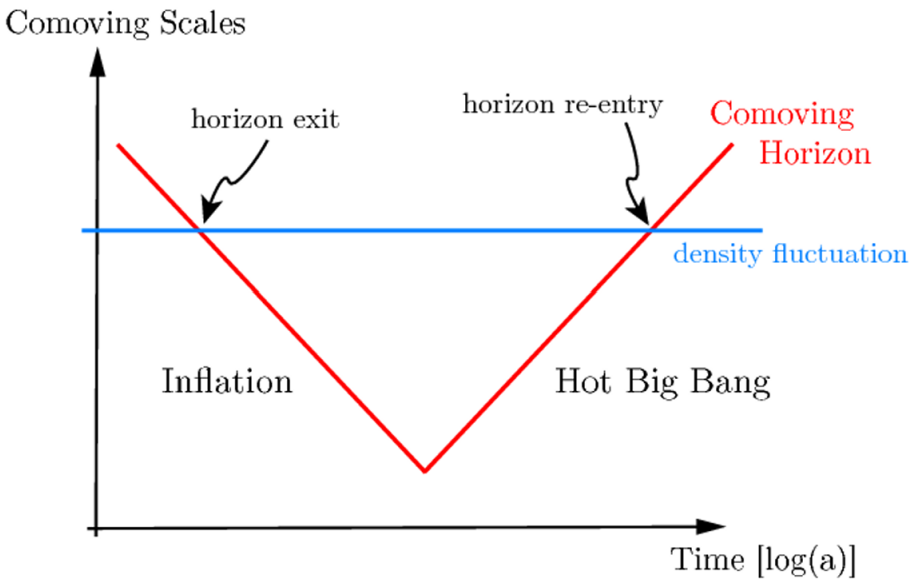

Figure 1.2: A schematic representation of the comoving horizon (red line) and the evolution of density fluctuations (blue line) during the inflationary and Hot Big Bang epochs. During inflation, the comoving horizon shrinks, allowing density fluctuations to exit the horizon (horizon exit). After inflation ends, during the Hot Big Bang phase, the comoving horizon grows, causing these fluctuations to re-enter the horizon (horizon re-entry). Figure from [7].

that assuming a decreasing Hubble horizon means assuming an epoch of accelerated expansion:

$$\dot{r}_H = -\frac{\ddot{a}}{a^2} < 0 \implies \ddot{a} > 0 \tag{1.6.8}$$

So we call *inflation* an epoch of the early universe where the expansion is accelerated. Now, we have to impose a condition on the duration of the

inflation such that at least what we observe today has entered in causal connection during the inflationary period, so we require:

$$r_H(t_i) \geq r_H(t_0), \tag{1.6.9}$$

where t_i is the beginning time of inflation. Looking at the 2^{nd} Friedmann equation (1.3.9), we see that the condition (1.6.9) corresponds to have:

$$P < -\frac{\rho}{3}, \tag{1.6.10}$$

i.e. a negative pressure. As we have seen before, the case of an exotic fluid with constant energy density and $w = -1$ is compatible with this condition. In this case we have a constant Hubble factor and an exponentially growing in time scale factor $a(t) \propto e^{Ht}$. One can find that the condition (1.6.9) translates in a condition on the duration of the inflation, and assuming this behavior of the scale factor we obtain:

$$N_{inf} \geq (56 - 67), \tag{1.6.11}$$

where we have introduced the *number of e-folds* N_{inf}, defined as:

$$N_{inf} = \int_{t_i}^{t_f} H dt = \log\left(\frac{a(t_f)}{a(t_i)}\right), \tag{1.6.12}$$

where t_f is the time of the end of inflation. The precise requirement on N depends on the details of the inflationary model, but the condition (1.6.11) is typical to solve the horizon and flatness problems. This corresponds to a total expansion during inflation of a factor:

$$\frac{a_f}{a_i} = e^{N_{inf}} \simeq 10^{26} - 10^{30} \tag{1.6.13}$$

Now, let us turn to the second challenge faced by the Hot Big Bang model: the **flatness problem**, and explore how it is resolved within the framework of the inflationary paradigm. As noted in Sec. 1.5, current observations of the density parameters are consistent with a flat universe. Recalling the definitions of the critical density (1.5.1) and the density parameter (1.5.2), the first Friedmann equation can be expressed as:

$$\Omega(t) - 1 = \frac{k}{a^2 H^2} = k\, r_H^2(t), \tag{1.6.14}$$

where this equation illustrates the time evolution of the density parameter. Specifically, it shows that the evolution of Ω is tied to the behavior of the Hubble horizon. Importantly, this equation reveals that if the universe is perfectly flat, then $\Omega = 1$ exactly. However, for any deviation where $\Omega \neq 1$, the difference between Ω and 1 increases proportionally to the growth of $r_H(t)$. As previously discussed, during a matter- or radiation-dominated era, $r_H(t)$ grows over time. Consequently, when we trace backward in time, $\Omega(t)$ becomes progressively closer to 1. Observationally, the current value of Ω is measured as [8]:

$$|\Omega_0 - 1| = 0.0007 \pm 0.0019 \ (68\%). \tag{1.6.15}$$

From Eq. (1.6.14), it follows that the value of Ω at the beginning of the universe was even closer to 1 than it is today. Taking the Planck time $t_{Pl} \sim 10^{-44}$ s after the Big Bang as a reference point—below which our current understanding of physical laws becomes incomplete—a straightforward calculation yields:

$$|\Omega(t_{Pl}) - 1| \simeq |\Omega_0 - 1| \cdot 10^{-60}. \tag{1.6.16}$$

This implies that at the beginning, the spatial curvature must have been extraordinarily close to flatness. This poses a significant problem, as the likelihood of the universe being exactly spatially flat by chance is infinitesimally small (one configuration out of an infinite number of possibilities). So, the flatness problem is related to a **fine-tuning problem**, and highlights the need for an explanation, which the inflationary model provides. By allowing r_H to decrease, the value of $|\Omega - 1|$ also decreases exponentially:

$$|\Omega(t) - 1| \propto r_H^2(t) = \frac{1}{a^2 H^2} \propto e^{-2Ht}. \tag{1.6.17}$$

This approach is particularly compelling because, regardless of the initial deviation, inflation exponentially suppresses the difference from 1. In this context, inflation is often referred to as an *attractor mechanism*. The flatness problem can be resolved if we require:

$$\frac{\Omega_i^{-1} - 1}{\Omega_0^{-1} - 1} \geq 1, \tag{1.6.18}$$

which implies that the density parameter at the onset of inflation was further from 1 compared to its value today. Using the definition in Eq. (1.6.12), and after some calculations, we find that the minimum number of e-foldings

required to solve the flatness problem is approximately $N_{\text{inf}} \simeq 60 - 70$, which coincides with the requirement for solving the horizon problem. Thus, solving the horizon problem is equivalent to solving the flatness problem. This result is not surprising, given the dependence of the density parameter on the Hubble horizon. Inflation provides a dynamical solution to these two issues, describing a mechanism that drives the universe toward a FLRW solution. This means that, regardless of the initial conditions—whether spatial curvature, inhomogeneities, or anisotropies—the inflationary model acts as an attractor that guides the universe toward the smooth, homogeneous, and isotropic state we observe today.

The third most prominent problem of the Hot Big Bang model, briefly described here, is the **unwanted relic problem**, which refers to the theoretical overproduction of stable or long-lived massive particles, such as magnetic monopoles, gravitinos, or other heavy exotic particles, during the early universe. These particles are predicted by various extensions of the Standard Model of particle physics, including Grand Unified Theories (GUTs) and supersymmetry (SUSY). At extremely high temperatures, such as those present during the GUT phase transitions, the production of these relics is energetically favored. However, if these relics are not efficiently diluted or annihilated, their predicted abundance would exceed observational constraints, leading to significant deviations from the observed dynamics and composition of the universe. This problem, particularly the overabundance of magnetic monopoles, serves as another motivation for the introduction of inflation. Inflation dilutes the density of such relics by exponentially expanding the universe, reducing their abundance to negligible levels and resolving the issue within the framework of cosmological theory.

1.7 Inflation

In the previous section, we saw that for inflation to take place we need a phase of accelerated expansion ($\ddot{a} > 0$), where the Hubble radius (r_H) shrinks, and that this correspond to require $w \leq -\frac{1}{3}$. In a de Sitter model we consider $w = -1$ and we have seen that this brings to $a \propto e^{Ht}$, with H constant and given by $H = \sqrt{\frac{\Lambda}{3}}$. In this case we would have an infinite phase of accelerated expansion, that, of course is not possible, so inflation cannot be exactly de Sitter because it has to end. In the current interpretation, Λ is linked to the quantum fluctuations of the vacuum. The vacuum expectation value of the stress-energy tensor gives the energy generated by these fluctuations. Using the Einstein field equations and the definition of Λ, we can write:

$$\langle 0|T_{\mu\nu}|0\rangle = -\langle 0|\rho_\Lambda|0\rangle\, g_{\mu\nu} = -\frac{\Lambda}{8\pi G} g_{\mu\nu} \implies \Lambda = 8\pi G\, \langle 0|\rho_\Lambda|0\rangle \tag{1.7.1}$$

As a result, the vacuum expectation value of the stress-energy tensor acts as the cosmological constant that promotes the expansion. This provides an indication of what to anticipate from a theory describing the inflationary mechanism.

Scalar (Inflaton) Field

To satisfy $P < -\frac{\rho}{3}$, let us introduce a minimally coupled scalar field ϕ with a suitable potential $V(\phi)$, that in general is an effective potential that takes into account the mass term, the self-interaction term and other terms for the interaction of ϕ with other fields. The Lagrangian for this scalar field is given by:

$$\mathcal{L}_\phi = -\frac{1}{2} g^{\mu\nu} \partial_\mu \phi \partial_\nu \phi - V(\phi), \tag{1.7.2}$$

rememebring that for a scalar field the covariant derivative $\nabla_\mu = \partial_\mu$.

The total action can then be expressed as [5]:

$$\begin{aligned} S &= S_{\text{EH}} + S_\phi + S_{\text{matter}} \\ &= \frac{M_{Pl}^2}{2} \int d^4x \sqrt{-g}\, \mathcal{R} + \int d^4x \sqrt{-g}\, \mathcal{L}_\phi\, [\phi, g_{\mu\nu}] + \sum_{i=\text{fields}} \int d^4x \sqrt{-g}\, \mathcal{L}_i, \end{aligned} \tag{1.7.3}$$

where S_{EH} is the Einstein-Hilbert action for the metric, S_ϕ is the action for the scalar field ϕ, and S_{matter} encompasses all other fields. From general

relativity we know we can build a symmetric stress-energy tensor as:

$$T_{\mu\nu} = -\frac{2}{\sqrt{-g}}\frac{\delta S}{\delta g^{\mu\nu}}. \tag{1.7.4}$$

In the case of a minimally coupled scalar, this brings to:

$$T_{\mu\nu} = \partial_\mu\phi\,\partial_\nu\phi + g_{\mu\nu}\left[-\frac{1}{2}g^{\alpha\beta}\partial_\alpha\phi\,\partial_\beta\phi - V(\phi)\right] \tag{1.7.5}$$

Due to the assumptions of homogeneity and isotropy, the metric tensor can be considered invariant under spatial translations and rotations, meaning $g_{\mu\nu} = g_{\mu\nu}(t)$. Similarly, the background value ϕ_0 is assumed to depend only on time. Therefore, we can express both the scalar field and the metric tensor as the sum of a background value and a perturbation term:

$$\phi(\mathbf{x}, t) = \phi_0(t) + \delta\phi(\mathbf{x}, t) \tag{1.7.6}$$

$$g_{\mu\nu}(\mathbf{x}, t) = g^{(0)}_{\mu\nu}(t) + \delta g_{\mu\nu}(\mathbf{x}, t). \tag{1.7.7}$$

This approximation holds if the perturbation is significantly smaller than the background value, which can be expressed as:

$$\langle\delta\phi^2\rangle \ll \phi_0^2(t). \tag{1.7.8}$$

This condition is experimentally supported by observations of the CMB, where the temperature fluctuations are remarkably small, on the order of $\frac{\Delta T}{T} \sim 10^{-5}$.

Background dynamics of the inflaton field

Let's start analyzing the background dynamics; it describes the accelerated expansion during inflation. The metric for this background is assumed to be the FLRW metric with zero spatial curvature. As we have seen in Sec. 1.3, the form of the stress-energy tensor in the FLRW metric is:

$$T^\phi_{00} = \rho_\phi, \tag{1.7.9}$$

$$T^\phi_{ij} = p_\phi g_{ij}. \tag{1.7.10}$$

Comparing these with (1.7.5) we find:

$$\rho_\phi = \frac{1}{2}\dot{\phi}_0^2 + V(\phi_0), \tag{1.7.11}$$

$$p_\phi = \frac{1}{2}\dot{\phi}_0^2 - V(\phi_0). \tag{1.7.12}$$

Since inflation requires negative pressure, we have the condition:

$$V > \dot{\phi}_0^2. \tag{1.7.13}$$

If the kinetic term is negligible compared to the potential term:

$$\frac{1}{2}\dot{\phi}_0^2 \ll V, \tag{1.7.14}$$

we can approximate:

$$p_\phi \approx -\rho_\phi. \tag{1.7.15}$$

This leads to a nearly exponential expansion:

$$a(t) \approx e^{Ht}. \tag{1.7.16}$$

The condition $\frac{1}{2}\dot{\phi}_0^2 \ll V$ ensures the scalar field evolves slowly, which is referred to as the **1st slow-roll condition**. Substituting this into the Friedmann equations, we find:

$$H^2 \approx \frac{8\pi G}{3}\rho_\phi \approx \frac{8\pi G}{3}V(\phi_0). \tag{1.7.17}$$

Here, H remains approximately constant, describing a quasi-de Sitter universe. The equation of motion for the scalar field is generally given by the Klein-Gordon equation:

$$\Box\phi = \frac{\partial V}{\partial \phi}, \tag{1.7.18}$$

where the d'Alembert operator $\Box$ in a curved spacetime is [9]:

$$\Box\phi = \frac{1}{\sqrt{-g}}\partial_\mu\left(\sqrt{-g}\, g^{\mu\nu}\partial_\nu\phi\right). \tag{1.7.19}$$

This simplifies to:

$$\ddot{\phi}_0 + 3H\dot{\phi}_0 + \frac{\partial V(\phi_0)}{\partial \phi_0} = 0. \tag{1.7.20}$$

The term $3H\dot{\phi}_0$ is due to the expansion of the universe and acts as a friction term, distinguishing the scalar field dynamics in an expanding universe from those in Minkowski space. The slow-roll approximation also assumes that

the acceleration of the scalar field is negligible compared to the friction term $3H\dot{\phi}_0$, leading to the **2nd slow-roll condition**:

$$\ddot{\phi}_0 \ll 3H\dot{\phi}_0. \tag{1.7.21}$$

This condition ensures that the dynamics of the inflaton field are dominated by the friction term $3H\dot{\phi}$ caused by the expansion of the universe. Specifically, it ensures that the inflaton field evolves gradually, allowing the potential energy $V(\phi)$ to remain the dominant contribution to the total energy density, such that $H^2 \propto V(\phi)$; moreover, oscillations or rapid accelerations of the inflaton field are suppressed, avoiding significant fluctuations in H that would disrupt the near-exponential growth of the scale factor $a(t)$. This slow and steady evolution is essential for maintaining a quasi-de Sitter universe, characterized by a nearly constant Hubble parameter H and sustained accelerated expansion. Under these conditions, the equation of motion for the background scalar field simplifies to:

$$3H\dot{\phi}_0 \approx -\frac{\partial V}{\partial \phi_0}. \tag{1.7.22}$$

So, our set of slow-roll equations is:

$$\begin{cases} H^2 \approx \frac{8\pi G}{3} V(\phi_0), \\ 3H\dot{\phi}_0 \approx -\frac{\partial V}{\partial \phi_0}. \end{cases} \tag{1.7.23}$$

To quantitatively describe inflationary dynamics, we define the first slow-roll parameter:

$$\epsilon \equiv -\frac{\dot{H}}{H^2}. \tag{1.7.24}$$

For inflation to occur ($\ddot{a} > 0$), this parameter must satisfy:

$$\epsilon \ll 1, \tag{1.7.25}$$

as we can easily see, remembering that $H = \frac{\dot{a}}{a}$. In the slow-roll approximation, H changes very slowly over time. This is quantified by the second slow-roll parameter:

$$\eta \equiv -\frac{\ddot{\phi}}{H\dot{\phi}}. \tag{1.7.26}$$

A quasi-de Sitter universe requires $|\eta| \ll 1$. With some straightforward calculation we can relate the conditions on these parameters to conditions on the V potential, in particular requiring that $\epsilon \ll 1$ corresponds to require:

$$V'(\phi) \ll V(\phi), \tag{1.7.27}$$

known as *flatness condition*, that implies that the slope of the potential is very shallow, ensuring that the inflaton field ϕ rolls slowly down the potential V, maintaining a nearly constant value of the potential energy and so of H. The condition on η is related to V'', which reflects the curvature of the potential, and translates into a requirement for the flatness of $V(\phi)$. However, it is also related to the duration of inflation: requiring $\eta \ll 1$ ensures that inflation lasts for long enough. Indeed In the slow-roll scenario, one can finds that the number of e-folds (1.6.12), which determines the duration of inflation, is given by:

$$N \approx \int_{\phi_i}^{\phi_f} \frac{V(\phi)}{M_{\rm Pl}^2 V'(\phi)}\, d\phi, \tag{1.7.28}$$

where ϕ_i and ϕ_f are the values of the inflaton field at the beginning and end of inflation, respectively, and $M_{Pl} = \frac{1}{\sqrt{8\pi G}}$ is the reduced Planck mass. For inflation to last long enough ($N \sim 60 - 70$), the potential $V(\phi)$ must be sufficiently flat, which requires small values of $V'(\phi)$ and $V''(\phi)$. The parameter η measures the curvature of the potential, and when $\eta \ll 1$, the inflaton field evolves slowly, extending the inflationary phase and increasing the number of e-folds. Conversely, if η is large, the inflaton accelerates rapidly, causing inflation to terminate prematurely and reducing N. Thus, the condition $|\eta| \ll 1$ not only reflects the flatness of the potential but also ensures that inflation lasts long enough to produce a sufficient number of e-folds to solve the horizon and flatness problems.

Reheating

After inflation the standard FLRW radiation dominated universe should start, to recover the well estabilished prediction of the BB model. During the accelerated expansion of the universe $T \propto e^{-Ht}$ and so at the end of iflation temperature become too small to allow a good thermalization of particles. We need a period in ehich the universe is reheated and which comes just before the radiation era, this transitional period is known as *reheating*. In the following, only a brief introduction to the topic is provided.

Inflation persists as long as the slow-roll conditions, $\epsilon \ll 1$ and $|\eta| \ll 1$, hold and ends when ϵ or $|\eta|$ approach 1, signaling the breakdown of the flatness of the potential that drives inflation. For a potential like the one depicted in Figure 1.5, at its minimum σ, the potential induces oscillations in the scalar field with a frequency w such that:

$$w^2 \equiv V''(\sigma) \equiv m^2(\sigma) \gg H^2 \tag{1.7.29}$$

During these oscillations, the scalar field decays into light, relativistic particles, leading to a radiation-dominated era (see Fig. 1.3). To account for the decay of the scalar field, the equation of motion is modified:

$$\ddot{\phi} + (3H + \Gamma_\phi)\dot{\phi} + V'(\phi) = 0, \tag{1.7.30}$$

where Γ_ϕ is the inflaton decay rate. The corresponding energy-density equation becomes [10]:

$$\dot{\rho}_\phi + (3H + \Gamma_\phi)\rho_\phi = 0. \tag{1.7.31}$$

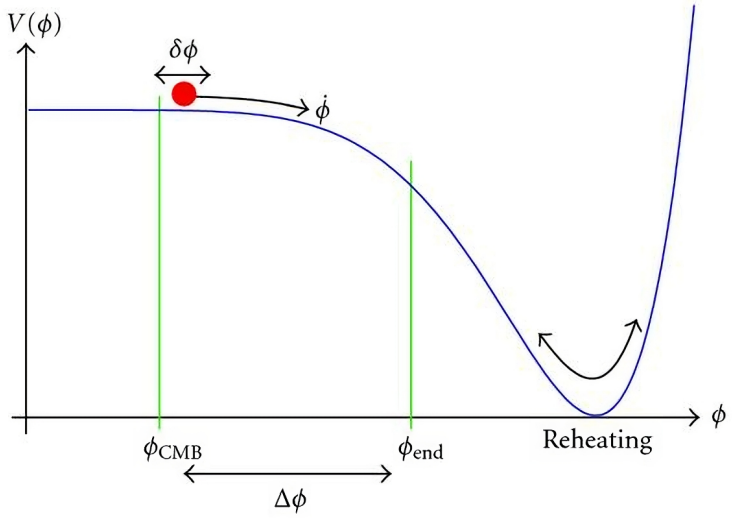

Figure 1.3: A schematic of the inflationary potential $V(\phi)$ showing the inflaton's slow roll, the generation of CMB fluctuations (ϕ_{CMB}), the end of inflation (ϕ_{end}), and the reheating phase where the inflaton oscillates around the potential minimum, transferring energy to radiation.

The efficiency and dynamics of reheating depend on the specifics of the inflationary potential and the coupling between the inflaton and other particles. Thus, understanding reheating is crucial for connecting the successes of inflation with the observable universe we see today.

Quantum fluctuations of the inflaton field

After discussing the dynamics of the background scalar field, we now turn our attention to its perturbations. For a complete treatment of the scalar field $\phi(\mathbf{x}, t)$, which depends on both space and time, the full equation of motion becomes:

$$\ddot{\phi}(\mathbf{x}, t) + 3H\dot{\phi}(\mathbf{x}, t) - \frac{\nabla^2\phi(\mathbf{x}, t)}{a^2} = -\frac{\partial V}{\partial \phi}, \tag{1.7.32}$$

where $\nabla^2 = \partial_i\partial^i$ is the spatial Laplacian wrt the comoving coordinate. Remembering the perturbative splitting $\phi(\mathbf{x}, t) = \phi_0(t) + \delta\phi(\mathbf{x}, t)$, and substituting the background equation into the above expression, the perturbation dynamics are governed by:

$$\delta\ddot{\phi} + 3H\delta\dot{\phi} - \frac{\nabla^2\delta\phi}{a^2} = -\frac{\partial^2 V}{\partial\phi^2}\delta\phi. \tag{1.7.33}$$

If we take the time derivative of the background equation of motion, considering H constant, we obtain:

$$\ddot{\phi}_0 + 3H\dot{\phi}_0 = -V''\phi_0. \tag{1.7.34}$$

Comparing the two equations for $\delta\phi$ and ϕ_0, we notice that they are similar, differing only by the spatial Laplacian term in $\delta\phi$. This means that on large scales, where the spatial Laplacian becomes negligible, these equations reduce to analogous forms, demonstrating the coupling between background and perturbation dynamics. To better analyze these perturbations, we perform a Fourier transformation to transition from coordinate space to momentum space. The equation for the perturbation becomes:

$$\delta\ddot{\phi}_k + 3H\delta\dot{\phi}_k + \frac{k^2}{a^2}\delta\phi_k = -V''\delta\phi_k, \tag{1.7.35}$$

where k is the comoving wave number. The behavior of $\delta\phi_k$ varies significantly depending on whether the scale of interest is smaller or larger than the Hubble horizon.

Small-Scale Regime ($\lambda_{\text{phys}} \ll H^{-1}$): In this regime, where the wavelength is much smaller than the Hubble horizon, the friction term ($3H\delta\dot{\phi}_k$) is negligible, and the equation reduces to:

$$\delta\ddot{\phi}_k + \frac{k^2}{a^2}\delta\phi_k = 0. \tag{1.7.36}$$

This is analogous to a harmonic oscillator with a time-dependent frequency, where the field exhibits oscillatory behavior around its vacuum expectation value, and with an amplitude that decreases with time as:

$$|\delta\phi_k| = \frac{1}{a\sqrt{2k}} \tag{1.7.37}$$

Large-Scale Regime ($\lambda_{\text{phys}} \gg H^{-1}$): When the wavelength exceeds the Hubble horizon, the spatial gradient term (k^2/a^2) becomes negligible, and the equation simplifies to:

$$\delta\ddot{\phi}_k + 3H\delta\dot{\phi}_k = 0. \tag{1.7.38}$$

The solution to this equation shows that the perturbation becomes constant over time:

$$\delta\phi_k = A + Be^{-3Ht}, \tag{1.7.39}$$

where A and B are constants determined by initial conditions. The exponential term quickly decays, leaving the perturbation "frozen" at its value when it crossed the Hubble horizon.

Quantum fluctuations of the scalar field during inflation act as the seeds for cosmological structures. When these fluctuations stretch beyond the Hubble horizon, they effectively freeze, and their amplitudes become imprinted as ini- tial conditions for later cosmic evolution. These frozen perturbations are directly linked to the density variations observed in the Cosmic Microwave Background (CMB). A complete treatment of this process involves the analysis of perturba- tions within the framework of general relativity, which is beyond the scope of this work. For a detailed discussion, see [9]. The relation between these fluctuations can be schematically represented as:

$$\delta\phi \to \zeta \to \frac{\delta\rho}{\rho} \to \frac{\delta T}{T} \tag{1.7.40}$$

where:

- $\delta\phi$ represents quantum fluctuations of the inflaton field,
- ζ is the curvature perturbation,
- $\delta\rho/\rho$ corresponds to density fluctuations,
- $\delta T/T$ represents temperature fluctuations in the CMB.

Chapter 2

Gravitational Instability and Cosmic Structure Formation

The large-scale structures observed in the universe, such as galaxies, clusters, superclusters, and cosmic filaments, are believed to arise from the gravitational amplification of small primordial density fluctuations. This process, known as gravitational instability, operates under the assumption that the dominant matter component in the universe is collisionless cold dark matter (CDM). These CDM particles, while yet to be directly identified, are hypothesized to be non-relativistic and extremely light compared to typical galactic mass scales, with number densities estimated to exceed 10^{50} particles per Mpc^3. In this framework, the vast number of particles ensures that discreteness effects, such as two-body relaxation, are negligible, enabling the treatment of dark matter as a collisionless fluid. This behavior is described by the Vlasov equation, which governs the evolution of the distribution function in phase space. The Vlasov equation, coupled with the Poisson equation for the gravitational potential, forms the foundation of gravitational instability theory and allows for a detailed understanding of the growth of cosmic structures. At scales much smaller than the Hubble radius, the dynamics of CDM particles can be effectively described by Newtonian gravity. In this regime, the equations of motion for CDM particles are adapted to account for the expanding universe through a redefinition of variables for position, momentum, and gravitational potential. This chapter explores the theoretical framework of gravitational instability, starting with the fundamental equations that govern CDM dynamics. We will discuss the role of perturbation theory (PT) in tracing the evolution of density fluctuations from linear

to non-linear regimes, providing a basis for testing the cold dark matter paradigm against cosmological observations.

2.1 The Vlasov Equation

In the following, we primarily follow the discussion presented in [11]. Consider a collection of particles, each of mass m, that interact solely via gravity in an expanding universe. For a particle located at $\mathbf{r}$ with velocity $\mathbf{v}$, its equation of motion is given by the sum of gravitational attractions from all other particles at positions $\mathbf{r}_i$:

$$\frac{d\mathbf{v}}{dt} = G\,m \sum_i \frac{\mathbf{r}_i - \mathbf{r}}{|\mathbf{r}_i - \mathbf{r}|^3}. \tag{2.1.1}$$

In the regime of a very large number of particles, this discrete sum may be replaced by a continuous distribution and expressed in terms of a smooth gravitational potential ϕ:

$$\frac{d\mathbf{v}}{dt} = -\nabla\phi, \tag{2.1.2}$$

where ϕ arises from the local mass density $\rho(\mathbf{r})$:

$$\phi(\mathbf{r}) = G \int d^3\mathbf{r}'\, \frac{\rho(\mathbf{r}')}{|\mathbf{r}' - \mathbf{r}|}. \tag{2.1.3}$$

To incorporate cosmic expansion, we use the conformal time τ, related to the usual cosmic time by $dt = a(\tau)\,d\tau$. The scale factor $a(\tau)$ obeys the Friedmann equations for a homogeneous and isotropic background, that can be written as:

$$\frac{\partial\mathcal{H}(\tau)}{\partial\tau} = -\frac{\Omega_m(\tau)}{2}\,\mathcal{H}^2(\tau) + \frac{\Lambda}{3}\,a^2(\tau) \;\equiv\; \left[\Omega_\Lambda(\tau) \;-\; \frac{\Omega_m(\tau)}{2}\right]\mathcal{H}^2(\tau), \tag{2.1.4}$$

$$\left[\Omega_{\rm tot}(\tau) - 1\right]\mathcal{H}^2(\tau) = k. \tag{2.1.5}$$

Here, $\mathcal{H}(\tau) \equiv \frac{1}{a}\frac{da}{d\tau}$ is the conformal Hubble parameter, and $\Omega_m(\tau)$, $\Omega_\Lambda(\tau)$, $\Omega_{\rm tot}(\tau)$ are the usual density parameters.

When studying gravitational instabilities, we introduce the density contrast $\delta(\mathbf{x}, \tau)$,

$$\rho(\mathbf{x},\tau) = \rho_0(\tau)\big[1+\delta(\mathbf{x},\tau)\big], \tag{2.1.6}$$

where $\rho_0(\tau)$ is the homogeneous background density. The total velocity is split into the Hubble flow plus a peculiar velocity:

$$\mathbf{v}(\mathbf{x},\tau) = \mathcal{H}\,\mathbf{x} + \mathbf{u}(\mathbf{x},\tau). \tag{2.1.7}$$

The cosmological gravitational potential is defined by separating out the unperturbed part,

$$\phi(\mathbf{x},\tau) \equiv -\frac{1}{2}\,\frac{\partial\mathcal{H}}{\partial\tau}\,x^2 + \Phi(\mathbf{x},\tau), \tag{2.1.8}$$

so that Φ depends only on the fluctuations in the matter distribution. Since $\nabla_r^2 = \nabla_x^2/a^2$, the linear Poisson equation in comoving coordinates becomes

$$\nabla^2\Phi(\mathbf{x},\tau) = 4\pi G\,\rho_0\,a^2\,\delta(\mathbf{x},\tau) = \tfrac{3}{2}\,\Omega_m(\tau)\,\mathcal{H}^2(\tau)\,\delta(\mathbf{x},\tau). \tag{2.1.9}$$

Henceforth, all spatial derivatives refer to the comoving coordinate $\mathbf{x}$. The particle equation of motion in conformal time then reads

$$\frac{d\mathbf{p}}{d\tau} = -\,a\,m\,\nabla\Phi(\mathbf{x},\tau), \tag{2.1.10}$$

where $\mathbf{p} \equiv a\,m\,\mathbf{u}$ is the canonical momentum in comoving coordinates.

Now, let's consider the distribution function in phase space, $f(\mathbf{x},\mathbf{p},\tau)$. Since we are considering only gravitational interactions, the system is in the collisionless limit, meaning that particles follow deterministic trajectories in phase space. As a result, the conservation of phase-space density is expressed by the Vlasov equation:

$$\begin{aligned}\frac{df}{d\tau} &\equiv \frac{\partial f}{\partial\tau} + \frac{\partial\mathbf{x}}{\partial\tau}\frac{\partial f}{\partial\mathbf{x}} + \frac{\partial\mathbf{p}}{\partial\tau}\frac{\partial f}{\partial\mathbf{p}} \\ &= \frac{\partial f}{\partial\tau} + \frac{\mathbf{p}}{m\,a}\cdot\nabla f - a\,m\,\nabla\Phi(\mathbf{x},\tau)\cdot\frac{\partial f}{\partial\mathbf{p}} \\ &= 0.\end{aligned} \tag{2.1.11}$$

The nonlinearity arises because Φ itself depends on $\rho(\mathbf{x},\tau)$, which is obtained by integrating f over all momenta (see also Eq. (2.2.1)); in other words, the potential depends on the momentum-averaged distribution of the particles, thus feeding back into the Vlasov equation.

2.2 Eulerian dynamics

In practice, we are usually interested in solving the evolution of the spatial distribution rather than the full phase-space dynamics. This is obtained by taking momentum moments of the distribution function. The zeroth order moment simply relates the phase space density to the local mass density field,

$$\int d^3p\, f(\mathbf{x}, \mathbf{p}, \tau) \equiv \rho(\mathbf{x}, \tau) \tag{2.2.1}$$

The first order moment,

$$\int d^3p\, \frac{\mathbf{p}}{am} f(\mathbf{x}, \mathbf{p}, \tau) \equiv \rho(\mathbf{x}, \tau)\mathbf{u}(\mathbf{x}, \tau), \tag{2.2.2}$$

define the peculiar velocity flow $\mathbf{u}$ as average velocity at $\mathbf{x}$. The second moment,

$$\int d^3p\, \frac{p_i p_j}{a^2 m^2} f(\mathbf{x}, \mathbf{p}, \tau) \equiv \rho(\mathbf{x}, \tau) u_i(\mathbf{x}, \tau) u_j(\mathbf{x}, \tau) + \sigma_{ij}(\mathbf{x}, \tau), \tag{2.2.3}$$

define the stress tensor $\sigma_{ij}(\mathbf{x}, \tau)$ that describes deviations of individual particle velocity from bulk velocity $\mathbf{u}$ and contributes to the anisotropic stress or pressure of the system, while the first term is the contribution of the coherent flow (bulk motion) where all particles at $\mathbf{x}$ are moving together with mean velocity $\mathbf{u}$. In particular, in gravitational collapse or structure formation the velocity dispersion is not uniform and both the bulk flow and the anisotropic random motion are relevant. The equation for these fields follow from taking moments of the Vlasov equation. From the zeroth moment,

$$\int d^3p \left(\frac{\partial f}{\partial \tau} + \frac{\mathbf{p}}{ma} \cdot \nabla f - am \nabla \Phi \cdot \frac{\partial f}{\partial \mathbf{p}} \right) \tag{2.2.4}$$

we obtain the conservation of mass, the continuity equation,

$$\frac{\partial \rho}{\partial \tau} + \nabla \cdot (\rho \mathbf{u}) = 0 \tag{2.2.5}$$

and substuituing ρ in terms of δ :

$$\frac{\partial \delta}{\partial \tau} + \nabla \cdot [(1 + \delta)\mathbf{u}] = 0 \tag{2.2.6}$$

Taking the first moment of the Vlasov equation and using the continuity equation, we obtain the Euler equation,

$$\frac{\partial \mathbf{u}(\mathbf{x},\tau)}{\partial \tau} + \mathcal{H}(\tau)\,\mathbf{u}(\mathbf{x},\tau) + \mathbf{u}(\mathbf{x},\tau)\cdot\nabla\mathbf{u}(\mathbf{x},\tau) = -\nabla\Phi(\mathbf{x},\tau) - \frac{1}{\rho}\nabla_j(\rho\,\sigma_{ij}), \tag{2.2.7}$$

which describes conservation of momentum. The first moment of the distribution function, represented by the peculiar velocity $u(x,\tau)$, is dynamically linked to the stress tensor σ_{ij}, which quantifies deviations of particle motions from a single coherent flow (single stream), for which the first term will be the dominant contribution. In the early stages of structure formation, the approximation $\sigma_{ij} \approx 0$ holds due to negligible pressure in cold dark matter, when structures did not have time to collapse and virialize. This approximation justifies the treatment of the dark matter distribution as a perfect fluid. As cosmic structures evolve and non-linearities grow, this assumption progressively breaks down on smaller scales, necessitating a more detailed treatment of the stress tensor. Notably, Eq. (2.2.7) highlights the key interaction between gravitational potential gradients and the peculiar velocity field, underpinning the dynamics of large-scale structure formation. It sets the stage for exploring deviations from linear theory and the onset of multi-streaming phenomena. We now begin by discussing the solutions of the Poisson equation, the continuity equation, and the Euler equation in the case of a vanishing stress tensor ($\sigma_{ij} = 0$), corresponding to a perfect fluid, and then examine the issues that arise with this description before introducing corrective terms.

2.3 Linear and Non-linear Eulerian Perturbation Theory

At large scales, where we expect the Universe to become smooth, the fluctuation fields $\delta(\mathbf{x},\tau)$, $\mathbf{u}(\mathbf{x},\tau)$ and $\Phi(\mathbf{x},\tau)$ can be assumed to be small compared to the homogeneous contribution. Therefore, it follows that we can linearize Eqs. (2.2.6) - (2.2.7) to obtain the equations of motion in the linear regime:

$$\frac{\partial \delta(\mathbf{x},\tau)}{\partial \tau} + \nabla\cdot\mathbf{u}(\mathbf{x},\tau) = 0 \tag{2.3.1}$$

$$\frac{\partial \mathbf{u}(\mathbf{x},\tau)}{\partial \tau} + \mathcal{H}(\tau)\,\mathbf{u}(\mathbf{x},\tau) = -\nabla\Phi(\mathbf{x},\tau) \tag{2.3.2}$$

The velocity field, as any vector field, can be completely described by its divergence $\boldsymbol{\theta}(\mathbf{x},\tau) \equiv \nabla \cdot \mathbf{u}(\mathbf{x},\tau)$ and its vorticity $\mathbf{w}(\mathbf{x},\tau) \equiv \nabla \times \mathbf{u}(\mathbf{x},\tau)$, whose equations of motion follow from Eq. (2.3.2):

$$\frac{\partial \boldsymbol{\theta}(\mathbf{x},\tau)}{\partial \tau} + \mathcal{H}(\tau)\boldsymbol{\theta}(\mathbf{x},\tau) + \frac{3}{2}\Omega_m \mathcal{H}^2(\tau)\delta(\mathbf{x},\tau) = 0 \tag{2.3.3}$$

$$\frac{\partial \mathbf{w}(\mathbf{x},\tau)}{\partial \tau} + \mathcal{H}(\tau)\mathbf{w}(\mathbf{x},\tau) = 0 \tag{2.3.4}$$

where in the first one we also used the Poisson equation for Φ. The vorticity evolution readily follows from Eq. (2.3.4), $\mathbf{w}(\mathbf{x},\tau) \propto a^{-}1$, i.e. in the linear regime any initial vorticity decays away due to the expansion of the Universe. The continuity equation can be instead rewritten as:

$$\frac{\partial \delta(\mathbf{x},\tau)}{\partial \tau} + \boldsymbol{\theta}(\mathbf{x},\tau) = 0 \tag{2.3.5}$$

Taking the time derivative of (2.3.3) and replacing it in (2.3.5) we get:

$$\frac{\partial^2 \delta(\mathbf{x},\tau)}{\partial \tau^2} + \mathcal{H}(\tau)\frac{\partial \delta(\mathbf{x},\tau)}{\partial \tau} = \frac{3}{2}\Omega_m \mathcal{H}^2(\tau)\delta(\mathbf{x},\tau) \tag{2.3.6}$$

Defining the linear growth factor $D_1(\tau)$ as $\delta(\mathbf{x},\tau) = D_1(\tau)\,\delta(\mathbf{x},0)$, we rewrite the equation as:

$$\frac{d^2 D_1(\tau)}{d\tau^2} + \mathcal{H}(\tau)\frac{dD_1(\tau)}{d\tau} = \frac{3}{2}\Omega_m \mathcal{H}^2(\tau)D_1(\tau) \tag{2.3.7}$$

This equation, together with the Friedmann equations (2.1.4) - (2.1.5), determines the growth of density perturbations in the linear regime as a function of cosmology. Since it is a second-order differential equation, it has two independent solutions, let's denote the fastest growing mode $D_1^{(+)}(\tau)$ and the slowest one $D_1^{(-)}(\tau)$. The evolution of the density contrast is then

$$\delta(\mathbf{x},\tau) = D_1^{(+)}(\tau)A(\mathbf{x}) + D_1^{(-)}(\tau)B(\mathbf{x}) \tag{2.3.8}$$

where $A(\mathbf{x})$ and $B(\mathbf{x})$ are two arbitrary functions of position describing the initial density field configuration, whereas the velocity divergence can be obtained using Eq. (2.3.5).

We will now extend our analysis of the density contrast and velocity fields to account for their non-linear evolution. To proceed, we adopt a

self-consistent approximation by describing the velocity field through its divergence, while justifying the neglect of vorticity. This simplification arises from the assumption that the initial vorticity is negligible, which we will examine further. Starting from the curl of Eq. (3.12) and incorporating the stress tensor σ_{ij} into the momentum conservation equation, the evolution of vorticity $\mathbf{w}(\mathbf{x},\tau) \equiv \nabla \times \mathbf{u}(\mathbf{x},\tau)$ can be written as:

$$\frac{\partial \mathbf{w}(\mathbf{x},\tau)}{\partial \tau} + \mathcal{H}(\tau)\mathbf{w}(\mathbf{x},\tau) - \nabla \times [\mathbf{u}(\mathbf{x},\tau) \times \mathbf{w}(\mathbf{x},\tau)] = \nabla \times \left(\frac{1}{\rho}\nabla \cdot \sigma_{ij}\right). \quad (2.3.9)$$

Let us consider two cases for the initial vorticity. In the first case, if the primordial vorticity is zero and $\sigma_{ij} \approx 0$ (valid for a pressureless perfect fluid), then the vorticity remains zero throughout the evolution. In the second case, if the initial vorticity is non-zero, it decays in the linear regime due to the expansion of the Universe, as discussed earlier. However, non-linear interactions, such as those represented by the third term in the equation above, can amplify vorticity. For simplicity, we assume vanishing primordial vorticity and neglect σ_{ij}, ensuring that vorticity remains zero during evolution. This framework forms the basis of perturbation theory (PT), where density contrast and velocity fields are expanded as perturbative series around their linear solutions. Assuming the variance of linear fluctuations is small and the velocity field is irrotational, we write:

$$\delta(\mathbf{x},\tau) = \sum_{n=1}^{\infty} \delta^{(n)}(\mathbf{x},\tau), \quad (2.3.10)$$

$$\theta(\mathbf{x},\tau) = \sum_{n=1}^{\infty} \theta^{(n)}(\mathbf{x},\tau). \quad (2.3.11)$$

Here, $\delta^{(1)}$ and $\theta^{(1)}$ represent linear terms proportional to the initial density contrast field, while higher-order terms such as $\delta^{(2)}$ and $\theta^{(2)}$ capture quadratic contributions arising from mode coupling. These expansions allow us to systematically analyze the transition from linear to non-linear scales in cosmological structure formation. When we are at large scales, fluctuations are small, therefore linear PT provides an adequate description of cosmological fields. In this regime, different Fourier modes evolve independently conserv-

ing the primordial statistics. So, it is natural to work in Fourier space,[1] where the continuity and Euler equations become:

$$\frac{\partial\delta(\mathbf{k},\tau)}{\partial\tau}+\theta(\mathbf{k},\tau)=-\int\frac{d^3\mathbf{k_1}}{(2\pi)^3}\int\frac{d^3\mathbf{k_2}}{(2\pi)^3}\,\delta_D(\mathbf{k}-\mathbf{k}_1-\mathbf{k}_2)\,\alpha(\mathbf{k}_1,\mathbf{k}_2)\,\delta(\mathbf{k}_1,\tau)\,\theta(\mathbf{k}_2,\tau), \tag{2.3.12}$$

$$\begin{aligned}\frac{\partial\theta(\mathbf{k},\tau)}{\partial\tau}+\mathcal{H}(\tau)\theta(\mathbf{k},\tau)+\frac{3}{2}\Omega_m(\tau)\mathcal{H}^2(\tau)\delta(\mathbf{k},\tau)=\\ =-\int\frac{d^3\mathbf{k_1}}{(2\pi)^3}\int\frac{d^3\mathbf{k_2}}{(2\pi)^3}\,\delta_D(\mathbf{k}-\mathbf{k}_1-\mathbf{k}_2)\,\beta(\mathbf{k}_1,\mathbf{k}_2)\,\theta(\mathbf{k}_1,\tau)\,\theta(\mathbf{k}_2,\tau).\end{aligned} \tag{2.3.13}$$

We have introduced the fundamental mode coupling functions

$$\alpha(\mathbf{k}_1,\mathbf{k}_2)\equiv\frac{(\mathbf{k}_1+\mathbf{k}_2)\cdot\mathbf{k}_1}{k_1^2}\quad\text{and}\quad\beta(\mathbf{k}_1,\mathbf{k}_2)\equiv\frac{(\mathbf{k}_1+\mathbf{k}_2)^2\,(\mathbf{k}_1\cdot\mathbf{k}_2)}{2k_1^2k_2^2}, \tag{2.3.14}$$

that encode the non-linearity of the evolution and come from the non-linear terms in the continuity and Euler equations respectively.

Now, we analyze the case of an Einstein-de Sitter universe, characterized by $\Omega_m=1$ and $\Omega_\Lambda=0$. Using the Friedmann equation, we find that the scale factor evolves as $a(\tau)\sim\tau^2$, and the Hubble parameter becomes $H(\tau)=\frac{2}{\tau}$. This allows us to simplify the equations of motion for perturbations by factoring out $\mathcal{H}$ from the velocity field, rendering Eqs. (2.3.12) and (2.3.13) homogeneous in either τ or equivalently in $a(\tau)$. Under this framework, the continuity and Euler equations in Fourier space can be solved using a

[1] In this work, we use the following convention for the Fourier transform:

$$X(k)=\int d^3x\,e^{-i\mathbf{k}\cdot\mathbf{x}}X(\mathbf{x}),\quad X(\mathbf{x})=\int\frac{d^3k}{(2\pi)^3}e^{i\mathbf{k}\cdot\mathbf{x}}X(\mathbf{k}),$$

leading to the definition of the Dirac delta function δ_D,

$$\int d^3x\,e^{i(\mathbf{k}_1-\mathbf{k}_2)\cdot\mathbf{x}}=(2\pi)^3\delta_D(\mathbf{k}_1-\mathbf{k}_2).$$

perturbative expansion of the following form[2]:

$$\delta(\mathbf{k},\tau) = \sum_{n=1}^{\infty} a^n(\tau)\delta_n(\mathbf{k}), \tag{2.3.15}$$

$$\theta(\mathbf{k},\tau) = -H(\tau)\sum_{n=1}^{\infty} a^n(\tau)\theta_n(\mathbf{k}), \tag{2.3.16}$$

where only the fastest-growing mode of perturbations is considered. At early times ($a \to 0$), these series are dominated by their leading terms. From the continuity equation, it follows that $\theta_1(\mathbf{k}) = \delta^{(1)}(\mathbf{k})$, meaning that the linear perturbations are fully described by $\delta^{(1)}(\mathbf{k})$. To satisfy the original equations of motion (Eqs. (2.3.12) and (2.3.13)), the higher-order perturbations $\delta_n(\mathbf{k})$ and $\theta_n(\mathbf{k})$ are expressed in terms of the linear density contrast field as:

$$\delta^{(n)}(\mathbf{k}) = \left[\prod_{i=1}^{n}\int \frac{\mathrm{d}^3 q_i}{(2\pi)^3}\right] (2\pi)^3\delta_D\left(\mathbf{k}-\mathbf{q}_{1\ldots n}\right) F_n(\mathbf{q}_1,\ldots,\mathbf{q}_n)\left[\prod_{i=1}^{n}\delta^{(1)}(\mathbf{q}_i)\right], \tag{2.3.17}$$

$$\theta^{(n)}(\mathbf{k}) = \left[\prod_{i=1}^{n}\int \frac{\mathrm{d}^3 q_i}{(2\pi)^3}\right] (2\pi)^3\delta_D\left(\mathbf{k}-\mathbf{q}_{1\ldots n}\right) G_n(\mathbf{q}_1,\ldots,\mathbf{q}_n)\left[\prod_{i=1}^{n}\delta^{(1)}(\mathbf{q}_i)\right]. \tag{2.3.18}$$

Here, F_n and G_n are the perturbative kernels capturing the non-linear mode coupling due to gravitational interactions. Demanding that these expressions solve Eqs. (2.3.12) - (2.3.13) at any given order in $\delta^{(1)}$, these equations then transform into recursion relations for the kernels F_n and G_n:

$$F_n(\mathbf{q}_1,\ldots,\mathbf{q}_n) = \sum_{m=1}^{n-1}\frac{G_m(\mathbf{q}_1,\ldots,\mathbf{q}_m)}{(2n+3)(n-1)}\Big[(2n+1)\alpha(\mathbf{k}_1,\mathbf{k}_2)F_{n-m}(\mathbf{q}_{m+1},\ldots,\mathbf{q}_n) + 2\beta(\mathbf{k}_1,\mathbf{k}_2)G_{n-m}(\mathbf{q}_{m+1},\ldots,\mathbf{q}_n)\Big], \tag{2.3.19}$$

$$G_n(\mathbf{q}_1,\ldots,\mathbf{q}_n) = \sum_{m=1}^{n-1}\frac{G_m(\mathbf{q}_1,\ldots,\mathbf{q}_m)}{(2n+3)(n-1)}\Big[3\alpha(\mathbf{k}_1,\mathbf{k}_2)F_{n-m}(\mathbf{q}_{m+1},\ldots,\mathbf{q}_n)$$

[2]Although this result is technically only valid for the EdS universe, it can be approximately extended to arbitrary values of Ω_m and Ω_Λ, by substituting the EdS growth factor a with the growth factor of the corresponding cosmology, $D(a)$ [11].

$$+ 2n\beta(\mathbf{k}_1, \mathbf{k}_2) G_{n-m}(\mathbf{q}_{m+1}, \ldots, \mathbf{q}_n) \Big], \tag{2.3.20}$$

where $\mathbf{k}_1 \equiv \mathbf{q}_1 + ... + \mathbf{q}_m$, $\mathbf{k}_2 \equiv \mathbf{q}_{m+1} + ... + \mathbf{q}_n$ and $\mathbf{k} \equiv \mathbf{k}_1 + \mathbf{k}_2$. In particular, we find $F_1 = G_1 = 1$, recovering the linear growing mode. For $n = 2$, if we symmetrize the expressions with respect to $\mathbf{q}_1$ and $\mathbf{q}_2$, we find:

$$F_2(\mathbf{q}_1, \mathbf{q}_2) = \frac{5}{7} + \frac{1}{2} \frac{\mathbf{q}_1 \cdot \mathbf{q}_2}{q_1 q_2} \left(\frac{q_1}{q_2} + \frac{q_2}{q_1} \right) + \frac{2}{7} \frac{(\mathbf{q}_1 \cdot \mathbf{q}_2)^2}{q_1^2 q_2^2}, \tag{2.3.21}$$

$$G_2(\mathbf{q}_1, \mathbf{q}_2) = \frac{3}{7} + \frac{1}{2} \frac{\mathbf{q}_1 \cdot \mathbf{q}_2}{q_1 q_2} \left(\frac{q_1}{q_2} + \frac{q_2}{q_1} \right) + \frac{4}{7} \frac{(\mathbf{q}_1 \cdot \mathbf{q}_2)^2}{q_1^2 q_2^2}. \tag{2.3.22}$$

Symmetrized kernels are used in perturbation theory to ensure solutions respect the symmetries of the universe, including isotropy, homogeneity, and invariance under wavevector permutations. They enforce permutational symmetry, ensuring the density contrast treats all wavevector configurations equivalently, reflecting the symmetry of the underlying physics. Symmetrization ensures physical consistency by enforcing momentum conservation among interacting wavevectors in Fourier space, ensuring that the solutions remain consistent with the fundamental equations governing the evolution of the density field. Furthermore, it eliminates redundant contributions in higher-order calculations, simplifying both analytical and computational efforts. Finally, symmetrized kernels are essential for computing statistical observables such as the power spectrum and bispectrum, which inherently average over all wavevector permutations.

2.4 Correlators, Power Spectra, and Cosmic Random Fields

The density contrast field, $\delta(\mathbf{x})$, has an ensemble average of zero by definition (indeed, it's the vacuum expectation value), but its statistical properties can be studied through correlations. The two-point correlation function, defined as:

$$\xi(r) = \langle \delta(\mathbf{x}) \delta(\mathbf{x} + \mathbf{r}) \rangle \,, \tag{2.4.1}$$

depends only on the norm of $\mathbf{r}$ due to statistical homogeneity and isotropy. The Fourier transform of $\delta(\mathbf{x})$ is:

$$\delta(\mathbf{x}) = \int \frac{d^3k}{(2\pi)^3}\, \delta(\mathbf{k})\, e^{i\mathbf{k}\cdot\mathbf{x}}, \tag{2.4.2}$$

where $\delta(\mathbf{k})$ are complex random variables satisfying $\delta(\mathbf{k}) = \delta^*(-\mathbf{k})$ due to the reality of $\delta(\mathbf{x})$. The power spectrum $P(k)$ is defined via the Fourier-space correlator:

$$\begin{aligned}\langle \delta(\mathbf{k})\delta(\mathbf{k}')\rangle &= \int d^3\mathbf{x}\, d^3\mathbf{r}\, \langle \delta(\mathbf{x})\delta(\mathbf{x}+\mathbf{r})\rangle \exp\left[-i(\mathbf{k}+\mathbf{k}')\cdot\mathbf{x} - i\mathbf{k}'\cdot\mathbf{r}\right] \\ &= (2\pi)^3\, \delta_D(\mathbf{k}+\mathbf{k}') \int d^3\mathbf{r}\, \xi(r)\, \exp(i\mathbf{k}\cdot\mathbf{r}) \\ &\equiv (2\pi)^3 \delta_D(\mathbf{k}+\mathbf{k}') P(k).\end{aligned} \tag{2.4.3}$$

So, the relation between the correlation function and the power spectrum is:

$$\xi(r) = \int \frac{d^3k}{(2\pi)^3} P(k) e^{i\mathbf{k}\cdot\mathbf{r}}. \tag{2.4.4}$$

The variance of $\delta(\mathbf{x})$ is:

$$\begin{aligned}\langle \delta^2(\mathbf{x})\rangle = \xi(0) &= \int \frac{d^3k}{(2\pi)^3} P(k) = \frac{1}{2\pi^2}\int_0^\infty dk\, k^2 P(k) \\ &= \frac{1}{2\pi^2}\int_0^\infty \frac{dk}{k}\, k^3 P(k) = \int_0^\infty \frac{dk}{k}\Delta(k)\end{aligned} \tag{2.4.5}$$

where $\Delta(k) = \frac{k^3}{2\pi^2}P(k)$ is the dimensionless power spectrum. Different conventions for Fourier transforms affect the definition of $P(k)$, but we adopt the convention in Eq. (2.4.2).

The Wick Theorem for Gaussian Fields

The power spectrum $P(k)$ is a fundamental quantity for characterizing almost all homogeneous random fields. Its utility becomes evident for Gaussian random fields, where the joint distribution of density values is Gaussian. For such fields, the Wick theorem applies: the ensemble average of any product of variables can be expressed in terms of two-point correlators. This is a

foundational concept in classical and quantum field theories. Explicitly, for the Fourier modes, the Wick theorem states:

$$\langle \delta(\mathbf{k}_1) \cdots \delta(\mathbf{k}_{2p+1}) \rangle = 0, \tag{2.4.6}$$

$$\langle \delta(\mathbf{k}_1) \cdots \delta(\mathbf{k}_{2p}) \rangle = \sum_{\text{all pairings}} \prod_{\text{pairs } (i,j)} \langle \delta(\mathbf{k}_i) \delta(\mathbf{k}_j) \rangle. \tag{2.4.7}$$

Thus, the statistical properties of the random variables $\delta(\mathbf{k})$ are fully specified by the shape and normalization of $P(k)$. A specific cosmological model, in the linear regime, is determined primarily by the power spectrum and the cosmological parameters Ω_m and Ω_Λ.

Higher-Order Correlators

Higher-order correlation functions are defined as the connected parts (subscript c) of joint ensemble averages of the density contrast. The N-point correlation function is expressed as:

$$\begin{aligned} \xi_N(\mathbf{x}_1, \ldots, \mathbf{x}_N) &= \langle \delta(\mathbf{x}_1) \cdots \delta(\mathbf{x}_N) \rangle_c \\ &\equiv \langle \delta(\mathbf{x}_1) \cdots \delta(\mathbf{x}_N) \rangle \\ &\quad - \sum_{S \in P(\{\mathbf{x}_1, \ldots, \mathbf{x}_N\})} \prod_{s_i \in S} \xi_{\#s_i}(\mathbf{x}_{s_i(1)}, \ldots, \mathbf{x}_{s_i(\#s_i)}), \end{aligned} \tag{2.4.8}$$

where the sum is over all proper partitions of $\{\mathbf{x}_1, \ldots, \mathbf{x}_N\}$, excluding the set itself. If the mean of $\delta(\mathbf{x})$ is zero, only partitions without singlets contribute. For Gaussian fields, all connected correlators beyond the two-point function vanish, making ξ_2 the sole non-zero connected part. Consequently, any field constructed from a Gaussian field δ has its statistics entirely determined by two-point functions. In Fourier space, due to homogeneity, connected N-point correlators are proportional to $\delta_D(\mathbf{k}_1 + \cdots + \mathbf{k}_N)$. This allows us to define the generalized power spectrum:

$$\langle \delta(\mathbf{k}_1) \cdots \delta(\mathbf{k}_N) \rangle_c = (2\pi)^3 \delta_D(\mathbf{k}_1 + \cdots + \mathbf{k}_N) P_N(\mathbf{k}_1, \ldots, \mathbf{k}_N), \tag{2.4.9}$$

where $P_N(\mathbf{k}_1, \ldots, \mathbf{k}_N)$ is the N-point spectrum. For $N = 3$, this corresponds to the bispectrum $B(\mathbf{k}_1, \mathbf{k}_2, \mathbf{k}_3)$, a key tool for probing non-Gaussianity.

Linear Power Spectrum

In linear theory, the two-point correlation of the density contrast in Fourier space is given by:

$$\langle \delta^{(1)}(\mathbf{k})\delta^{(1)}(\mathbf{k}')\rangle = (2\pi)^3\delta_D(\mathbf{k}+\mathbf{k}')P_L(k,\tau), \tag{2.4.10}$$

where $P_L(k,\tau) = D_+^2(\tau)P_L(k)$. As is standard in cosmological perturbation theory, we normalize $D_+(\tau)$ such that $D_+(\tau=\tau_0)=1$, ensuring that $P_L(k)$ represents the linear matter power spectrum at redshift zero.
The linear matter power spectrum in the ΛCDM model exhibits a characteristic shape reflecting various stages of cosmological evolution. Its asymptotic behaviors are:

$$P_L \propto k, \quad \text{as } k\to 0, \quad \text{and} \quad P_L \propto k^{-3}\ln^2(k), \quad \text{as } k\to\infty.$$

It features a peak at the wavenumber corresponding to the comoving size of the Hubble horizon at the time of matter-radiation equality, $k \approx 0.015\,\mathrm{h\ Mpc^{-1}}$. A plot of the linear power spectrum can be found in Fig.2.1.

To estimate the typical density constrast variance at a given point $\mathbf{x}$, we compute:

$$\langle \delta^2(\mathbf{x})\rangle = \int \frac{d^3q}{(2\pi)^3}P_L(q). \tag{2.4.11}$$

Surprisingly, for the ΛCDM power spectrum, this integral diverges in the ultraviolet (UV), meaning that short-scale mass fluctuations formally lead to an infinite variance. This divergence indicates a breakdown of the assumption that δ is small and challenges the validity of linear theory at these scales.
A more physically reasonable approach is to filter out short-scale fluctuations by introducing a low-pass filter W_R with a filtering scale R. By choosing R appropriately, we can ensure that the coarse-grained density fluctuations remain well-defined. This observation suggests that the natural variables in cosmological perturbation theory should be the smoothed density and velocity fields.

One-loop Power Spectrum and Bispectrum

Using the non-linear perturbation theory results and in particular Eqs. (2.3.17) - (2.3.18) we can compute the power spectrum at order $[\delta^{(1)}]^4$. For simplicity,

in the following we adopt the short hand notation $\delta(\mathbf{k}) = \delta_{\mathbf{k}}$:

$$\begin{aligned}\langle \delta_{\mathbf{k}} \delta_{\mathbf{k}'} \rangle &= \langle (\delta^{(1)}_{\mathbf{k}} + \delta^{(2)}_{\mathbf{k}} + \delta^{(3)}_{\mathbf{k}})(\delta^{(1)}_{\mathbf{k}'} + \delta^{(2)}_{\mathbf{k}'} + \delta^{(3)}_{\mathbf{k}'}) \rangle \\ &= \langle \delta^{(1)}_{\mathbf{k}} \delta^{(1)}_{\mathbf{k}'} \rangle + \langle \delta^{(2)}_{\mathbf{k}} \delta^{(2)}_{\mathbf{k}'} \rangle + 2 \langle \delta^{(3)}_{\mathbf{k}} \delta^{(1)}_{\mathbf{k}'} \rangle \\ &\equiv (2\pi)^3 \delta(\mathbf{k} + \mathbf{k}') \left(P_{11} + P_{22} + P_{13} \right),\end{aligned} \tag{2.4.12}$$

where we used the exchange symmetry $\mathbf{k} \leftrightarrow \mathbf{k}'$ of the P_{13} term.
The first term is just the linear power spectrum, $P_{11} \equiv P_L$. The computation of the other terms can be found in Appendix A and bring to these results:

$$\langle \delta^{(2)}(\mathbf{k}_1) \delta^{(2)}(\mathbf{k}_2) \rangle = (2\pi)^3 \delta_D(\mathbf{k}_1 + \mathbf{k}_2)\, 2 \int \frac{d^3q}{(2\pi)^3} \left[F_2(\mathbf{q}, \mathbf{k}_1 - \mathbf{q}) \right]^2 P_L(q) P_L(|\mathbf{k}_1 - \mathbf{q}|), \tag{2.4.13}$$

$$\langle \delta^{(3)}(\mathbf{k}_1) \delta^{(1)}(\mathbf{k}_2) \rangle = (2\pi)^3 \delta_D(\mathbf{k}_1 + \mathbf{k}_2)\, 6 \int \frac{d^3q}{(2\pi)^3} F_3(\mathbf{q}, -\mathbf{q}, \mathbf{k}_1) P_L(q) P_L(k_1). \tag{2.4.14}$$

Collecting them, we obtain:

$$\begin{aligned}P_{\text{1-loop}}(k_1) = (2\pi)^3 \delta_D(\mathbf{k}_1 + \mathbf{k}_2) \Bigg[& P_L(k_1) \\ & + 2 \int \frac{d^3q}{(2\pi)^3} \left[F_2(\mathbf{q}, \mathbf{k}_1 - \mathbf{q}) \right]^2 P_L(q) P_L(|\mathbf{k}_1 - \mathbf{q}|) \\ & + 6 \int \frac{d^3q}{(2\pi)^3} F_3(\mathbf{q}, -\mathbf{q}, \mathbf{k}_1) P_L(q) P_L(k_1) \Bigg].\end{aligned} \tag{2.4.15}$$

In Fig. 2.1, we present a plot of P_{22} and P_{13} in comparison with P_L. The one-loop corrections to the integral increase significantly with increasing wavenumber. Notably, $P_{22}(k)$ is positive, while $P_{13}(k)$ is negative. As a result, the two corrections nearly cancel each other, leading to a relatively small overall correction. However, starting at $k \approx 0.1\,\text{h/Mpc}$, the corrections to the linear power spectrum become non-negligible, indicating that the linear regime is no longer valid.

We now present the bispectrum at order $[\delta^{(1)}]^4$. For a detailed derivation, refer to Appendix A. Figure 2.2 displays plots for various bispectrum configurations.

$$\langle \delta(\mathbf{k}_1) \delta(\mathbf{k}_2) \delta(\mathbf{k}_3) \rangle \equiv (2\pi)^3 \delta^{(3)}_D(\mathbf{k}_1 + \mathbf{k}_2 + \mathbf{k}_3) B(k_1, k_2, k_3), \tag{2.4.16}$$

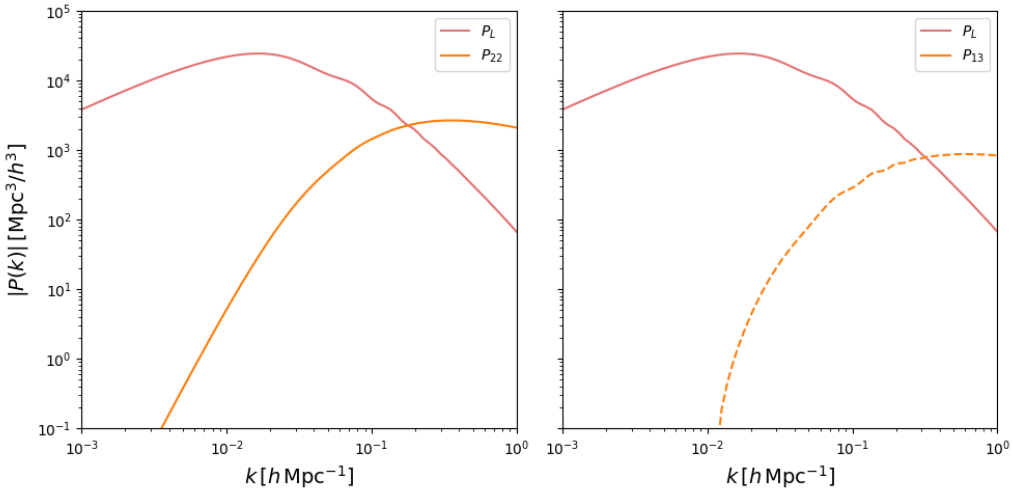

Figure 2.1: Left panel: Plot of the linear power spectrum (P_L, red line) and the P_{22} one-loop contribution (orange line) at $z = 0$. Right panel: Similar to the left panel, but showing the P_{13} one-loop contribution instead. The dashed line indicates a negative contribution. The plot is obtained using the FFTLog method, with P_L derived from the CLASS-PT library. More details can be found in Appendix A.

where

$$B(\mathbf{k}_1, \mathbf{k}_2, \mathbf{k}_3) = 2F_2(\mathbf{k}_1, \mathbf{k}_2)P_L(k_1)P_L(k_2) + 2\,\mathrm{cyc.} \tag{2.4.17}$$

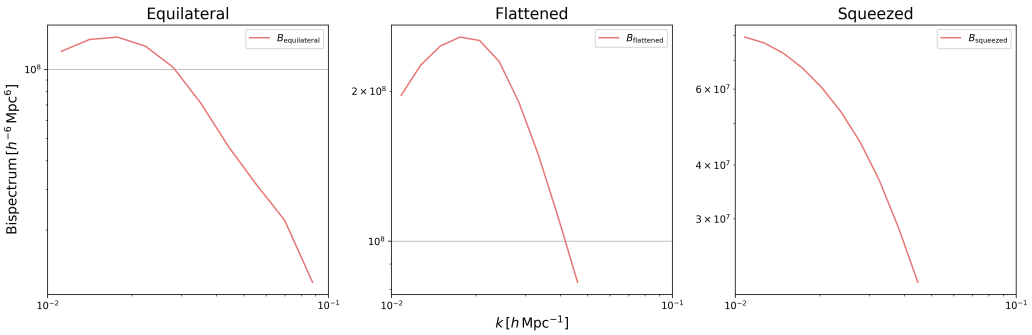

Figure 2.2: Plots of the bispectrum for three configurations: equilateral ($k_1 \approx k_2 \approx k_3$), flattened ($k_1 \approx k_2 \approx k_3/2$), and squeezed ($k_1 \ll k_2 \approx k_3$). The bispectrum is computed up to $k = 0.10\,h\,\text{Mpc}^{-1}$, as beyond this scale, the tree-level bispectrum is no longer a sufficient approximation.

2.5 Limitations of the Pressureless Perfect Fluid Model

As seen when computing the variance of the density contrast, Eq. (2.4.11), we need to work with coarse-grained fields to ensure small fluctuations. Moreover, several issues arise in this simplified PPF model, which we briefly discuss below.

IR and UV Singularities in the PPF Model

In the analysis of the one-loop power spectrum integrals, two major sources of divergence arise: the infrared singularities and ultraviolet singularities. These issues stem from the behavior of the power spectrum at extreme scales, highlighting the limitations of the PPF model.
The IR singularities emerge due to displacements caused by long-wavelength modes. At the one-loop level, the contributions from P_{22} and P_{13} exhibit the following IR limits [12]:

$$P_{22}(k)\Big|_{q\ll k,|\mathbf{q}-\mathbf{k}|\ll k} = \frac{k^2}{3}P_{11}(k)\int_{q\ll k}\frac{d^3q}{q^2}P_{11}(q), \tag{2.5.1}$$

$$P_{13}(k)\Big|_{q\ll k} = -\frac{k^2}{3}P_{11}(k)\int_{q\ll k}\frac{d^3q}{q^2}P_{11}(q). \tag{2.5.2}$$

These contributions individually diverge due to the IR displacements. However, their sum respects the equivalence principle, resulting in an exact cancellation of the IR singularities. This ensures that physical observables like correlation functions remain finite. Despite this cancellation, the IR displacements influence the BAO (Baryon Acoustic Oscillations) features in the power spectrum. BAO refers to the periodic fluctuations in the density of visible baryonic matter (normal matter) in the universe, which were imprinted during the early universe when sound waves propagated through the hot plasma before recombination. These effects include the smoothing of the BAO peak and a slight shift in its position. Such displacements are not adequately captured in the PPF model and require resummation techniques for an accurate treatment. For more details about the BAO, please refer to [13]. This is achieved within the framework of time-sliced perturbation theory, the results of which will be briefly discussed in a subsequent section.

UV singularities originate from the behavior of the one-loop integrals at small scales, where nonlinear physics becomes significant. The UV contributions for P_{22} and P_{13} are [14]:

$$P_{22}(k)\Big|_{q\gg k} = \frac{9}{196\pi^2}k^4\int_{q\gg k}\frac{dq}{q^2}P_L^2(q), \tag{2.5.3}$$

$$P_{13}(k)\Big|_{q\gg k} = -\frac{61}{630\pi^2}k^2P_L(k)\int_{q\gg k}dqP_L(q). \tag{2.5.4}$$

While these integrals converge for the ΛCDM power spectrum, they fail to capture the physics of small-scale virialization, where halos form. In perturbation theory, UV modes contribute unphysically large displacements, ignoring the confinement effects of halos.

Physical IR and UV Effects

The physical IR effects arise from the coherent displacements induced by large-scale flows. These flows move structures coherently over scales comparable to the BAO wavelength, leading to the suppression and shift of the BAO peak. The suppression is encapsulated in the smoothed power spectrum:

$$P(k) = P_{\text{smooth}}(k) + P_{\text{wiggle}}(k), \tag{2.5.5}$$

where P_{wiggle} describes the oscillatory BAO feature, modified by resummation methods to include the effects of long-wavelength modes.

UV effects are tied to unresolved small-scale physics, such as virialized halo formation. To address these, counterterms are introduced, leading to an effective modification of the Euler equation:

$$\frac{\partial}{\partial\tau}v^i + \mathcal{H}v^i + v^j\partial_j v^i = -\partial_i\Phi - c_s^2\partial_i\delta, \tag{2.5.6}$$

where c_s^2 represents the effective sound speed. This results in a UV-regulated correction to the one-loop power spectrum:

$$P_{\text{1-loop}}(k) = P_L(k) + P_{22}(k) + P_{13}(k) - 2k^2\gamma P_L(k), \tag{2.5.7}$$

with γ parameterizing the small-scale cutoff effects.

By addressing these IR and UV effects, the theoretical framework ensures consistency with physical principles and observational data, resolving the singularities and incorporating essential physical phenomena. Ultimately, the introduction of a non-zero stress tensor provides a systematic way to address UV singularities and physical effects associated with unresolved small-scale nonlinearities, such as virialization. This will be introduced in the next section.

2.6 Beyond Eulerian Perturbation Theory

In the following, we present the elements upon which the Effective Field Theory (EFT) approach to large-scale structure is based and discuss its main results. To address the issues encountered with the PPF model, we adopt a bottom-up approach by coarse-graining the equations of motion for the density contrast and velocity fields. Additionally, we introduce a stress-energy tensor and a momentum cutoff to systematically account for non-linear effects, including shot noise and counterterm corrections. So, the new equations of motion read:

$$\frac{\partial}{\partial\tau}\delta_\ell(\mathbf{x},\tau) + \partial_i\left[(1+\delta_\ell(\mathbf{x},\tau))v_\ell^i(\mathbf{x},\tau)\right] = 0, \tag{2.6.1}$$

$$\begin{aligned}\frac{\partial}{\partial\tau}v_\ell^i(\mathbf{x},\tau) + \mathcal{H}v_\ell^i(\mathbf{x},\tau) + v_\ell^j(\mathbf{x},\tau)\partial_j v_\ell^i(\mathbf{x},\tau) + \partial_i\Phi_\ell(\mathbf{x},\tau)& \\ = -\frac{1}{\rho_\ell(\mathbf{x},\tau)}\left[\partial_j\sigma_\ell^{ij}(\mathbf{x},\tau)\right]_\Lambda,&\end{aligned} \tag{2.6.2}$$

$$\Delta\Phi_\ell(\mathbf{x},\tau) = \frac{3}{2}\mathcal{H}^2\Omega_m(\tau)\delta_\ell(\mathbf{x},\tau). \tag{2.6.3}$$

Here, our variables are the long-wavelenght density contrast and velocity fields. Even though these coarse grained variables explicitly depend on the smoothing scale, the physical observables do not. Technically, this is realized by means of counterterms embedded in the stress tensor. The quantity that appears in the r.h.s. of the Euler equation is the smoothed divergence of the effective stress tensor, σ^{ij} . This term incorporates the effects of the short scale physics and its backreaction on large scales, such as halo virialization and non-linear interactions. In the following, the new contributions arising from the introduction of the stress tensor are briefly discussed. For a more detailed explanation, see [15]. The stress tensor is expressed in terms of effective operators, with its leading-order contributions written as:

$$\frac{1}{\rho_\ell(\mathbf{x},\tau)}\left[\partial_j\sigma_\ell^{ij}(\mathbf{x},\tau)\right]_\Lambda = c_s^2(\tau)\,\partial^i\delta(\mathbf{x},\tau), \tag{2.6.4}$$

where c_s^2 is the effective sound speed, encapsulating the small-scale physics that modulate the large-scale dynamics, as presented in Eq. (2.5.6).

Stochastic term

Small-scale perturbations, due to non-linear collapse and virialization, are not statistically correlated over long distances. These processes erase memory of initial conditions, making the short-scale density field partially uncorrelated with long-wavelength modes. This introduces a stochastic (noise) component into the effective stress-energy tensor:

$$\frac{1}{\rho_\ell}[\partial_j\sigma_\ell^{ij}(\mathbf{x},\tau)]_\Lambda \supset J^i, \tag{2.6.5}$$

where J^i is the stochastic term and satisfies $\langle J^i\delta_\ell\rangle = 0$, reflecting the statistical independence between the stochastic contributions and the coarse-grained density field δ_ℓ. This stochastic contribution propagates into the density field as:

$$\delta_{\text{stoch}} \propto \partial_i J^i, \tag{2.6.6}$$

where the divergence $\partial_i J^i$ reflects how small-scale stochastic velocity fluctuations redistribute matter density through the continuity equation (where $\mathbf{v}_\ell \to \mathbf{v}_\ell + \mathbf{J}$). Symmetry arguments constrain the scale dependence of δ_{stoch}.

For $k \to 0$, mass conservation requires that stochastic noise does not introduce a net density shift, excluding constant contributions (k^0). Similarly, momentum conservation prevents linear contributions (k^1), as large-scale flows cannot generate net momentum from small-scale noise. These constraints imply that the leading-order contribution scales as:

$$\delta_{\rm stoch} \propto k^2. \tag{2.6.7}$$

This scaling reflects the suppression of stochastic effects at large scales and their quadratic growth with wavenumber, leading to the following power spectrum of the stochastic term:

$$\begin{aligned}\langle \delta_{\rm stoch}(\mathbf{k}')\delta_{\rm stoch}(\mathbf{k})\rangle &= (2\pi)^3\delta_D(\mathbf{k}+\mathbf{k}')P_J(k) \\ &= (2\pi)^3\delta_D(\mathbf{k}+\mathbf{k}')R^7_{\rm stoch}k^4 + \cdots ,\end{aligned} \tag{2.6.8}$$

where $R_{\rm stoch}$ is a parameter with dimensions of length.
In many cases, the stochastic contribution to the galaxy power spectrum is idealized as a Poissonian noise term, which arises from the discreteness of tracers in a finite sample. Under this assumption, the power spectrum of the stochastic component takes the form:

$$P_{\rm stoch}(k) = \frac{1}{\bar{n}}, \tag{2.6.9}$$

where $\bar{n}$ is the mean number density of tracers. This approximation assumes that the stochastic fluctuations are independent and uncorrelated beyond the scale of individual tracers, leading to a scale-independent (white noise) contribution at leading order. However, as described above, additional physical constraints from mass and momentum conservation imply that the lowest-order stochastic corrections scale as k^2 or higher, modifying the simple Poissonian expectation on large scales. In the end, we can write the stochastic term as:

$$P_{\rm stoch}(k) = \frac{1}{\bar{n}}\left(1 + \alpha + \beta k^2\right), \tag{2.6.10}$$

where the two free parameters α and β describe, respectively, constant and scale-dependent corrections to the Poisson shot-noise term $1/\bar{n}$.

The stochastic correction to the real space bispectrum, Eq. (2.4.17), can be written as [16]:

$$B_{\rm stoch}(k_1,k_2,k_3) = P_{\rm shot}\left[P_L(k_1) + P_L(k_2) + P_L(k_3)\right] + B_{\rm shot}. \tag{2.6.11}$$

Full one-loop prediction

Adding these leading order stress tensor terms, it's convenient to express the total density constrast field as:

$$\delta_{\mathbf{k}}^{\mathrm{NL}} = \delta_{\mathbf{k}}^{(1)} + \delta_{\mathbf{k}}^{(2)} + \delta_{\mathbf{k}}^{(3)} + \delta_{\mathbf{k}}^{\mathrm{stress.}} + \delta_{\mathbf{k}}^{\mathrm{stoch.}}, \tag{2.6.12}$$

where the $\delta^{(n)}$ terms are the same as those in the PPF model, with the key difference that all fields now have support only for $k \leq \Lambda$. The field $\delta_{\mathbf{k}}^{\mathrm{stoch}}$ only correlates with itself, its power spectrum is given in (2.6.8). One can find that, at leading order, $\delta_{\mathbf{k}}^{\mathrm{stress}}$ can be expressed as:

$$\delta_{\mathbf{k}}^{\mathrm{stress}} = -\gamma_\Lambda k^2 \delta_{\mathbf{k}}^{(1)} \tag{2.6.13}$$

In the end, the total matter power spectrum at one-loop order is given by:

$$P_{\text{non-linear}}(k) = P_{11}(k,\eta) + P_{22}^{\Lambda}(k,\eta) + P_{13}^{\Lambda}(k,\eta) - 2\gamma_\Lambda k^2 P_{11}(k,\eta) + P_J(k). \tag{2.6.14}$$

Now, let's see how these corrections help renormalize the one-loop power spectrum by isolating and absorbing UV-sensitive contributions. First of all, in this context, it is crucial to distinguish between the bare and renormalized parameters. The bare parameters, such as γ_Λ and R_{stoch}, contain both infinite terms (dependent on the cutoff Λ) and finite terms that encapsulate the physical UV effects. These infinite terms stem from the short-wavelength modes which are not directly accessible within the EFT, while the finite terms correspond to modes where the EFT holds. Therefore, the loop integrals are split into two components: the Λ-dependent part, which we do not trust, and the calculable part that is evaluated over the regimes where the EFT is valid.

We define a wavenumber q_{trust} such that the loop integrals are split based on whether q lies below or above this threshold. First, let us consider the contribution from the P_{13} term, given by

$$\begin{aligned} P_{13}^{\Lambda} =& 6P_{11}(k) \int_{q \leq q_{\mathrm{trust}}} \frac{d^3q}{(2\pi)^3} F_3(\mathbf{k}, \mathbf{q}, -\mathbf{q}) P_L(q) \\ &+ 6P_{11}(k) \int_{q_{\mathrm{trust}} \leq q \leq \Lambda} \frac{d^3q}{(2\pi)^3} F_3(\mathbf{k}, \mathbf{q}, -\mathbf{q}) P_L(q). \end{aligned} \tag{2.6.15}$$

Assuming $\Lambda > q_{\mathrm{trust}} \gg k$, we can simplify the second term using the ultraviolet limit (2.5.4), yielding

$$6P_{11}(k)\int_{q_{\rm trust}\le q\le\Lambda}\frac{d^3q}{(2\pi)^3}\,F_3(\mathbf{k},\mathbf{q},-\mathbf{q})P_L(q)=-\frac{61}{630\pi^2}k^2P_L(k)\int_{q_{\rm trust}}^{\Lambda}dqP_L(q). \tag{2.6.16}$$

This term, as $\Lambda\to\infty$, potentially diverges. However, the divergence can be cancelled by an appropriate choice of γ_Λ, where

$$\gamma_\Lambda=\gamma_{\rm finite}-\frac{61}{1260\pi^2}\int_{q_{\rm trust}}^{\Lambda}P_L(q)\,dq. \tag{2.6.17}$$

Thus, the physical contribution to P_{13} becomes independent of Λ, and we obtain

$$P_{13}^{\Lambda}-2\gamma_\Lambda k^2P_L=-2\gamma_{\rm finite}k^2P_{11}+6P_{11}(k)\int_{q\le q_{\rm trust}}\frac{d^3q}{(2\pi)^3}\,F_3(\mathbf{k},\mathbf{q},-\mathbf{q})P_L(q) \tag{2.6.18}$$

This equation illustrates that the effective sound speed renormalizes the P_{13} loop, and in practice, this allows us to choose any value of Λ, including $\Lambda=\infty$. A similar calculation shows that the P_{22} correction is successfully renormalized by the noise term P_J:

$$\begin{aligned}P_{22}^{\Lambda}+P_J=&2\int_{q\le q_{\rm trust}}\frac{d^3q}{(2\pi)^3}\,\left[F_2(\mathbf{k}-\mathbf{q},\mathbf{q})\right]^2P_L(q)P_L(|\mathbf{k}-\mathbf{q}|)\\&+2\int_{q_{\rm trust}<q\le\Lambda}\frac{d^3q}{(2\pi)^3}\,\left[F_2(\mathbf{k}-\mathbf{q},\mathbf{q})\right]^2P_L(q)P_L(|\mathbf{k}-\mathbf{q}|)+P_J.\end{aligned} \tag{2.6.19}$$

At leading order, this simplifies to:

$$2\int_{q\le q_{\rm trust}}\frac{d^3q}{(2\pi)^3}\left[F_2(\mathbf{k}-\mathbf{q},\mathbf{q})\right]^2P_L(q)P_L(|\mathbf{k}-\mathbf{q}|)+k^4\left[\frac{9}{196\pi^2}\int_{q_{\rm trust}}^{\Lambda}\frac{dq}{q^2}P_L^2(q)+R^7_{\rm stoch}\right].$$

The counterterms now include finite and stochastic components, and we define the renormalized P_{22}^{Λ} as:

$$P_{22}^{\Lambda}+P_J=2\int_{q\le q_{\rm trust}}\frac{d^3q}{(2\pi)^3}\,\left[F_2(\mathbf{k}-\mathbf{q},\mathbf{q})\right]^2P_L(q)P_L(|\mathbf{k}-\mathbf{q}|)+\left(R^{\rm finite}_{\rm stoch}\right)^7\,k^4. \tag{2.6.20}$$

Collecting the results, the renormalized power spectrum at one-loop order is;

$$\begin{aligned} P_{\text{non-linear}}(k) =& P_L(k) + 2\int_{q,q\leq q_{\text{trust}}} \frac{d^3q}{(2\pi)^3}\,\left[F_2(\mathbf{k}-\mathbf{q},\mathbf{q})\right]^2 P_L(q)P_L(|\mathbf{k}-\mathbf{q}|) \\ &+ 6P_L(k)\int_{q,q\leq q_{\text{trust}}} \frac{d^3q}{(2\pi)^3}\,F_3(\mathbf{k},\mathbf{q},-\mathbf{q})P_L(q) - 2\gamma_{\text{finite}}k^2P_L(k) \\ &+ \left(R^{\text{stoch}}_{\text{finite}}\right)^7\,k^4, \end{aligned} \tag{2.6.21}$$

where q_{trust} is typically chosen around $0.3\,h\,\text{Mpc}^{-1}$ for redshifts $z\sim 0.5$. Notably, the one-loop integrals become saturated around k_{eq} for the ΛCDM spectrum, and beyond this scale, the choice of q_{trust} becomes irrelevant, allowing us to set $q_{\text{trust}}=\infty$.

IR Resummation

The issue of IR singularities, discussed in section 2.5, is properly addressed using an alternative approach to conventional perturbation theory, namely the Time-Sliced Perturbation Theory (TSPT). TSPT involves two main steps: (i) evolving the probability distribution function (PDF) for the perturbations from the initial time to a given redshift, and (ii) performing statistical averaging over the evolved fields. This approach systematically handles large contributions from IR modes in non-linear regimes by resumming enhanced terms and achieving IR safety.
A significant advantage of TSPT is that it can be expanded to higher-order functions, systematically addressing any degree of infrared enhancement. This is particularly important for understanding the behavior of baryon acoustic oscillations in the large-scale structure. Moreover, TSPT is both IR and UV safe, meaning it avoids the unphysical divergences typically encountered in other perturbative approaches, such as those seen previously. More details on this can be found in [15, 17].
In this framework, the result for IR resummation at one-loop order is given by:

$$\begin{aligned} P^{\text{IR-res}}_{\text{LO}}(k) &= P^{nw}_L(k) + e^{-k^2\Sigma^2}P^w_L, \\ P^{\text{IR-res}}_{\text{NLO}}(k) &= P^{nw}_L(k) + P^{nw}_{\text{1-loop}}(k) + e^{-k^2\Sigma^2}\left[\left(1+k^2\Sigma^2\right)P^w_L + P^w_{\text{1-loop}}\right]. \end{aligned} \tag{2.6.22}$$

This equation represents the IR-resummed matter power spectrum at the one-loop order, where P^{nw} corresponds to the smooth (non-oscillatory) power

spectrum, and P^w refers to the wiggly (oscillatory) component. The factor $e^{-\Sigma^2 k^2}$ acts as the IR damping factor, suppressing contributions from small scales. Meanwhile, the integral $P_{1-\text{loop}}$ incorporates loop corrections that refine the estimation of the matter power spectrum.
This resummation method extends beyond the leading order of perturbation theory, thereby improving the description of the matter power spectrum at large scales where IR modes play a significant role.

2.7 Galaxy Bias and Redshift Space Distortions

Until now, we have focused on dark matter in real-space coordinates. However, in spectroscopic galaxy surveys, we observe galaxies that trace the underlying matter distribution in a nonlinear fashion. The galaxy positions are inferred from their observed redshifts, which are affected by peculiar velocities, i.e., the motion of galaxies relative to the Hubble flow. These peculiar velocities introduce additional non-linearities that must be accounted for in the model. In this section, we discuss these effects in more detail, following the reference [18], where further details can be found.

To describe the one-loop power spectrum for biased tracers, we need to consider all relevant operators up to third order in the bias expansion. The bias expansion allows us to model how galaxies, as biased tracers of the underlying matter field, respond to variations in the matter density:

$$\delta_g = b_1\delta + \epsilon + \frac{b_2}{2}\delta^2 + b_{\mathcal{G}_2}\mathcal{G}_2 + \frac{b_3}{6}\delta^3 + b_{\delta\mathcal{G}_2}\delta\mathcal{G}_2 + b_{\mathcal{G}_3}\mathcal{G}_3 + b_{\Gamma_3}\Gamma_3 + R_*^2\partial^2\delta, \quad (2.7.1)$$

where ϵ represents the stochastic contribution, which is uncorrelated with the large-scale density field. The terms $\mathcal{G}_2$, $\mathcal{G}_3$, and Γ_3 are higher-order operators capturing tidal and non-local effects that become important at nonlinear scales. At one-loop order, the terms δ^3, $\delta\mathcal{G}_2$ and $\mathcal{G}_3$ do not introduce new k-dependencies and can therefore be absorbed into the bias parameters of lower-order terms. The last term, $R_*^2\nabla^2\delta$, represents higher-derivative corrections arising from the finite size of galaxy-forming regions, leading to scale-dependent modifications in the bias expansion. These effects become significant on small scales and can be regarded as a third-order contribution in the expansion of $\delta^{(3)}$. This follows from the fact that each spatial derivative introduces an additional factor of k/k_{NL} in Fourier space, which is a small

quantity at large scales due to $k \ll k_{\rm NL}$, where $k_{\rm NL}$ denotes the wavenumber at which density fluctuations become nonlinear. Since δ is already small on large scales, the term $R_*^2\nabla^2\delta$ is naturally suppressed and enters at higher order in the perturbative expansion. For further discussion on the estimates and constraints on R_* for different tracers, see [19].

The Galileon operator $\mathcal{G}_2$ is defined as:

$$\mathcal{G}_2(\Phi_g) \equiv (\partial_i\partial_j\Phi_g)^2 - (\partial_i^2\Phi_g)^2, \tag{2.7.2}$$

where Φ_g is the gravitational potential. The only cubic operator that contributes non trivially to the one-loop power spectrum is:

$$\Gamma_3 \equiv \mathcal{G}_2(\Phi_g) - \mathcal{G}_2(\Phi_v), \tag{2.7.3}$$

where Φ_v is the velocity potential, which, in linear theory, is identical to Φ_g, but they differ at higher-order perturbations.

For further details on the definition of $\mathcal{G}_3$ and the derivation of the full bias expansion, please refer to [20].

Power Spectrum Corrections

Using the above expansion, the one-loop galaxy power spectrum is given by:

$$\begin{aligned} P_{\rm gg}(z,k) = {} & b_1^2(z)\left(P_L(z,k) + P_{1-\text{loop,SPT}}(z,k)\right) + b_1(z)b_2(z)\mathcal{I}_{\delta^2}(z,k) \\ & + 2b_1(z)b_{\mathcal{G}_2}(z)\mathcal{I}_{\mathcal{G}_2}(z,k) + b_1(z)\left(2b_{\mathcal{G}_2}(z) + \frac{4}{5}b_{\Gamma_3}(z)\right)\mathcal{F}_{\mathcal{G}_2}(z,k) \\ & + \frac{1}{4}b_2^2(z)\mathcal{I}_{\delta^2\delta^2}(z,k) + b_{\mathcal{G}_2}^2(z)\mathcal{I}_{\mathcal{G}_2\mathcal{G}_2}(z,k) + b_2(z)b_{\mathcal{G}_2}(z)\mathcal{I}_{\delta^2\mathcal{G}_2}(z,k) \\ & + P_{\nabla^2\delta}(z,k) + P_{\epsilon\epsilon}(z,k), \end{aligned} \tag{2.7.4}$$

This expression requires calculating various integrals, including the linear power spectrum and the kernel function F_2.

It is worth noting that contributions from operators like δ^3, $\delta\mathcal{G}_2$, and $\mathcal{G}_3$ vanish after renormalization, so the bias parameters b_3, $b_{\delta\mathcal{G}_2}$, and $b_{\mathcal{G}_3}$ do not appear in Eq. (2.7.4). Renormalization is the process of absorbing divergent or redundant contributions into redefined parameters, ensuring that only physically meaningful quantities remain in the final expressions. This means that higher-order bias terms that are not independent after loop corrections can be systematically removed or absorbed into lower-order bias parameters.

Next, we examine the effects of redshift-space distortions (RSD) on the galaxy power spectrum. RSD arise due to the peculiar velocities of galaxies along the line of sight, which cause distortions in the observed galaxy positions in spectroscopic surveys. To model these distortions, we assume the flat-sky plane-parallel approximation, which simplifies the geometry of the problem. In this approximation, the redshift-space mapping can be fully characterized by the projection of the 3D galaxy distribution onto the 2D sky plane. Specifically, the mapping is described by the cosine of the angle between the line-of-sight $\hat{\mathbf{z}}$ and the wavevector $\mathbf{k}$ of a given Fourier mode, given by $\mu \equiv (\hat{\mathbf{z}} \cdot \mathbf{k})/k$. This quantity μ represents the directional component of the wavevector along the line of sight, which is crucial for understanding how redshift-space distortions influence the observed power spectrum. The redshift-space distortions depend on both the position of the galaxy in real space and its peculiar velocity along the line of sight, affecting the overall shape and amplitude of the power spectrum. Under this assumption, the one-loop redshift-space power spectrum is given by (see [21, 22]):

$$\begin{aligned} P_{\text{gg, RSD}}(z,k,\mu) = Z_1^2(\mathbf{k})P_L(z,k) + 2\int_{\mathbf{q}} Z_2^2(\mathbf{q},\mathbf{k}-\mathbf{q})P_L(z,|\mathbf{k}-\mathbf{q}|)P_L(z,q) \\ + 6Z_1(\mathbf{k})P_L(z,k)\int_{\mathbf{q}} Z_3(\mathbf{q},-\mathbf{q},\mathbf{k})P_L(z,q) \\ + P_{\text{ctr, RSD}}(z,k,\mu) + P_{\epsilon,\text{RSD}}(z,k,\mu), \end{aligned} \tag{2.7.5}$$

where $\int_{\mathbf{q}} = \int \frac{d^3q}{(2\pi)^3}$.
The redshift-space kernels are given by:

$$Z_1(\mathbf{k}) = b_1 + f\mu^2, \tag{2.7.6}$$

commonly referred as Kaiser factor,

$$\begin{aligned} Z_2(\mathbf{k}_1,\mathbf{k}_2) = \frac{b_2}{2} + b_{\mathcal{G}_2}\left(\frac{(\mathbf{k}_1\cdot\mathbf{k}_2)^2}{k_1^2k_2^2} - 1\right) + b_1F_2(\mathbf{k}_1,\mathbf{k}_2) + f\mu^2G_2(\mathbf{k}_1,\mathbf{k}_2) \\ + \frac{f\mu k}{2}\left(\frac{\mu_1}{k_1}(b_1 + f\mu_2^2) + \frac{\mu_2}{k_2}(b_1 + f\mu_1^2)\right), \end{aligned} \tag{2.7.7}$$

$$\begin{aligned} Z_3(\mathbf{k}_1,\mathbf{k}_2,\mathbf{k}_3) = 2b_{\Gamma_3}\left[\frac{(\mathbf{k}_1\cdot(\mathbf{k}_2+\mathbf{k}_3))^2}{k_1^2(\mathbf{k}_2+\mathbf{k}_3)^2} - 1\right][F_2(\mathbf{k}_2,\mathbf{k}_3) - G_2(\mathbf{k}_2,\mathbf{k}_3)] \\ + b_1F_3(\mathbf{k}_1,\mathbf{k}_2,\mathbf{k}_3) + f\mu^2G_3(\mathbf{k}_1,\mathbf{k}_2,\mathbf{k}_3) + \frac{(f\mu k)^2}{2}(b_1 + f\mu_1^2)\frac{\mu_2\mu_3}{k_2k_3} \\ + f\mu k\frac{\mu_3}{k_3}\left[b_1F_2(\mathbf{k}_1,\mathbf{k}_2) + f\mu_{12}^2G_2(\mathbf{k}_1,\mathbf{k}_2)\right] + f\mu k(b_1 + f\mu_1^2)\frac{\mu_{23}}{k_{23}}G_2(\mathbf{k}_2,\mathbf{k}_3) \end{aligned}$$

$$+ b_2 F_2(\mathbf{k}_1, \mathbf{k}_2) + 2b_{\mathcal{G}_2}\left[\frac{(\mathbf{k}_1 \cdot (\mathbf{k}_2 + \mathbf{k}_3))^2}{k_1^2(\mathbf{k}_2 + \mathbf{k}_3)^2} - 1\right] F_2(\mathbf{k}_2, \mathbf{k}_3)$$
$$+ \frac{b_2 f\mu k}{2}\frac{\mu_1}{k_1} + b_{\mathcal{G}_2} f\mu k \frac{\mu_1}{k_1}\left[\frac{(\mathbf{k}_2 \cdot \mathbf{k}_3)^2}{k_2^2 k_3^2} - 1\right], \tag{2.7.8}$$

where $\mathbf{k} = \mathbf{k}_1 + \mathbf{k}_2 + \mathbf{k}_3$.
It is important to note that $Z_3(\mathbf{k}_1, \mathbf{k}_2, \mathbf{k}_3)$ only includes the bias parameters that contribute non trivially to the redshift-space one-loop power spectrum, and it must be symmetrized over its momentum arguments when used in Eq. (2.7.5).
For clarity, the time dependence of f and the biases is omitted here.

Now, let's consider the final terms in Eq. (2.7.5). The leading counterterm contributions in redshift space can be seen as a simple generalization of the dark matter sound speed [21]:

$$\begin{aligned} P_{\text{ctr, RSD},\nabla^2\delta}(z, k, \mu) = &- 2\tilde{c}_0(z) k^2 P_L(z, k) - 2\tilde{c}_2(z) f(z) \mu^2 k^2 P_L(z, k) \\ &- 2\tilde{c}_4(z) f^2(z) \mu^4 k^2 P_L(z, k), \end{aligned} \tag{2.7.9}$$

where $\tilde{c}_0(z)$, $\tilde{c}_2(z)$, and $\tilde{c}_4(z)$ are quantities that are expected to be of similar magnitude to the real-space dark matter sound speed in units of $[\text{Mpc}/h]^2$.

Due to the Finger of God effect [23], certain counterterms can be more significant for some tracers than initially expected. This effect is caused by the peculiar velocities of galaxies within clusters, resulting in distortions along the line of sight in redshift space. These distortions, especially at small scales, contribute to the non-linearities in the galaxy distribution. It is induced by higher-derivative terms in the non-linear redshift space distortion mapping. To account for this, an additional counterterm proportional to $k^4\mu^4 P_L(z, k)$ can be included as a proxy for these higher-order contributions caused by peculiar motions:

$$P_{\text{ctr, RSD},\nabla^4_{\mathbf{z}}\delta}(z, k, \mu) = -\tilde{c}(z) f^4(z) \mu^4 k^4 \left(b_1(z) + f(z)\mu^2\right)^2 P_L(z, k), \tag{2.7.10}$$

We emphasize that including this term is crucial for fitting the data or the results from N-body simulations, especially when Finger of God effects are pronounced.
The full counterterm contribution is given by

$$P_{\text{ctr, RSD}}(z,k,\mu) = P_{\text{ctr, RSD},\nabla^2\delta}(z,k,\mu) + P_{\text{ctr, RSD},\nabla^4_{\hat{\mathbf{z}}}\delta}(z,k,\mu), \tag{2.7.11}$$

and depends on four free functions of time $\tilde{c}_0(z), \tilde{c}_2(z), \tilde{c}_4(z)$, and $\tilde{c}(z)$.

Finally, the stochastic power spectrum in redshift space at next-to-leading order in the derivative expansion is given by

$$P_{\epsilon\epsilon,\text{RSD}}(z,k,\mu) = P_{\text{shot}}(z) + a_0(z)k^2 + a_2(z)\mu^2k^2, \tag{2.7.12}$$

where P_{shot} describes constant shot noise, and the additional two terms are scale-dependent shot noise contributions to the monopole and the quadrupole. The coefficients a_0 and a_2 are time-dependent, and the k and μ dependence of the stochastic power spectrum is simple. Note that the pair-counting Poissonian contribution $1/\bar{n}$ is often subtracted from the power spectrum estimator, but it is important to retain the residual constant P_{shot} in the model to account for deviations from the Poissonian prediction.

While all terms should be included in a data analysis for consistency, some contributions are quite degenerate at the galaxy power spectrum level. For example, the $P_{\text{ctr, RSD},\nabla^4_{\hat{\mathbf{z}}}\delta}$ counterterm is degenerate with the $a_2\mu^2k^2$ stochastic contribution due to the slope of the linear power spectrum on mildly non-linear scales. Thus, for precision, one can choose to retain only one of the two terms. As shown in Ref. [24], the a_0 contribution can be neglected for scales where $k \lesssim 0.3\,h/\text{Mpc}$.

We have now presented the perturbation theory model for the redshift-space power spectrum, keeping the full k and μ dependence. However, it is often more convenient to summarize the full angular information in a few multipoles, using the relation:

$$P_{\text{gg, RSD}}(z,k,\mu) = \sum_{\ell \text{ even}} \mathcal{L}_\ell(\mu) P_\ell(z,k), \tag{2.7.13}$$

where $\mathcal{L}_\ell(\mu)$ are Legendre polynomials. The galaxy power spectrum multipoles are then defined as

$$P_\ell(z,k) \equiv \frac{2\ell+1}{2}\int_{-1}^{1} d\mu\, \mathcal{L}_\ell(\mu) P_{\text{gg, RSD}}(z,k,\mu), \tag{2.7.14}$$

and their detailed expressions can be found in [18].

Bispectrum Corrections

Analogously, for the tree-level bispectrum in redshift space, we replace $F_2 \to Z_2$ and $P_L \to Z_1 P_L$ in Eq. (2.4.17), resulting in:

$$B(\mathbf{k}_1, \mathbf{k}_2, \mathbf{k}_3) = 2Z_2(\mathbf{k}_1, \mathbf{k}_2)Z_1(\mathbf{k_1})Z_1(\mathbf{k_2})P_L(k_1)P_L(k_2) + 2\,\text{cyc.} \tag{2.7.15}$$

For more details on the stochastic and counterterm corrections, we refer the reader to [25]. In this work, we only include the stochastic contribution:

$$\begin{aligned} B_{\text{stoch}}(\mathbf{k}_1, \mathbf{k}_2, \mathbf{k}_3) = Z_1(\mathbf{k}_1)\frac{P_{11}(k_1)}{\bar{n}}\left(b_1 B_{\text{shot}} + f\mu^2(1 + P_{\text{shot}})\right) \\ + \frac{1 + A_{\text{shot}}}{\bar{n}^2} + \text{cyc}, \end{aligned} \tag{2.7.16}$$

where A_{shot}, B_{shot}, and P_{shot} are free $\mathcal{O}(1)$ shot-noise parameters that account for deviations from Poissonian stochasticity.
It is important to note that mathematical consistency requires the parameter P_{shot} to be the same as the one appearing in the power spectrum model.

2.8 Primordial Non-Gaussianity

In this section, we briefly discuss how primordial non-Gaussianity (PNG) can be incorporated, which is an important feature for addressing key questions about inflation, such as: how many degrees of freedom were responsible for generating density fluctuations, and how fast did these degrees of freedom propagate? The simplest observable signature of PNG is the bispectrum, B_ζ, of the primordial metric curvature perturbation ζ. Due to the translational and rotational invariance, B_ζ depends only on the moduli of the three momenta, $\mathbf{k}_1$, $\mathbf{k}_2$, and $\mathbf{k}_3$, which form a closed triangle. A bispectrum that peaks at squeezed triangles, $k_1 \ll k_2 \approx k_3$, is a typical signature of particle interactions in multi-field inflation, where multiple degrees of freedom are light during inflation. This type of PNG is referred to as "local" PNG. In contrast, a bispectrum peaking at equilateral triangles ($k_1 \approx k_2 \approx k_3$) or flattened triangles ($k_1 \approx k_2 \approx k_3/2$) is a characteristic feature of interactions in single-field inflation, which involves only one degree of freedom (the inflaton). This kind of non-local primordial non-Gaussianity (NLPNG) can be described as a linear combination of two basis shapes, equilateral and orthogonal [26], with amplitudes f_{NL}^{equil} and f_{NL}^{ortho}, respectively.

In this work, we focus on NLPNG. Symmetries of inflation also establish a relationship between the inflaton's speed of sound and the strength of the nonlinear interactions that generate NLPNG [27]. This relationship allows one to constrain the propagation speed of the inflaton from the observed level of NLPNG. Analysis of CMB data, particularly from the Planck 2018 mission, provides the following constraints: $f_{NL}^{\rm equil} = -26 \pm 47$ and $f_{NL}^{\rm ortho} = -38 \pm 24$ (both at 68% confidence level) [28].
In principle, tighter constraints can be obtained from upcoming galaxy surveys, though analyzing this data is more complex due to the weak effect of PNG in the galaxy distribution, which is overlaid on an intrinsic late-time non-Gaussian signal generated by the nonlinear clustering of matter. The dominant effect of NLPNG on galaxy clustering is a specific shape dependence in the galaxy bispectrum, which also modifies the power spectra through loop corrections.

A general single-field Lagrangian for the inflaton perturbation π with leading interactions up to cubic order is given by [27]

$$S = \int d^4x\sqrt{-g}\left[-\frac{M_{\rm Pl}^2\dot{H}}{c_{\pi,s}^2}\left(\dot{\pi}^2 - c_{\pi,s}^2\frac{(\partial_i\pi)^2}{a^2}\right) - M_{\rm Pl}^2\dot{H}(1-c_{\pi,s}^{-2})\dot{\pi}\frac{(\partial_i\pi)^2}{a^2}\right. \\ \left. + \left(M_{\rm Pl}^2\dot{H}(1-c_{\pi,s}^{-2}) - \frac{4}{3}M_3^4\right)\dot{\pi}^3\right], \tag{2.8.1}$$

with the scalar perturbation π being related to the curvature perturbation $\zeta = -H\pi$. The higher order interactions of the inflaton field give rise to a primordial bispectrum for the curvature perturbation $B_\zeta(k_1, k_2, k_3)$ that can be expressed using a linear combination of the orthogonal and equilateral templates. We define

$$B_\zeta(k_1, k_2, k_3) = \frac{18}{5}f_{NL}\Delta_\zeta^4\frac{S(k_1, k_2, k_3)}{k_1^2k_2^2k_3^2}, \tag{2.8.2}$$

with the equilateral and orthogonal templates defined as [26]

$$S_{\rm eq}(k_1, k_2, k_3) = \left(\frac{k_1}{k_2} + 5 \text{ perms.}\right) - \left(\frac{k_1^2}{k_2k_3} + 2 \text{ perms.}\right) - 2, \tag{2.8.3}$$

$$S_{\rm ort}(k_1, k_2, k_3) = (1+p)\frac{\Delta}{e_3} - p\frac{\Gamma^3}{e_3^2}, \tag{2.8.4}$$

where $p = 8.52587$, $\Delta = (k_T - 2k_1)(k_T - 2k_2)(k_T - 2k_3)$,

$$k_T = k_1 + k_2 + k_3, \quad e_2 = k_1k_2 + k_1k_3 + k_2k_3, \quad e_3 = k_1k_2k_3, \tag{2.8.5}$$
$$\Gamma = \frac{2}{3}e_2 - \frac{1}{3}\left(k_1^2 + k_2^2 + k_3^2\right).$$

The PNG affects the late-time dark matter distribution, inducing an additional bispectrum term given by

$$\langle \delta^{(1)}\delta^{(1)}\delta^{(1)} \rangle = f_{\rm NL} B_{111}(k_1, k_2, k_3)(2\pi)^3 \delta_D(\mathbf{k}_{123}), \tag{2.8.6}$$

with

$$f_{\rm NL} B_{111}(k_1, k_2, k_3) = \mathcal{T}(k_1)\mathcal{T}(k_2)\mathcal{T}(k_3) B_\zeta(k_1, k_2, k_3), \tag{2.8.7}$$

where we have introduced the transfer function

$$\mathcal{T}(k) \equiv \frac{\delta^{(1)}(k)}{\zeta(k)} = \left(\frac{P_{11}(k)}{P_\zeta(k)}\right)^{1/2}. \tag{2.8.8}$$

Notice that this can be easily calculated via the definition of the power spectrum of initial fluctuations:

$$P_\zeta(k) = \Delta_\zeta^2 k^{-3} \left(\frac{k}{k_*}\right)^{n_s - 1}. \tag{2.8.9}$$

Analysis of Planck data finds $\Delta_\zeta^2 \simeq 4.1 \times 10^{-8}$, $n_s \simeq 0.96$ for the pivot scale $k_* = 0.05\,\mathrm{Mpc}^{-1}$ [29].
The initial bispectrum also enters the 1-loop galaxy power spectrum through the 1-2 term:

$$f_{\rm NL} P_{12}(\mathbf{k}) = 2 f_{\rm NL} Z_1(\mathbf{k}) \int_{\mathbf{q}} Z_2(\mathbf{k} - \mathbf{q}, \mathbf{q}) B_{111}(k, q, |\mathbf{k} - \mathbf{q}|), \tag{2.8.10}$$

where $Z_{1,2}$ are linear and quadratic galaxy redshift-space kernels (see Section 2.7). In addition, non-local PNG modulates galaxy formation, which is captured by the scale-dependent galaxy bias:

$$\delta_g = Z_1 \delta + f_{\rm NL} b_\zeta \left(\frac{k}{k_{\rm NL}}\right)^2 \zeta + \text{nonlinear}, \tag{2.8.11}$$

where b_ζ is an order-one PNG linear bias coefficient, and $k_{\rm NL}$ represents the nonlinear scale. The value of $k_{\rm NL}$ is conventionally determined by requiring that the dimensionless power spectrum satisfies

$$\Delta^2(k_{\rm NL}) = P_{11}(k_{\rm NL})\frac{k_{\rm NL}^3}{2\pi^2} = 1. \tag{2.8.12}$$

We obtain $k_{\rm NL} \approx 0.5\,{\rm h\ Mpc}^{-1}$ at the relevant redshift $z \simeq 0.5$. This definition provides an estimate of the transition scale between the linear and nonlinear regimes. Physically, it corresponds to the scale at which density fluctuations become of order unity, marking the breakdown of perturbation theory.

Thus, the final model for the galaxy power spectra and bispectra in redshift space is

$$P_g(\mathbf{k}) = P_{g,G}(k) + f_{\rm NL}\left(P_{12}(\mathbf{k}) + 2b_\zeta Z_1(k)\frac{k^2}{k_{\rm NL}^2}\frac{P_L(k)}{\mathcal{T}(k)}\right), \tag{2.8.13}$$

$$\begin{aligned} B_g(\mathbf{k}_1,\mathbf{k}_2,\mathbf{k}_3) =& B_{g,G}(\mathbf{k}_1,\mathbf{k}_2,\mathbf{k}_3) + \\ & f_{\rm NL}Z_1(k_1)Z_1(k_2)Z_1(k_3)B_{111}(k_1,k_2,k_3), \end{aligned} \tag{2.8.14}$$

where $P_{g,G}$ and $B_{g,G}$ are the standard Gaussian power spectrum and bispectrum models. In this work, we will assume that the following relation holds for the primordial non-Gaussian bias and the linear bias

$$b_\zeta = \frac{18}{5}\delta_c(b_1 - 1), \tag{2.8.15}$$

motivated by the peak-background split argument [30], with δ_c being the critical overdensity for the spherical collapse.

Chapter 3

The Marked Density Field

Galaxy surveys have advanced significantly in recent years, allowing for the study of the large-scale structure (LSS) of the Universe with unprecedented precision. In particular, current and upcoming LSS observations will provide access to a wealth of new cosmological information from non-linear scales in the galaxy density field.

In the previous sections, we established that the primary method of extracting information from the density contrast field is through the two-point correlator, namely the power spectrum $P(\mathbf{k})$. At early times, deviations from Gaussianity in the Universe are minimal, making the power spectrum a sufficient statistic that captures nearly all cosmological information. However, at later times, non-linear effects become prominent, leading to significant deviations from Gaussianity and redistributing information into higher-order statistics. To address this, two main approaches can be taken: (1) extending the analysis to higher-order statistics beyond the power spectrum, thereby incorporating non-Gaussian information; or (2) transforming the density field to construct an alternative two-point statistic that encodes this additional information. In the first case, the lowest-order extension is the three-point correlator, or bispectrum. The bispectrum has been extensively studied in the literature, e.g. [31, 25], but its application in cosmological parameter inference remains challenging. A key issue is that the bispectrum retains most of its information only at mildly non-linear scales. Extending the analysis to even higher-order moments, while desirable, presents significant computational challenges, particularly in realistic data analysis scenarios where evaluating covariances and including observational effects, such as window functions, is crucial.

An alternative approach is to apply transformations to the density field, which have been shown to effectively map higher-order information into two-point correlators. One such transformation that has gained considerable attention is the *marked density field*, a weighted version of the density field where the weight (or "mark") can encode various physical properties, such as galaxy attributes, halo merger history, or—as in this work—the local environmental density. Recent studies have demonstrated that the marked power spectrum can provide stronger cosmological constraints, particularly on neutrino mass [32] and modified gravity models [33], compared to the standard power spectrum. This enhanced constraining power arises from two key factors as emphasized in previous works [33, 34, 35, 36, 37] . First, by correlating the density field with its environment, the marked power spectrum effectively incorporates information from higher-order correlation functions. Second, the mark can be designed to up-weight low-density regions, which are expected to retain much of their initial cosmological information due to their reduced non-linear evolution. Additionally, low-density regions contribute minimally to the conventional power spectrum, making their inclusion particularly valuable.

Modeling marked statistics is, however, non-trivial. Most approaches involve non-linear transformations of the density field, whether for matter or biased tracers. These transformations must typically be expanded as a Taylor series to facilitate perturbative analysis. This poses difficulties, as the density field itself is inherently non-linear, and series convergence is not always guaranteed unless the field is sufficiently smoothed. The marked density contrast field, however, satisfies this criterion, as the weighting function—and hence its Taylor expansion—depends solely on the smoothed density field, whose variance can be parametrically controlled.
In this work, we follow [35] and present the one-loop perturbative description of the marked power spectrum $M(\mathbf{k})$ for general tracers in both real and redshift space, adding more details on its numerical implementation. Furthermore, we extend the results of [38], which incorporated primordial non-Gaussianity (PNG) into the perturbative description of the marked power spectrum in real space, to redshift space. These theoretical developments will be utilized in the next chapter to perform a Fisher matrix analysis.

3.1 Initial definitions

We begin with the definition of the marked density field,

$$\rho_M(\mathbf{x}) = m(\mathbf{x})\, n(\mathbf{x}) = m(\mathbf{x})\, \bar{n}\, [1 + \delta(\mathbf{x})] \tag{3.1.1}$$

where $\bar{n} = \langle n(\mathbf{x}) \rangle$ is the average density and $\delta(\mathbf{x})$ is the usual density contrast field. This applies in a general sense and can be used for any quantity, whether it's matter or biased tracers, and in real- or redshift-space.

As in [32], we define the mark $m(\mathbf{x})$ as:

$$m(\mathbf{x}) = \left(\frac{1 + \delta_s}{1 + \delta_s + \delta_R(\mathbf{x})} \right)^p, \tag{3.1.2}$$

where $\delta_R(\mathbf{x})$ is the density contrast field smoothed on scale R. It is the convolution of the smoothing kernel W_R with the unsmoothed density contrast field $\delta(\mathbf{x})$, given by:

$$\begin{aligned} \delta_R(\mathbf{x}) &= \int d^3x'\, W_R(\mathbf{x} - \mathbf{x}')\delta(\mathbf{x}') \\ &= \int d^3x'\, W_R(\mathbf{x} - \mathbf{x}') \left(\frac{\rho(\mathbf{x}') - \bar{\rho}}{\bar{\rho}} \right) \\ &= \frac{1}{\bar{\rho}} \left(\int d^3x'\, W_R(\mathbf{x} - \mathbf{x}')\rho(\mathbf{x}') - \bar{\rho} \int d^3x'\, W_R(\mathbf{x} - \mathbf{x}') \right), \end{aligned} \tag{3.1.3}$$

where the first term inside the parentheses represents the convolution of the window function $W_R(\mathbf{x} - \mathbf{x}')$ with the unsmoothed density $\rho(\mathbf{x}')$, which gives the smoothed density $\rho_R(\mathbf{x})$. The second term represents the integral over the kernel $W_R(\mathbf{x} - \mathbf{x}')$, which we assume to be normalized in order to preserve the mean density $\bar{\rho}$:

$$\int d^3x'\, W_R(\mathbf{x} - \mathbf{x}') = 1.$$

Thus, the final expression for the smoothed density contrast is:

$$\delta_R(\mathbf{x}) = \frac{\rho_R(\mathbf{x}) - \bar{\rho}}{\bar{\rho}}. \tag{3.1.4}$$

Next, we work in Fourier space, where we use a Gaussian window function $W_R(k) = e^{-k^2R^2/2}$.[1] . In this case, the relation between the smoothed and unsmoothed density contrast fields becomes:

$$\delta_R(\mathbf{k}) = W_R(k)\delta(\mathbf{k}). \tag{3.1.5}$$

The exponent p, the offset δ_s and the smoothing R of the mark are model hyperparameters. The case where $\delta_s \to 0$ is particularly insightful, as it leads to $m(\mathbf{x}) \to [\bar{\rho}/\rho_R(\mathbf{x})]^p$. In this scenario, it's evident that positive values of p increase the weight of points in low-density regions, while negative values of p give more weight to points in high-density areas. An example of the effects of the application of the mark can be seen in Fig. 3.1. It's worth noting that enhancing the weight in low-density regions is conceptually similar to studying the properties of voids, which are often used as probes for modified gravity (e.g., [39]), but without the need to identify voids.
To convert Eq. (3.1.1) into a contrast density field, we first need to compute the mean density. This is given by:

$$\langle \rho_M(\mathbf{x}) \rangle = \langle n(\mathbf{x}) m(\mathbf{x}) \rangle = \bar{n}\bar{m}, \tag{3.1.6}$$

where we have defined $\bar{m} = \frac{\langle n(\mathbf{x}) m(\mathbf{x}) \rangle}{\langle n(\mathbf{x}) \rangle}$, which represents the average of $m(\mathbf{x})$ weighted by the number density field $n(\mathbf{x})$ and that can be measured from simulations or data.
So, the marked density contrast field is given by:

$$\delta_M(\mathbf{x}) \equiv \frac{\rho_M(\mathbf{x}) - \langle \rho_M \rangle}{\langle \rho_M \rangle} = \frac{1}{\bar{m}} m(\mathbf{x}) \left[1 + \delta(\mathbf{x})\right] - 1. \tag{3.1.7}$$

3.2 Perturbative Framework

We proceed by expanding the marked contrast density field in powers of the linear density field $\delta^{(1)}(\mathbf{x})$, which will enable us to compute the power spectra perturbatively. Our goal is to develop a theory at one-loop accuracy, which requires an expansion up to third order in $\delta^{(1)}(\mathbf{x})$. To achieve this,

[1] The Gaussian window function is chosen due to its smoothness and suppression of small-scale fluctuations, efficient Fourier transform properties (the Fourier transform of a Gaussian is also a Gaussian), and its ability to reduce ultraviolet (UV) divergences, which improves the convergence of perturbation theory.

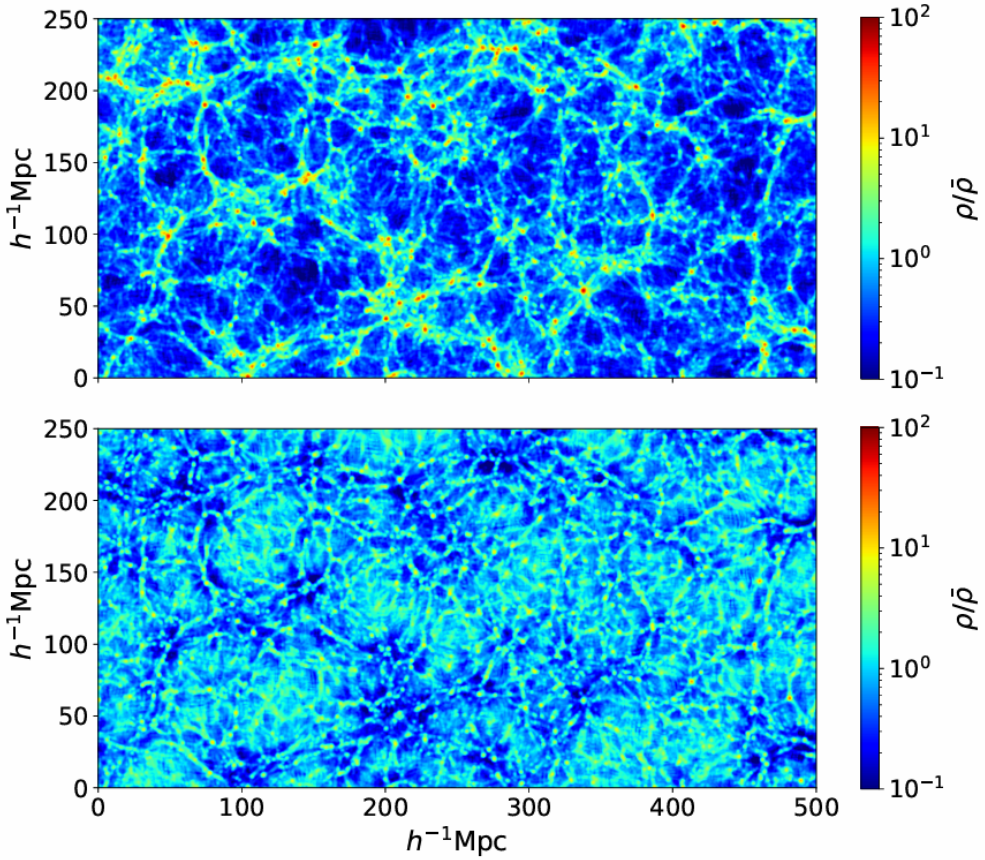

Figure 3.1: Projections in a region of $500 \times 250 \times 20\,(h^{-1}\mathrm{Mpc})^3$ of a simulation with fiducial cosmology at z = 0. Top panel shows the projected matter density field and bottom panel displays the marked density field with parameters $R = 10\,h^{-1}\,\mathrm{Mpc}$, $p = 2$, and $\delta_s = 0.25$. Here we show how the large-scale structure looks like in a marked field with positive p: high density regions are down weighted, while low density regions are up-weighted. Image taken from [32].

we approximate the mark $m(\mathbf{x})$ using its Taylor series expansion in terms of $\delta_R(\mathbf{x})$.

$$\begin{aligned} m(\mathbf{x}) &= 1 - \frac{p}{1+\delta_s}\delta_R(\mathbf{x}) + \frac{p(p+1)}{2(1+\delta_s)^2}\delta_R^2(\mathbf{x}) - \frac{p(p+1)(p+2)}{6(1+\delta_s)^3}\delta_R^3(\mathbf{x}) + \mathcal{O}(\delta_R^4) \\ &\equiv 1 - C_1\delta_R(\mathbf{x}) + C_2\delta_R^2(\mathbf{x}) - C_3\delta_R^3(\mathbf{x}) + \mathcal{O}(\delta_R^4), \end{aligned} \tag{3.2.1}$$

where the coefficients $C_n \equiv \binom{p+n-1}{p-1}(1+\delta_s)^{-n}$ encapsulate the dependence on the mark parameters p and δ_s. This decomposition, along with all subsequent formulas, is applicable to any mark function that depends solely on δ_R, with the Taylor coefficients $\{C_n\}$ suitably defined. The condition for the Taylor expansion to converge is:

$$\left|\frac{\delta_R(\mathbf{x})}{1+\delta_s}\right| < 1. \tag{3.2.2}$$

Since the fluctuation scale of δ_R is the usual variance $\sigma_{RR}^2(z) = \langle\delta^2(\mathbf{x})\rangle$, convergence is expected if:

$$\sigma_{RR}(z) \lesssim (1+\delta_s). \tag{3.2.3}$$

At high redshifts, where $\sigma_{RR}(z)$ is small, convergence is expected for $\delta_s \lesssim 0$, though this is not guaranteed at later times, and will depend on the choice of R and δ_s.[2] For biased tracers in real space, assuming R is large enough, we can approximate $\delta_R(z) \sim b_1(z)D(z)$ for linear bias b_1 and growth factor $D(z)$, leading to the condition:

$$b_1(z)D(z)\sigma_{RR}(0) < 1 + \delta_s. \tag{3.2.4}$$

Here, $\sigma_{RR}(0)$ represents the variance of the matter field on scale R at redshift zero. For most biased tracers, $b_1(z) > 1$, making this a stricter bound compared to matter, and it is not necessarily alleviated by moving to higher redshift. Additionally, for (angle-averaged) biased tracers in redshift space, the condition becomes even more stringent:

$$\left(b_1^2(z) + \frac{2}{3}f(z)b_1(z) + \frac{1}{5}f^2(z)\right)^{1/2} D(z)\,\sigma_{RR}(0) < 1 + \delta_s, \tag{3.2.5}$$

[2]Technically, R must be at least as large as the non-linear scale $k_{\rm NL}^{-1}$ when $\delta_s = 0$, with a less stringent condition as δ_s increases.

where $f(z)$ is the growth rate, which is scale-independent in ΛCDM cosmologies without massive neutrinos.

Using the expansion of the mark (3.2.1), the marked density contrast field (3.1.7) can be written as:

$$\delta_M(\mathbf{x}) = \frac{1}{\bar{m}}\left[1+\delta(\mathbf{x})\right]\left[1 - C_1\delta_R(\mathbf{x}) + C_2\delta_R^2(\mathbf{x}) - C_3\delta_R^3(\mathbf{x})\right] - 1 + \mathcal{O}(\delta^4) \tag{3.2.6}$$

Now, we express this in terms of powers of the linear density field $\delta^{(1)}$. To do this, we first expand $\delta(\mathbf{x})$ and $\delta_R(\mathbf{x})$ perturbatively as:

$$\delta(\mathbf{x}) = \delta^{(1)}(\mathbf{x}) + \delta^{(2)}(\mathbf{x}) + \delta^{(3)}(\mathbf{x}) + \mathcal{O}\left[\delta^{(4)}(\mathbf{x})\right], \tag{3.2.7}$$

$$\delta_R(\mathbf{x}) = \delta_R^{(1)}(\mathbf{x}) + \delta_R^{(2)}(\mathbf{x}) + \delta_R^{(3)}(\mathbf{x}) + \mathcal{O}\left[\delta_R^{(4)}(\mathbf{x})\right], \tag{3.2.8}$$

Additionally, from Eq. (3.1.5), we know that $\delta_R^{(n)}(\mathbf{k}) = W_R(k)\delta^{(n)}(\mathbf{k})$. Using these with the Taylor expansion of the mark (3.2.1), the marked density contrast field (3.1.7) becomes:

$$\delta_M(\mathbf{x}) \equiv \left(\frac{1}{\bar{m}} - 1\right) + \frac{1}{\bar{m}}\left(\delta_M^{(1)}(\mathbf{x}) + \delta_M^{(2)}(\mathbf{x}) + \delta_M^{(3)}(\mathbf{x})\right), \tag{3.2.9}$$

with:

$$\begin{aligned}
\delta_M^{(1)}(\mathbf{x}) &= \left[\delta^{(1)} - C_1\,\delta_R^{(1)}\right](\mathbf{x}) \\
\delta_M^{(2)}(\mathbf{x}) &= \left[\delta^{(2)} - C_1\,\delta_R^{(2)} - C_1\,\delta_R^{(1)}\,\delta^{(1)} + C_2\,\delta_R^{(1)}\delta_R^{(1)}\right](\mathbf{x}) \\
\delta_M^{(3)}(\mathbf{x}) &= \Big[\delta^{(3)} - C_1\,\delta_R^{(3)} - C_1\,\delta_R^{(2)}\delta^{(1)} - C_1\,\delta_R^{(1)}\delta^{(2)} + 2C_2\,\delta_R^{(1)}\delta_R^{(2)} \\
&\quad + C_2\delta_R^{(1)}\delta_R^{(1)}\delta^{(1)} - C_3\delta_R^{(1)}\delta_R^{(1)}\delta_R^{(1)}\Big](\mathbf{x}).
\end{aligned} \tag{3.2.10}$$

In Fourier space, where we follow the convention established in Chapter 2, these products can be expressed as convolutions, defined by:

$$\begin{aligned}
[X * Y](\mathbf{k}) &= \int_{\mathbf{p}} X(\mathbf{p})Y(\mathbf{k}-\mathbf{p}), \\
[X * Y * Z](\mathbf{k}) &= \int_{\mathbf{p}_1,\mathbf{p}_2} X(\mathbf{p}_1)Y(\mathbf{p}_2)Z(\mathbf{k}-\mathbf{p}_1-\mathbf{p}_2),
\end{aligned} \tag{3.2.11}$$

where we again use the integral notation $\int_{\mathbf{p}} = \int \frac{d^3p}{(2\pi)^3}$. Remembering also the Eq. (3.1.5), we obtain:

$$\delta_M(\mathbf{k}) \equiv (2\pi)^3\delta_D(\mathbf{k})\left(\frac{1}{\bar{m}}-1\right)+\frac{1}{\bar{m}}\delta_M^{(1)}(\mathbf{k})+\delta_M^{(2)}(\mathbf{k})+\delta_M^{(3)}(\mathbf{k}), \tag{3.2.12}$$

with

$$\begin{aligned}
\delta_M^{(1)}(\mathbf{k}) &= \left[1-C_1W_R(k)\right]\delta^{(1)}(\mathbf{k}) \\
\delta_M^{(2)}(\mathbf{k}) &= \left[1-C_1W_R(k)\right]\delta^{(2)}(\mathbf{k}) - C_1\left[\delta^{(1)}*\delta_R^{(1)}\right](\mathbf{k}) + C_2\left[\delta_R^{(1)}*\delta_R^{(1)}\right](\mathbf{k}) \\
\delta_M^{(3)}(\mathbf{k}) &= \left[1-C_1W_R(k)\right]\delta^{(3)}(\mathbf{k}) + 2C_2\left[\delta_R^{(1)}*\delta_R^{(2)}\right](\mathbf{k}) - C_3\left[\delta_R^{(1)}*\delta_R^{(1)}*\delta_R^{(1)}\right](\mathbf{k}) \\
&\quad - C_1\left[\delta^{(1)}*\delta_R^{(2)}\right](\mathbf{k}) - C_1\left[\delta^{(2)}*\delta_R^{(1)}\right](\mathbf{k}) + C_2\left[\delta^{(1)}*\delta_R^{(1)}*\delta_R^{(1)}\right](\mathbf{k})
\end{aligned} \tag{3.2.13}$$

To proceed, we require expressions for $\delta^{(n)}$ in terms of the linear spectrum $\delta^{(1)}$. Assuming Einstein-de-Sitter (EdS) kernels, these take the standard form

$$\delta^{(n)}(\mathbf{k}) \equiv \int_{\mathbf{k}_1\ldots\mathbf{k}_n} Z_n(\mathbf{k}_1,...,\mathbf{k}_n)\,\delta^{(1)}(\mathbf{k}_1)...\delta^{(1)}(\mathbf{k}_n)\times(2\pi)^3\delta_D\left(\mathbf{k}_1+...+\mathbf{k}_n-\mathbf{k}\right), \tag{3.2.14}$$

where the Z_n kernels are the redshift space kernels seen in Sec. (2.7), and we adopt the shorthand $\int_{\mathbf{k}_1..\mathbf{k}_n} \equiv (2\pi)^{-3n}\int d\mathbf{k}_1...\int d\mathbf{k}_n$. Note that we have still assumed nothing about the form of the input field δ, thus the expressions in this section are relevant to any tracer with complexities such as redshift-space distortions (RSD) only appearing in the $\{Z_n\}$ kernels. Moreover, it is important to emphasize that we apply the mark transformation to the *redshift-space* field, rather than introducing redshift-space distortions (RSD) to the already marked field. This approach is justified, as the redshift-space field represents the directly observable quantity.
Inserting this definition into (3.2.13) gives analogous kernels, $\{H_n\}$, for the marked field, *i.e.*

$$\delta_M^{(n)}(\mathbf{k}) \equiv \int_{\mathbf{k}_1\ldots\mathbf{k}_n} H_n(\mathbf{k}_1,...,\mathbf{k}_n)\,\delta^{(1)}(\mathbf{k}_1)...\delta^{(1)}(\mathbf{k}_n)\times(2\pi)^3\delta_D\left(\mathbf{k}_1+...+\mathbf{k}_n-\mathbf{k}\right)$$

From these expansions, we can easily compute summary statistics, such as the marked power spectrum, by using Wick's theorem to evaluate products of $\delta^{(1)}$ fields. Just as for the unmarked case results (see Eq. 2.7.5), we obtain

$$\bar{m}^2M(\mathbf{k}) = \bar{m}^2|\delta_M(\mathbf{k})|^2 \equiv M_{11}(\mathbf{k}) + 2M_{13}(\mathbf{k}) + M_{22}(\mathbf{k}) \tag{3.2.15}$$

$$
\begin{aligned}
M_{11}(\mathbf{k}) &= H_1^2(\mathbf{k}) P_L(k) \\
M_{13}(\mathbf{k}) &= 3 H_1(\mathbf{k}) P_L(k) \int_{\mathbf{p}} H_3(\mathbf{p}, -\mathbf{p}, \mathbf{k}) P_L(p) \\
M_{22}(\mathbf{k}) &= 2 \int_{\mathbf{p}} |H_2(\mathbf{p}, \mathbf{k}-\mathbf{p})|^2 P_L(p) P_L(|\mathbf{k}-\mathbf{p}|)
\end{aligned}
\tag{3.2.16}
$$

where $P_L(k)$ is the linear power spectrum, *i.e.* $\langle \delta^{(1)}(\mathbf{k}) \delta^1(-\mathbf{k}) \rangle$.

The kernels are given by:

$$
\begin{aligned}
H_1(\mathbf{k}) &= C_{\delta_M}(k) Z_1(\mathbf{k}) \\
H_2(\mathbf{k}_1, \mathbf{k}_2) &= C_{\delta_M}(k) Z_2(\mathbf{k}_1, \mathbf{k}_2) + C_{\delta_M^2}(k_1, k_2) Z_1(\mathbf{k}_1) Z_1(\mathbf{k}_2) \\
H_3(\mathbf{k}_1, \mathbf{k}_2, \mathbf{k}_3) &= C_{\delta_M}(k) Z_3(\mathbf{k}_1, \mathbf{k}_2, \mathbf{k}_3) + 2 C_{\delta_M^2}(k_1, k_{23}) Z_1(\mathbf{k}_1) Z_2(\mathbf{k}_2, \mathbf{k}_3) \\
&\qquad + C_{\delta_M^3}(k_1, k_2, k_3) Z_1(\mathbf{k}_1) Z_1(\mathbf{k}_2) Z_1(\mathbf{k}_3),
\end{aligned}
\tag{3.2.17}
$$

where $\mathbf{k} = \sum_i \mathbf{k}_i$, $k_{ij} = |\mathbf{k}_i + \mathbf{k}_j|$, $k = |\mathbf{k}|$, and the H_3 kernel should properly be symmetrized over its arguments. The functions behind Z kernels are defined as:

$$
\begin{aligned}
C_{\delta_M}(k) &= 1 - C_1 W_R(k) \\
C_{\delta_M^2}(k_1, k_2) &= C_2 W_R(k_1) W_R(k_2) - \frac{1}{2} C_1 [W_R(k_1) + W_R(k_2)] \\
C_{\delta_M^3}(k_1, k_2, k_3) &= -C_3 W_R(k_1) W_R(k_2) W_R(k_3) \\
&\qquad + \frac{1}{3} C_2 [W_R(k_2) W_R(k_3) + W_R(k_3) W_R(k_1) + W_R(k_1) W_R(k_2)],
\end{aligned}
\tag{3.2.18}
$$

which are simply the coefficients of an expansion of $\delta_M(\mathbf{k})$ in powers of the full $\delta(\mathbf{k})$ field, *i.e.*;

$$
\bar{m}\, \delta_M(\mathbf{k}) \equiv \sum_{n=1}^{\infty} \int_{\mathbf{k}_1 \ldots \mathbf{k}_n} C_{\delta_M^n}(k_1, ..., k_n) \delta(\mathbf{k}_1) ... \delta(\mathbf{k}_n) \times (2\pi)^3 \delta_D \left(\mathbf{k}_1 + ... + \mathbf{k}_n - \mathbf{k} \right).
\tag{3.2.19}
$$

The linear spectrum M_{11} is simply equal to that of the unmarked field, $P_{11} = Z_1^2(\mathbf{k}) P_L(k)$ damped by the function $C_{\delta_M}^2(k)$. Notably, this damping prefactor appears in *any* H_n term proportional to Z_n, and sources a marked spectrum contribution proportional to $C_{\delta_M}^2(k) P(\mathbf{k})$ for non-linear power spectrum $P(\mathbf{k})$. This has important consequences for evaluation of

the theory: third order contributions to δ appear only in the term proportional to $P(\mathbf{k})$, thus for the remaining terms we can work to second order in δ, *i.e.* considering only Z_1 and Z_2. In this work, we will compute terms proportional to $P(\mathbf{k})$ using the FFTLog algorithm, via the publicly available `CLASS-PT` package (see Appendix Sec. A.3), including the inbuilt infra-red resummation procedure. In a following section, we consider simplifications of the above expressions in order to evaluate them numerically.

The one-loop terms can all be written as even polynomials in μ (the angle cosine between $\mathbf{k}$ and the line-of-sight (LoS) vector $\hat{\mathbf{n}}$). For comparison to data, it is usually more convenient to express the function as a set of Legendre multipoles, $M_\ell(k)$, *i.e.*,

$$M(k,\mu) \equiv \sum_n \tilde{M}_n(k)\mu^{2n} \equiv \sum_\ell M_\ell(k) L_\ell(\mu), \tag{3.2.20}$$

and the even Legendre moments M_ℓ are given in terms of $\tilde{M}_n$ by

$$M_\ell(k) = \sum_n \tilde{M}_n(k) \frac{2\ell+1}{2} \int_{-1}^{1} L_\ell(\mu)\mu^{2n} d\mu$$

where $\{L_\ell(\mu)\}$ are the Legendre polynomials. To compute $M_\ell(k)$, we thus only need expressions for $M(\mathbf{k})$ as an expansion in powers of μ^2.

3.3 Biases, Counterterms and Shot-Noise

To evaluate Eq. (3.2.15), we need to use the Z_n kernels, which require a bias expansion for biased tracers. Following Ref. [40], we employ a third-order expansion:

$$\delta_g(\mathbf{x}) = b_1\delta(\mathbf{x}) + \frac{b_2}{2}\delta^2(\mathbf{x}) + b_{\mathcal{G}_2}[\mathcal{G}_2](\mathbf{x}) + b_{\Gamma_3}[\Gamma_3](\mathbf{x}). \tag{3.3.1}$$

This expansion includes all terms relevant for the one-loop power spectrum. It is worth noting that, unlike the expansion presented in the previous chapter (2.7.1), the term involving R_* is omitted. However, in the final analysis, its effects can be considered as absorbed into the counterterms that will be introduced next. For simplicity, we set b_{Γ_3} to zero, as it was found to be highly degenerate with $b_{\mathcal{G}_2}$ in the BOSS analysis [40], which uses similar volumes to the simulations in this work. This expansion is done in terms of

renormalized operators [20], which, at second order, are related to the usual fields via:

$$[\delta^2](\mathbf{x}) = \delta^2(\mathbf{x}) - \sigma^2, \quad [\mathcal{G}_2](\mathbf{x}) = \mathcal{G}_2(\mathbf{x}). \tag{3.3.2}$$

Here, σ^2 represents the variance of the unsmoothed density field $\delta(\mathbf{x})$, defined as:

$$\sigma^2 = \int_{\mathbf{p}} P_L(p), \tag{3.3.3}$$

which depends on the ultraviolet (UV) cutoff of the theory. By subtracting this term, we ensure that $\langle \delta_g \rangle = 0$ at the loop level. This renormalization step removes the contribution from large-scale fluctuations and guarantees that only the short-scale fluctuations contribute to the power spectrum, keeping the theory physically consistent. So, the new operator $[\delta^2](\mathbf{x})$ is now well-defined and represents only the relevant short-scale fluctuations. For our purposes, we neglect the third-order terms in the bias expansion since they do not contribute any new information to the power spectrum. They only renormalize the well-known terms in $P(k)$, which are already included in the standard models of the power spectrum.
When considering only the unmarked power spectrum, the σ^2 term in $[\delta^2]$ can be neglected, since it gives only a zero-lag contribution (i.e. at $\mathbf{k} = 0$); here, greater caution is needed since the marked theory contains products of operators evaluated at the same location. In Fourier space, its inclusion leads to the redefinition

$$\delta_g(\mathbf{k}) \to \delta_g(\mathbf{k}) - \frac{b_2}{2}\sigma^2(2\pi)^3\delta_D(\mathbf{k}), \tag{3.3.4}$$

Indeed, using the convolution theorem, the Fourier transform of the product $\delta^2(\mathbf{x})$ in real space becomes a convolution in Fourier space:

$$\delta^2(\mathbf{k}) = \int_{\mathbf{p}} \delta(\mathbf{p})\delta(\mathbf{k}-\mathbf{p}), \tag{3.3.5}$$

The expectation value of $\delta^2(\mathbf{k})$ is:

$$\langle \delta^2(\mathbf{k}) \rangle = \int_{\mathbf{p}} \langle \delta(\mathbf{p})\delta(\mathbf{k}-\mathbf{p}) \rangle, \tag{3.3.6}$$

where

$$\langle \delta(\mathbf{p})\delta(\mathbf{k}-\mathbf{p})\rangle = (2\pi)^3\delta_D(\mathbf{k})P_L(p), \tag{3.3.7}$$

and so,

$$\langle \delta^2(\mathbf{k})\rangle = \int_{\mathbf{p}} (2\pi)^3\delta_D(\mathbf{k})P_L(p). \tag{3.3.8}$$

The Dirac delta function $\delta_D(\mathbf{k})$ ensures that this term contributes only at $\mathbf{k}=0$. Thus:

$$\langle \delta^2(\mathbf{k})\rangle = (2\pi)^3\delta_D(\mathbf{k})\int_{\mathbf{p}} P_L(p) = (2\pi)^3\delta_D(\mathbf{k})\sigma^2. \tag{3.3.9}$$

Removing this term ensures that the mean of the density contrast field $\langle\delta_g\rangle = 0$ is preserved. Similarly, for the marked field

$$\begin{aligned}\delta_M^{(2)}(\mathbf{k}) &\to \delta_M^{(2)}(\mathbf{k}) - \frac{b_2}{2}\sigma^2 C_{\delta_M}(k)(2\pi)^3\delta_D(\mathbf{k}),\\ \delta_M^{(3)}(\mathbf{k}) &\to \delta_M^{(3)}(\mathbf{k}) - b_2\sigma^2 C_{\delta_M^2}(k,0)\delta^{(1)}(\mathbf{k}).\end{aligned} \tag{3.3.10}$$

As discussed below, properly including the $\delta_M^{(3)}(\mathbf{k})$ contribution is crucial for the UV-safety of the one-loop $M(\mathbf{k})$ theory.

Now, let's discuss the effects of small-scale physics on the $M(\mathbf{k})$ model. We have seen in Sec. (2.6) that, for unmarked matter at one-loop order, the introduction of a third-order counterterm $\delta^{(ct)}(\mathbf{k}) = -c_s^2k^2\delta^{(1)}(\mathbf{k})$ in the expansion $\delta(\mathbf{k})$, captures the UV-dependence of $P_{13}(\mathbf{k})$, and accounts for the backreaction of short-scale physics on long-wavelength modes. Ref. [35] showed that this c_s^2 counterterm was the only one needed to capture the UV divergences of the one-loop $M(\mathbf{k})$ theory in real-space; equivalently, all other terms are manifestly convergent for hard loop momenta $p \gg k$ due to the presence of smoothing windows that depend on the physical scale R used in the definition of the mark. Given that the expansion of $\delta_M(\mathbf{k})$ includes at most one unsmoothed $\delta(\mathbf{k})$ field, this result holds at arbitrary loop order. Consequently, all potential UV divergences originate solely from terms in $P(\mathbf{k})$, implying that the marked theory does not require any additional counterterms beyond those already present in the unmarked theory.[3]
Moreover, since the terms involving $P(\mathbf{k})$ consistently appear in the combination $\bar{m}^2M(\mathbf{k}) \propto C^2_{\delta_M}(k)P(\mathbf{k})$, the relevant counterterm for $M(\mathbf{k})$ is

[3]This assumes that the smoothing scale R^{-1} is much smaller than the cut-off scale.

$$M_{ct}^{\rm real}(\mathbf{k}) = -2c_s^2 k^2 C_{\delta_M}^2(k) P_L(k) \tag{3.3.11}$$

in real-space, where c_s^2 strictly depends on redshift.

For biased tracers in redshift-space the counterterm structure of $P(\mathbf{k}) \equiv P(k,\mu)$ is somewhat more complex. Here, we follow Ref. [40], and use

$$M_{{\rm ct},\ell}(k) = -2c_\ell^2 k^2 C_{\delta_M}^2(k) P_L(k), \tag{3.3.12}$$

for the multipole counterterms. The reason for keeping two distinct free coefficients is that they account for different loops and capture distinct physical effects. Specifically, the higher-derivative bias primarily affects $\ell = 0$, while the fingers-of-God effect dominates at $\ell = 2$; both effects exhibit a leading-order k^2 scaling. We also include an additional higher-order counterterm

$$M_{\rm ct,NLO}(\mathbf{k}) = \tilde{c}(kfu)^4 \times C_{\delta_M}^2(k) Z_1^2(\mathbf{k}) P_L(k), \tag{3.3.13}$$

where f is the growth rate; this accounts for the next order contribution of FoG.[4] A comprehensive analysis of the ultraviolet (UV) behavior of the unbiased real-space loop integrals is presented in Ref. [35]. For the more general case, it is sufficient to note that the additional divergences take the form:

$$M_{13}(\mathbf{k}) \supset 2C_{\delta_M}(k) C_{\delta_M^2}(k,0) Z_1^2(\mathbf{k}) P_L(k) \int_{\mathbf{p}} \frac{b_2}{2} P_L(p) \tag{3.3.14}$$

$$\begin{aligned} M_{22}(\mathbf{k}) &\supset \frac{b_2^2}{2} C_{\delta_M}^2(k) \int_{\mathbf{p}} P_L(p) P_L(|\mathbf{k}-\mathbf{p}|) \\ &= \frac{b_2^2}{2} C_{\delta_M}^2(k) \int_{\mathbf{p}} \left[P_L(p) P_L(|\mathbf{k}-\mathbf{p}|) - P_L^2(p) \right] \\ &+ \frac{b_2^2}{2} C_{\delta_M}^2(k) \int_{\mathbf{p}} P_L^2(p) \end{aligned} \tag{3.3.15}$$

The divergence in M_{13} is eliminated when the properly renormalized bias operators are included (3.3.10). On the other hand, the second term contains a divergent component in the final line, which is also present in $P(\mathbf{k})$. This

[4] Any FoG kernel is a function of $(k\mu\sigma_v)^2$ for some velocity dispersion σ_v^2; our approach is to take the terms in its Taylor expansion allowing the coefficients to be free; this is more general than assuming some functional form.

divergence can be fully absorbed when considering the stochastic shot noise contribution. Assuming the stochastic part of the power spectrum, which is uncorrelated with the matter field δ, takes the following form:

$$M_{\text{stoch},\ell}(k) = C^2_{\delta_M}(k)\delta^K_{\ell 0} \times P_{\text{shot}}, \tag{3.3.16}$$

where P_{shot} is constant and $\delta^K_{\ell 0}$ is the Kronecker delta, the UV-sensitive component of $M_{22}(\mathbf{k})$ is fully absorbed. Note that assuming a constant P_{shot}, the absence of a contribution for $\ell = 2$ follows from the fact that, in the expansion into multipoles, the integration of $\mathcal{L}_2(\mu)$ over μ results in zero.

One final issue to consider is the effect of infrared (IR) resummation. Following the approximation presented in [35, 36], we replace P_{NL} with its IR-resummed form for terms in the marked spectrum that involve $C^2_{\delta_M} P_{\text{NL}}$. For the remaining terms involving the linear power spectrum $P_L(k)$, we replace it with its IR-resummed counterpart. The specific form of the IR-resummed power spectrum for matter is detailed in Sec. 2.6, and similar expressions apply to biased tracers.
This approximation has been demonstrated to effectively fit simulated data, eliminating any residual wiggles and capturing the expected behavior with appropriate accuracy.

In summary, the one-loop model for the marked spectrum of biased tracers in redshift-space has the following form, expressed in multipoles,

$$\bar{m}^2 M_\ell(k) = M_{11,\ell}(k) + 2M_{13,\ell}(k) + M_{22,\ell}(k) + M_{\text{ct},\ell}(k) + M_{\text{stoch},\ell}(k), \tag{3.3.17}$$

which, assuming $\ell_{\text{max}} = 2$, carries the following seven nuisance parameters;

$$\{b_1, b_2, b_{\mathcal{G}_2}, c_0^2, c_2^2, P_{\text{shot}}, \tilde{c}\}. \tag{3.3.18}$$

In real-space, we do not require c_2^2 or $\tilde{c}$ (and can set $\mu = f = 0$), whilst for unbiased tracers, we can set $b_1 = 1, b_2 = b_{\mathcal{G}_2} = P_{\text{shot}} = 0$.

3.4 Non-local PNG effects

Here, we present the impact of non-local primordial non-Gaussianity (PNG) on the marked power spectrum, extending the results previously derived for the power spectrum and bispectrum (Sec. 2.8). Similar to the other components of the marked power spectrum, the structure of the non-local PNG

contribution mirrors that of the unmarked power spectrum. Specifically, akin to Eq. (2.8.10), an additional term arises from the initial bispectrum contribution:

$$\begin{aligned} f_{\rm NL}M_{12}(\mathbf{k}) &= 2f_{\rm NL}H_1(\mathbf{k})\int_{\mathbf{q}} H_2(\mathbf{k}-\mathbf{q},\mathbf{q})B_{111}(\mathbf{k},\mathbf{q},|\mathbf{k}-\mathbf{q}|) \\ &= 2f_{\rm NL}C_{\delta_M}(k)Z_1(\mathbf{k})\int_{\mathbf{q}}\Big[C_{\delta_M}(k)Z_2(\mathbf{k}-\mathbf{q},\mathbf{q}) \\ &\quad + C_{\delta_M^2}(|\mathbf{k}-\mathbf{q}|,q)Z_1(\mathbf{k}-\mathbf{q})Z_1(\mathbf{q})\Big] \\ &\quad \times B_{111}(\mathbf{k},\mathbf{q},|\mathbf{k}-\mathbf{q}|). \end{aligned} \tag{3.4.1}$$

Additionally, considering the term with the galaxy bias b_ζ, as shown in Eq. (2.8.11), which contributes to the linear marked power spectrum M_{11}, we find:

$$M_g(\mathbf{k}) = M_{g,G}(\mathbf{k}) + f_{\rm NL}\left(M_{12}(\mathbf{k}) + 2b_\zeta Z_1(\mathbf{k})\frac{k^2}{k_{\rm NL}^2}C_{\delta_M}^2(k)\frac{P_L(k)}{\mathcal{T}(k)}\right). \tag{3.4.2}$$

For the marked bispectrum, analogous to the unmarked case in Eq. (2.8.14), we obtain:

$$BM_g(\mathbf{k}_1,\mathbf{k}_2,\mathbf{k}_3) = BM_{g,G}(\mathbf{k}_1,\mathbf{k}_2,\mathbf{k}_3) + H_1(\mathbf{k}_1)H_1(\mathbf{k}_2)H_1(\mathbf{k}_3)f_{\rm NL}B_{111}(k_1,k_2,k_3), \tag{3.4.3}$$

where

$$BM_{g,G}(\mathbf{k}_1,\mathbf{k}_2,\mathbf{k}_3) = 2H_1(\mathbf{k}_1)H_1(\mathbf{k}_2)H_2(\mathbf{k}_1,\mathbf{k}_2)P_L(k_1)P_L(k_2) + 2\,\text{perms.} \tag{3.4.4}$$

It is important to note that, at the power spectrum level, contributions from primordial non-Gaussianity (PNG) appear only at the one-loop order. Furthermore, as demonstrated in [41], the impact of equilateral and orthogonal PNG is highly degenerate with the second-order bias parameters b_2 and $b_{\mathcal{G}_2}$. These two factors significantly reduce the efficiency of power spectrum-only analyses in constraining non-local PNG, thereby making the inclusion of the bispectrum crucial for obtaining meaningful constraints.

The marked power spectrum offers a promising alternative in this regard, as it effectively incorporates higher-order information into a two-point function, as highlighted in [37]. As observed in [38], this may provide an intuitive explanation for the findings of [42], where the marked power spectrum was shown to be significantly more effective in constraining non-local PNG compared to the local type.

3.5 Numerical evaluation in real and redshift space

M_{11} term

Expanding the linear term we get:

$$M_{11}(k,\mu) = C^2_{\delta_M}(k) Z_1^2(\mathbf{k}) P_L(k) = \left[1 - C_1 W_R(k)\right]^2 (b_1 + f\mu_k^2)^2 P_L(k), \quad (3.5.1)$$

And so using the results for the multipole expansion of Z_1^2 [B.0.7] we get:

$$M_{11,\ell}(k) = \left[1 - C_1 W_R(k)\right]^2 P_L(k) \times \begin{cases} b_1^2 + \frac{2}{3} b_1 f + \frac{1}{5} f^2 & \ell = 0 \\ \frac{4}{3} b_1 f + \frac{4}{7} f^2 & \ell = 2 \\ \frac{8}{35} f^2 & \ell = 4 \end{cases} \quad (3.5.2)$$

At this point the numerical implementation is straightforward.

M_{22} term

The M_{22} term is given by:

$$M_{22}(\mathbf{k}) = 2 \int \frac{d^3p}{(2\pi)^3} \left|H_2(\mathbf{p}, \mathbf{k}-\mathbf{p})\right|^2 P_L(p) P_L(|\mathbf{k}-\mathbf{p}|)$$

Given the expansion of $H_2(\mathbf{p}, \mathbf{k}-\mathbf{p})$ in terms of the redshift-space distortion kernels, the expression for $M_{22}(\mathbf{k})$ becomes:

$$M_{22}(\mathbf{k}) = 2 \int \frac{d^3p}{(2\pi)^3} \left| C_{\delta_M}(k) Z_2(\mathbf{p}, \mathbf{k}-\mathbf{p}) + C_{\delta_M^2}(p, |\mathbf{k}-\mathbf{p}|) Z_1(\mathbf{p}) Z_1(\mathbf{k}-\mathbf{p}) \right|^2 \times P_L(p) P_L(|\mathbf{k}-\mathbf{p}|), \quad (3.5.3)$$

We obtain three terms:

$$\begin{aligned} M_{22}^{A}(\mathbf{k}) &= 2\int \frac{d^3p}{(2\pi)^3} C_{\delta_M}^2(k) Z_2^2(\mathbf{p}, \mathbf{k}-\mathbf{p}) P_L(p) P_L(|\mathbf{k}-\mathbf{p}|) \\ &\equiv C_{\delta_M}^2(k) P_{22}(k,\mu) \end{aligned} \tag{3.5.4}$$

This term is just a rescaling of a known term from the unmarked power spectrum.

$$\begin{aligned} M_{22}^{B}(\mathbf{k}) = 4\int \frac{d^3p}{(2\pi)^3} & C_{\delta_M}(k) C_{\delta_M^2}(p, |\mathbf{k}-\mathbf{p}|) \\ & \times Z_2(\mathbf{p}, \mathbf{k}-\mathbf{p}) Z_1(\mathbf{p}) Z_1(\mathbf{k}-\mathbf{p}) \\ & \times P_L(p) P_L(|\mathbf{k}-\mathbf{p}|) \end{aligned} \tag{3.5.5}$$

$$M_{22}^{C}(\mathbf{k}) = 2\int \frac{d^3p}{(2\pi)^3} \left(C_{\delta_M^2}(p, |\mathbf{k}-\mathbf{p}|) Z_1(\mathbf{p}) Z_1(\mathbf{k}-\mathbf{p}) \right)^2 P_L(p) P_L(|\mathbf{k}-\mathbf{p}|) \tag{3.5.6}$$

Computation of $\mathbf{M_{22}^B}$

The second term (3.5.5) can be written as:

$$\frac{M_{22}^{B}(k)}{4 C_{\delta_M}(k)} = C_2 *_{Z_1 Z_1 Z_2} [W_R P_L, W_R P_L](\mathbf{k}) - C_1 *_{Z_1 Z_1 Z_2} [W_R P_L, P_L](\mathbf{k}), \tag{3.5.7}$$

where $*_Z[X,Y]$ is the convolution of X and Y with kernel Z, and $Z_1 Z_1 Z_2 \equiv Z_1(\mathbf{k_1}) Z_1(\mathbf{k_2}) Z_2(\mathbf{k_1}, \mathbf{k_2})$ and we have also used the convolution property $A * B = B * A$ for the C_1 terms.
We have to solve integrals of the form:

$$\mathcal{I}[X,Y] = \int_{\mathbf{p}} Z_1(\mathbf{p}) Z_1(|\mathbf{k}-\mathbf{p}|) Z_2(\mathbf{p}, |\mathbf{k}-\mathbf{p}|) X(p) Y(|\mathbf{k}-\mathbf{p}|) \tag{3.5.8}$$

We can expand the Z_n kernels as polynomials in $\hat{\mathbf{p}} \cdot \hat{\mathbf{n}}$:

$$Z_1(\mathbf{p}) Z_1(\mathbf{k}-\mathbf{p}) Z_2(\mathbf{p}, \mathbf{k}-\mathbf{p}) = \sum_n (\hat{\mathbf{p}} \cdot \hat{\mathbf{n}})^n z_n(k, p, \mu_k, x), \tag{3.5.9}$$

with $x = \hat{\mathbf{p}} \cdot \hat{\mathbf{k}}$.

The integral can be solved using the following result for a rotational scalar function: $S(\mathbf{k}, \mathbf{p}) = S(k, p, x)$:

$$\int_{\mathbf{p}} (\hat{\mathbf{p}}\cdot\hat{\mathbf{n}})^n S(\mathbf{k},\mathbf{p}) = \sum_{m=0}^{n} (\hat{\mathbf{k}}\cdot\hat{\mathbf{n}})^m \int_{\mathbf{p}} G_{nm}(x) S(k,p,x), \tag{3.5.10}$$

where

$$G_{nm}(x) = \sum_{\ell=0}^{n} \left(1+(-1)^{\ell+n}\right)(2\ell+1)\binom{\ell}{m}\binom{\frac{\ell+m-1}{2}}{\ell}\frac{2^\ell n!\left(\frac{n+\ell}{2}+1\right)!}{\left(\frac{n-\ell}{2}\right)!(n+\ell+2)!}L_\ell(x). \tag{3.5.11}$$

For the binomial coefficient appearing in $G_{nm}(x)$, we employ its generalized form using the Gamma function, which allows for an extension to fractional values:

$$\binom{n}{k} = \frac{\Gamma(n+1)}{\Gamma(k+1)\Gamma(n-k+1)}. \tag{3.5.12}$$

Then we get:

$$\mathcal{I}[X,Y] = \sum_n \int_{\mathbf{p}} (\hat{\mathbf{p}}\cdot\hat{\mathbf{n}})^n z_n(k,p,\mu_k,x) X(p) Y\left(\sqrt{k^2+p^2-2kpx}\right) \tag{3.5.13}$$

$$= \sum_n \sum_{m\le n} \mu_k^m \int_0^\infty \frac{p^2 dp}{2\pi^2}\int_{-1}^{1}\frac{dx}{2} z_n(k,p,\mu_k,x) G_{nm}(x) X(p) Y\left(\sqrt{k^2+p^2-2kpx}\right)$$

In the end, we need an expansion of the product of Z_n kernels as polynomials in $(\hat{\mathbf{p}}\cdot\hat{\mathbf{n}})$ and $(\hat{\mathbf{k}}\cdot\hat{\mathbf{n}})$:

$$Z_1(\mathbf{p})Z_1(\mathbf{k}-\mathbf{p})Z_2(\mathbf{p},\mathbf{k}-\mathbf{p}) = \sum_{(n,\alpha)\,\text{pair}} (\hat{\mathbf{p}}\cdot\hat{\mathbf{n}})^n (\hat{\mathbf{k}}\cdot\hat{\mathbf{n}})^\alpha z_{n\alpha}(k,p,x), \tag{3.5.14}$$

Furthermore, to optimize the computation and avoid redundant evaluations—such as when the same integral needs to be computed for different bias parameter values (e.g., for a Fisher matrix analysis or MCMC sampling)—it is beneficial to factor out the bias dependence from the integral. This requires separating the contributions of different bias terms, whether they involve a single bias parameter or products of biases, in the expansion given by Eq. (3.5.14). This decomposition can be efficiently performed using a symbolic computation software like Wolfram Mathematica.

Computation of $\mathbf{M_{22}^C}$

Now, let's consider the third term (3.5.6) of M_{22}. This integral involves $C^2_{\delta^2_M}$ that is given by:

$$C^2_{\delta^2_M}(p, |\mathbf{k}-\mathbf{p}|) = \left[C_2 W_R(p) W_R(|\mathbf{k}-\mathbf{p}|) - \frac{1}{2} C_1 [W_R(p) + W_R(|\mathbf{k}-\mathbf{p}|)]\right]^2 \tag{3.5.15}$$

Expanding this we get:

$$\begin{aligned}
&= C_2^2 W_R^2(p) W_R^2(|\mathbf{k}-\mathbf{p}|) \\
&- C_1 C_2 W_R(p) W_R(|\mathbf{k}-\mathbf{p}|)[W_R(p) + W_R(|\mathbf{k}-\mathbf{p}|)] \\
&+ \frac{C_1^2}{4} W_R^2(p) + \frac{C_1^2}{4} W_R^2(|\mathbf{k}-\mathbf{p}|) + \frac{C_1^2}{2} W_R(p) W_R(|\mathbf{k}-\mathbf{p}|)
\end{aligned}$$

Defining $P_{11} = Z_1^2 P_L$ and considering these terms inside the integral, they can be expressed as convolutions as follows:

$$\begin{aligned}
&\text{1) First term:} \quad C_1^2 * [W_R P_{11}, W_R P_{11}](\mathbf{k}) \\
&\text{2) Second term:} \quad 2C_2^2 * \left[W_R^2 P_{11}, W_R^2 P_{11}\right](\mathbf{k}) \\
&\text{3) Third term:} \quad C_1^2 * \left[W_R^2 P_{11}, P_{11}\right](\mathbf{k}) \\
&\text{4) Fourth term:} \quad -4C_1 C_2 * \left[W_R P_{11}, W_R^2 P_{11}\right](\mathbf{k})
\end{aligned} \tag{3.5.16}$$

where, again, we used the convolution property $A * B = B * A$ for the third term. Thus, the second term of the $M_{22}(\mathbf{k})$ integral is expressed as the sum of these four convolution terms. Convolution in Fourier space coincides with product in real space, in general we can write:

$$* [X, Y](\mathbf{k}) = \mathcal{F}[X(\mathbf{r}) Y(\mathbf{r})](\mathbf{k}) \tag{3.5.17}$$

We have to notice that the convolvands have angular dependence. Efficient evaluation is possible by first expressing X, Y in terms of their multipoles, then computing the multipoles of $[XY](\mathbf{r})$ via the relation

$$[XY]_L(r) = (2L+1) \sum_{\ell,\ell'} X_\ell(r) Y_{\ell'}(r) \begin{pmatrix} \ell & \ell' & L \\ 0 & 0 & 0 \end{pmatrix}^2 \tag{3.5.18}$$

Here, $X_\ell(r)$ and $Y_\ell(r)$ are the radial components corresponding to multipoles ℓ and ℓ' of $X(\mathbf{r})$ and $Y(\mathbf{r})$, respectively. Parentheses represent Wigner 3j

symbols that encode the angular momentum dependence, telling us how to combine two angular mommenta to form a resultant angular momentum L, the constraint is

$$|\ell - \ell'| \leq L \leq \ell + \ell'$$

In our case, the angular dependence is all encoded in Z_1^2 terms so we need its expansion in multipoles (Eq.. B.0.7). So, we have terms like

$$X_\ell(k) = A(k) Z_{1,\ell}^2 \tag{3.5.19}$$

where A(k) involve the linear unmarked power spectrum and can involve window function terms.

Now, to compute the correspondent real space terms we can use the following relation:

$$X_\ell(r) = (-i)^\ell \int \frac{k^2 dk}{2\pi^2} j_\ell(kr) X_\ell(k) \tag{3.5.20}$$

where j_ℓ is the Bessel function of order ℓ.
Then we have to apply the inverse relation which in general is given by

$$X_\ell(k) = 4\pi (i)^\ell \int r^2 dr j_\ell(kr) X_\ell(r) \tag{3.5.21}$$

to the XY product to come back to Fourier space.
To obtain the real-space terms and subsequently transform them back into Fourier space, we use the functions *P2xi* and *xi2P* from the ***mcfit*** library[5].

The Wigner symbols terms that arise for $L = 0$ (monopole), $L = 2$ (quadrupole), and $L = 4$ (hexadecapole) are computed next.

Monopole Term (L = 0)

The non zero Wigner symbols in this case are for:

- $\ell = 0, \ell' = 0$
- $\ell = 2, \ell' = 2$
- $\ell = 4, \ell' = 4$

[5] github.com/eelregit/mcfit

$$\begin{aligned}
&\begin{pmatrix} 0 & 0 & 0 \\ 0 & 0 & 0 \end{pmatrix} = 1 \qquad \begin{pmatrix} 2 & 2 & 0 \\ 0 & 0 & 0 \end{pmatrix} = \sqrt{\frac{1}{5}} \\
&\begin{pmatrix} 4 & 4 & 0 \\ 0 & 0 & 0 \end{pmatrix} = \frac{1}{3}
\end{aligned} \tag{3.5.22}$$

So we obtain:

$$[XY]_{L=0}(r) = X_0(r)Y_0(r) + \frac{1}{5}X_2(r)Y_2(r) + \frac{1}{9}X_4(r)Y_4(r) \tag{3.5.23}$$

Quadrupole Term ($\mathbf{L = 2}$)
For the quadrupole ($L = 2$), we compute the contribution from:

- $\ell = 0, \ell' = 2$ (and viceversa)
- $\ell = 2, \ell' = 2$
- $\ell = 4, \ell' = 2$ (and viceversa)
- $\ell = 4, \ell' = 4$

The correspondent Wigner symbols are:

$$\begin{aligned}
&\begin{pmatrix} 0 & 2 & 2 \\ 0 & 0 & 0 \end{pmatrix} = \sqrt{\frac{1}{5}} \qquad \begin{pmatrix} 2 & 2 & 2 \\ 0 & 0 & 0 \end{pmatrix} = -\sqrt{\frac{2}{35}} \\
&\begin{pmatrix} 4 & 2 & 2 \\ 0 & 0 & 0 \end{pmatrix} = \sqrt{\frac{2}{35}} \qquad \begin{pmatrix} 4 & 4 & 2 \\ 0 & 0 & 0 \end{pmatrix} = -\frac{2}{3}\sqrt{\frac{5}{77}}
\end{aligned} \tag{3.5.24}$$

We obtain:

$$\begin{aligned}
[XY]_{L=2}(r) =& X_0(r)Y_2(r) + X_2(r)Y_0(r) + \frac{2}{7}X_2(r)Y_2(r) \\
&+ \frac{2}{7}X_4(r)Y_2(r) + \frac{2}{7}X_2(r)Y_4(r) + \frac{100}{693}X_4(r)Y_4(r)
\end{aligned} \tag{3.5.25}$$

Hexadecapole Term ($\mathbf{L = 4}$)
For the hexadecapole the contribution arises from:

- $\ell = 2, \ell' = 2$
- $\ell = 4, \ell' = 0$ (and viceversa)

- $\ell = 4, \ell' = 2$ (and viceversa)
- $\ell = 4, \ell' = 4$

So the relevant Wigner symbols are:

$$\begin{aligned} \begin{pmatrix} 2 & 2 & 4 \\ 0 & 0 & 0 \end{pmatrix} &= \sqrt{\frac{2}{35}} \qquad \begin{pmatrix} 4 & 0 & 4 \\ 0 & 0 & 0 \end{pmatrix} = \frac{1}{3} \\ \begin{pmatrix} 4 & 2 & 4 \\ 0 & 0 & 0 \end{pmatrix} &= -\frac{2}{3}\sqrt{\frac{5}{77}} \qquad \begin{pmatrix} 4 & 4 & 4 \\ 0 & 0 & 0 \end{pmatrix} = 3\sqrt{\frac{2}{1001}} \end{aligned} \tag{3.5.26}$$

We obtain:

$$\begin{aligned} [XY]_{L=4}(r) =& \frac{18}{35} X_2(r)Y_2(r) + X_4(r)Y_0(r) + X_0(r)Y_4(r) + \\ & \frac{20}{77} X_4(r)Y_2(r) + \frac{20}{77} X_2(r)Y_4(r) + \frac{162}{1001} X_4(r)Y_4(r) \end{aligned} \tag{3.5.27}$$

M_{13} term

The M_{13} integral is given by

$$\begin{aligned} M_{13}(k,\mu) = 3C_{\delta_M}(k)Z_1(\mathbf{k})P_L(k) \int_{\mathbf{p}} P_L(p) \{ & C_{\delta_M}(k)Z_3(\mathbf{p},-\mathbf{p},\mathbf{k}) \\ & + \frac{2}{3} C_{\delta_M^2}(k,0) Z_1(\mathbf{k}) Z_2(\mathbf{p},-\mathbf{p}) \\ & + \frac{2}{3} C_{\delta_M^2}(p,|\mathbf{k}-\mathbf{p}|) Z_1(\mathbf{p}) Z_2(\mathbf{k},-\mathbf{p}) \\ & + \frac{2}{3} C_{\delta_M^2}(p,|\mathbf{k}+\mathbf{p}|) Z_1(-\mathbf{p}) Z_2(\mathbf{k},\mathbf{p}) \\ & + C_{\delta_M^3}(p,p,k) Z_1(\mathbf{p}) Z_1(-\mathbf{p}) Z_1(\mathbf{k}) \Big\} \end{aligned} \tag{3.5.28}$$

This can be split into three pieces involving C_{δ_M}, $C_{\delta_M^2}$, and $C_{\delta_M^3}$. The first is simply

$$\begin{aligned} M_{13}^A(k,\mu) =& 3C_{\delta_M}^2(k)Z_1(\mathbf{k})P_L(k) \int_{\mathbf{p}} Z_3(\mathbf{p},-\mathbf{p},\mathbf{k})P_L(p) \\ \equiv & C_{\delta_M}^2(k) P_{13}(k,\mu) \end{aligned} \tag{3.5.29}$$

where P_{13} is the unmarked spectrum. Adding this term to M_{22}^A (3.5.4) and M_{11} (3.5.1), we obtain:

$$C_{\delta_M}^2(k)\left(P_{11}(k,\mu)+P_{22}(k,\mu)+P_{13}(k,\mu)\right), \tag{3.5.30}$$

where these terms can be directly taken from CLASS-PT and are simply multiplied by $C_{\delta_M}^2(k)$.

Computation of $\mathbf{M_{13}^B}$

For M_{13}^B we can notice that $Z_2(\mathbf{p},-\mathbf{p})=b_2/2$ so we get:

$$\begin{aligned} M_{13}^B(k,\mu) &= 2C_{\delta_M}(k)C_{\delta_M^2}(k,0)Z_1^2(\mathbf{k})P_L(k)\int_{\mathbf{p}}\frac{b_2}{2}P_L(p) \\ &\quad + 2C_{\delta_M}(k)Z_1(\mathbf{k})P_L(k)\left[\int_{\mathbf{p}} C_{\delta_M^2}(p,|\mathbf{k}-\mathbf{p}|)Z_1(\mathbf{p})Z_2(\mathbf{k},-\mathbf{p})P_L(p)+(\mathbf{p}\leftrightarrow-\mathbf{p})\right] \end{aligned} \tag{3.5.31}$$

The first integral is simply $b_2\sigma^2/2$, which appears UV divergent, but is exactly cancelled by the bias renormalization contribution (see 3.3.10).

Furthermore, we can transform $\mathbf{p}\to-\mathbf{p}$ in the second integral leaving the integral unchanged:

$$M_{13}^B(k,\mu) = 4C_{\delta_M}(k)Z_1(\mathbf{k})P_L(k)\int_{\mathbf{p}} C_{\delta_M^2}(p,|\mathbf{k}-\mathbf{p}|)Z_1(\mathbf{p})Z_2(\mathbf{k},-\mathbf{p})P_L(p) \tag{3.5.32}$$

Now, we adopt the same approach used for M_{22}^B. We expand the Z_n kernels and apply the result for a rotational scalar function (3.5.10), leading to:

$$M_{13}^B(k,\mu) = 4C_{\delta_M}(k)Z_1(\mathbf{k})P_L(k)\sum_n\int_{\mathbf{p}}(\hat{\mathbf{p}}\cdot\hat{\mathbf{n}})^n C_{\delta_M^2}(p,|\mathbf{k}-\mathbf{p}|)z_n(k,p,\mu_k,x)P_L(p) \tag{3.5.33}$$

$$\begin{aligned} &= 4C_{\delta_M}(k)Z_1(\mathbf{k})P_L(k)\sum_n\sum_{m\le n}\mu_k^m\int_0^\infty\frac{p^2dp}{2\pi^2}\int_{-1}^1\frac{dx}{2}C_{\delta_M^2}(p,k,x)z_n(k,p,\mu_k,x) \\ &\qquad\qquad \times G_{nm}(x)P_L(p) \end{aligned}$$

Computation of $\mathbf{M_{13}^C}$

The third term can be written as:

$$M_{13}^C(k,\mu) = 3C_{\delta_M}(k)Z_1^2(\mathbf{k})P_L(k)\int_{\mathbf{p}} C_{\delta_M^3}(p,p,k)Z_1(\mathbf{p})Z_1(-\mathbf{p})P_L(p) \quad (3.5.34)$$

$$= [1 - C_1W_R(k)]\,(b_1 + f\mu^2)^2P_L(k)$$

$$\times \left(b_1^2 + \frac{2b_1f}{3} + \frac{f^2}{5}\right)\int_{\mathbf{p}} \left[2C_2W_R(k)W_R(p) + (C_2 - 3C_3W_R(k))\,W_R^2(p)\right]P_L(p),$$

Note that $Z_1(\mathbf{p})$ is equivalent to $Z_1(-\mathbf{p})$ because $\mu_p^2 = \mu_{-p}^2$. The factor $\left(b_1^2 + \frac{2b_1f}{3} + \frac{f^2}{5}\right)$ results from the angular integration of $Z_1^2(\mathbf{p})$, corresponding to the Kaiser monopole prefactor. To be precise from the angular integration results also a factor of '2' but it is used to restore the full 3D integral over $\mathbf{p}$, indeed the integrand no longer depends on μ_p, so the factor of 2 is represented by the angular integral $\int_{-1}^{1} d\mu_p$. Now we define:

$$S_R = \left(b_1^2 + \frac{2b_1f}{3} + \frac{f^2}{5}\right)\int_{\mathbf{p}} W_R(p)P_L(p), \quad (3.5.35)$$

and analogously for S_{RR}:

$$S_{RR} = \left(b_1^2 + \frac{2b_1f}{3} + \frac{f^2}{5}\right)\int_{\mathbf{p}} W_R^2(p)P_L(p), \quad (3.5.36)$$

The integrals are defined as variances σ_R^2 and σ_{RR}^2, the angular part can be easily solved analytically while the radial integral can be solved numerically:

$$\sigma_R^2 = \frac{1}{(2\pi)^3}\int_0^\infty p^2dp\int_{-1}^{1} d\mu\int_0^{2\pi} d\phi\, W_R(p)P_L(p)$$

Since $W_R(p)$ and $P_L(p)$ depend only on the magnitude p, the angular integrals contribute a factor of 4π, leading to:

$$\sigma_R^2 = \frac{1}{2\pi^2}\int_0^\infty p^2W_R(p)P_L(p)dp,$$

which can be efficiently computed using a standard one-dimensional integration method.

Analogously we can solve σ_{RR}^2, the only difference is due to the presence of the square Gaussian window function. In the end M_{13}^C can be written as:

$$\begin{aligned} M_{13}^C(k,\mu) = &[1 - C_1W_R(k)]\,(b_1 + f\mu^2)^2P_L(k) \\ &\times [2C_2W_R(k)S_R + (C_2 - 3C_3W_R(k))\,S_{RR}] \end{aligned} \quad (3.5.37)$$

PNG term

The computation of the PNG contribution in Eq. (3.4.2) is divided into two parts: the calculation of M_{12} and the term proportional to b_ζ. The latter is given by:

$$2f_{\rm NL}b_\zeta Z_1(\mathbf{k})\frac{k^2}{k_{\rm NL}^2}C^2_{\delta_M}(k)\frac{P_L(k)}{\mathcal{T}(k)}, \tag{3.5.38}$$

which can be computed straightforwardly.

The first term, M_{12}, is given by Eq. (3.4.1):

$$\begin{aligned} f_{\rm NL}M_{12}(\mathbf{k}) = 2f_{\rm NL}C_{\delta_M}(k)Z_1(\mathbf{k})\int_{\mathbf{q}}\Big[&C_{\delta_M}(k)Z_2(\mathbf{k}-\mathbf{q},\mathbf{q}) \\ &+ C_{\delta^2_M}(|\mathbf{k}-\mathbf{q}|,q)Z_1(\mathbf{k}-\mathbf{q})Z_1(\mathbf{q})\Big] \\ &\times B_{111}(\mathbf{k},\mathbf{q},|\mathbf{k}-\mathbf{q}|). \end{aligned}$$

This expression can be decomposed into two separate integrals: one involving the Z_2 kernel and another involving products of Z_1 kernels:

$$f_{\rm NL}M^A_{12}(\mathbf{k}) = 2f_{\rm NL}C_{\delta_M}(k)Z_1(\mathbf{k})\int_{\mathbf{q}}C_{\delta_M}(k)Z_2(\mathbf{k}-\mathbf{q},\mathbf{q})B_{111}(\mathbf{k},\mathbf{q},|\mathbf{k}-\mathbf{q}|), \tag{3.5.39}$$

$$\begin{aligned} f_{\rm NL}M^B_{12}(\mathbf{k}) = 2f_{\rm NL}C_{\delta_M}(k)Z_1(\mathbf{k})\int_{\mathbf{q}}&C_{\delta^2_M}(|\mathbf{k}-\mathbf{q}|,q)Z_1(\mathbf{k}-\mathbf{q})Z_1(\mathbf{q}) \\ &\times B_{111}(\mathbf{k},\mathbf{q},|\mathbf{k}-\mathbf{q}|) \end{aligned} \tag{3.5.40}$$

Considering the expression of the Z_2 kernel in Eq. (2.7.7), the quantity M^A_{12} can be efficiently decomposed into contributions from different bias terms. All terms, except for the last term in Z_2—the one proportional to $\frac{f\mu_\mathbf{k}k}{2}$—can be evaluated using a standard two-dimensional numerical integration method.

The remaining term can be computed using the same approach applied to M^B_{13} and M^A_{22}. Similarly, the second integral, which involves Z_1 kernels, can be evaluated following the method used for M^B_{13} and M^B_{22}.

Results and implementation details

We now present the results obtained from the numerical implementation described above. The following plots correspond to the calculations performed

at $z = 1$.
Figure 3.2 shows the components of the marked power spectrum for matter in both real and redshift space at one-loop order. In redshift space, the counterterm M_{ct} also includes the next-to-leading order (NLO) contribution, as given in Eq. (3.3.13).
Similarly, Figure 3.3 presents the marked power spectrum for galaxies. The bias parameters used in this case are $b_1 = 1.30$, $b_2 = -0.73$, and $b_{\mathcal{G}_2} = -0.086$, following a semi-analytic model that depends on the redshift z, which will be introduced in the next chapter.

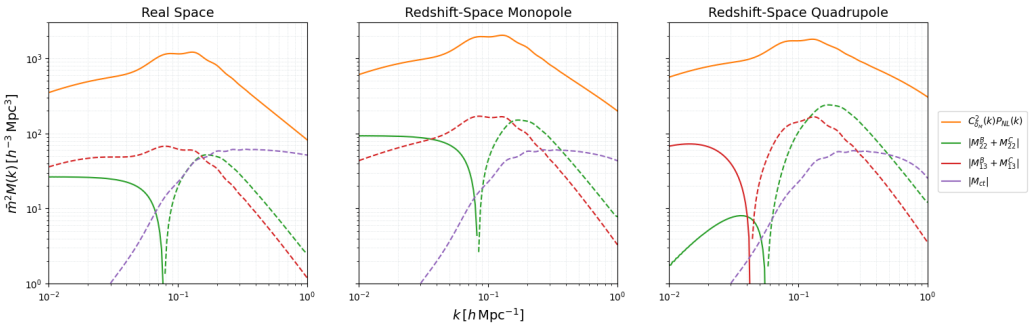

Figure 3.2: Marked power spectrum components for matter in real and redshift space at $z = 1$, computed at one-loop order. The mark parameters are $p = 1$, $\delta_s = 0.25$, and $R = 15\,\mathrm{h}^{-1}$Mpc. The first term, $C^2_{\delta_M} P_{NL}(k)$, includes both the linear term M_{11} and the contributions to M_{22} and M_{13} that are proportional to their unmarked counterparts. Note that the additional contributions to the '22' and '13' terms become significant in the $k \to 0$ limit. The counterterm parameter is set to $c_s^2 = 1$. The dashed lines indicate negative contributions.

We proceed with the presentation of the marked PNG contribution results. Fig. 3.4 shows the contributions for the matter case, while Fig. 3.5 displays the corresponding results for galaxies. For these computations, we use the same bias parameter values as in Fig. 3.3 and set $f_{NL}^{\mathrm{equil}} = f_{NL}^{\mathrm{ortho}} = 1$.

The following provides details on the structure of the codes used to compute the various contributions to the marked power spectrum.
The values of the linear power spectrum, P_L, are obtained from CLASS-PT[43, 18]. To facilitate their use in numerical integrations, a continuous function is constructed via interpolation. It is important to ensure that the

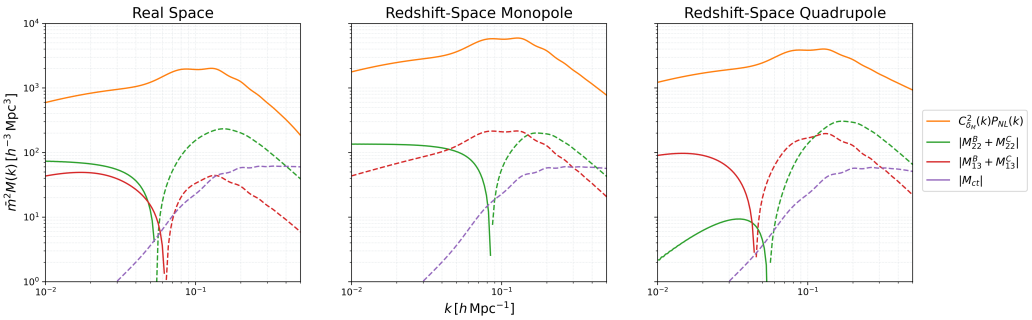

Figure 3.3: Marked power spectrum components for galaxies, analogous to Fig. 3.2. The bias parameters used are $b_1 = 1.30$, $b_2 = -0.73$, and $b_{\mathcal{G}_2} = -0.086$. The counterterms parameters are set to $c_\ell^2 = \tilde{c} = 1$.

interpolation covers a sufficiently wide range of k values. This prevents cases where the argument of the interpolated power spectrum function extends beyond its defined range, which could otherwise lead to inaccuracies in the computations.

For the computation of M_{13}^B, M_{22}^B, and for some terms of M_{12} (as discussed in Sect. 3.5), special attention is required.
First, we describe the structure of the code used for the computation of M_{13}^B, which is the same approach applied to the previously mentioned terms of M_{12}.
The first step involves determining the relevant components of the perturbative kernels based on the choice of bias model, i.e., whether we are computing results for matter or galaxies. These components are selected according to the powers of μ_p and μ_k, noting that we must also consider the additional contribution arising from μ_k^m after applying the result for the integration of a rotational scalar function (Eq. 3.5.10).
Once the relevant terms have been identified, they are used to construct the full integrand. At this stage, the proper weighting factors must be applied, depending on whether the monopole ($\ell = 0$) or quadrupole ($\ell = 2$) contribution is being computed. These weights ensure the correct angular averaging over μ_k, which affects the final result.
Additionally, since our goal is to isolate the dependence on bias parameters, the integration process must be structured accordingly. Specifically, rather than computing a single integral, it is necessary to evaluate multiple integrals separately, each corresponding to different bias terms or products of bias pa-

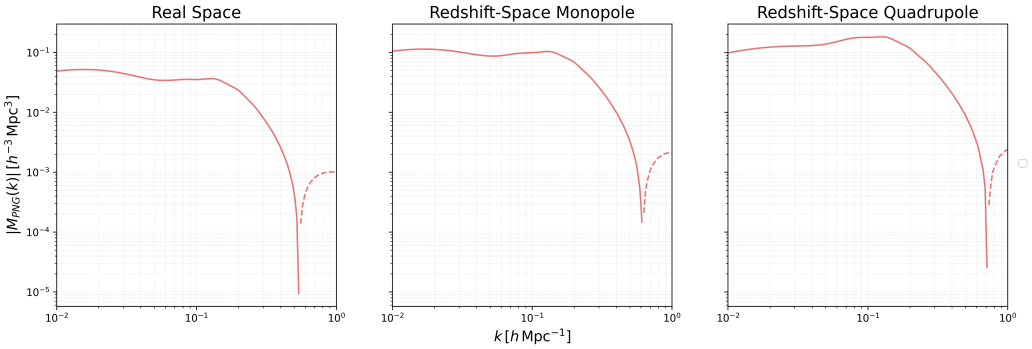

Figure 3.4: Contribution of non-local PNG to the marked power spectrum for matter. Here, we set $f_{NL}^{\mathrm{equil}} = f_{NL}^{\mathrm{ortho}} = 1$ for simplicity. Also in this case, the contribution is more significant in the $k \to 0$ limit. Dashed lines indicate negative contributions.

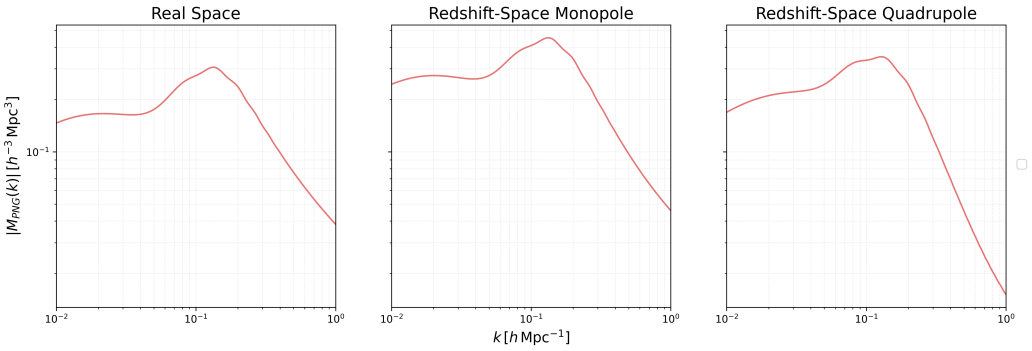

Figure 3.5: Marked PNG contribution for galaxies, analogous to Figure 3.4.

rameters arising from the expansion of the Z_n kernels. The final result is then obtained by adding these contributions to reconstruct the total value of the integral.

A crucial aspect of this approach is the presence of the $Z_1(k)$ kernel, which, in principle, is outside the integral and is not included in the expansion of the other Z_n kernels. However, it plays an essential role in selecting the correct angular averaging factor. As a consequence, when constructing the integrand, we obtain separate contributions for terms proportional to b_1 and f. This allows us to compute the integral for both contributions independently. By doing so, we fully separate the dependence on bias parameters

from the numerical integration process, enabling us to compute the integral for each bias term separately and then multiply the resulting value by the appropriate bias factor.
After constructing the integrand, numerical integration is performed over the variables x and p. This requires summing over all valid kernel components, each contributing according to its respective order in the perturbative expansion. The integration is carried out using established numerical methods, ensuring sufficient accuracy in capturing the relevant contributions.
The final step in the computation involves applying the necessary weighting factors associated with the different bias parameters. Since the integral has been structured to separate contributions from different bias terms, these factors can be applied independently before summing the results. This modular approach ensures flexibility, allowing modifications to the kernel expansion or integration method without affecting the overall framework.

To summarize, the calculation proceeds as follows:

1. The relevant perturbative kernel components are identified based on the bias model.

2. The full integrand is constructed, incorporating the appropriate averaging factors for monopole or quadrupole contributions.

3. The integral is computed separately for contributions proportional to b_1 and f, leveraging the presence of $Z_1(k)$ to isolate these terms.

4. Numerical integration is performed over x and p, summing over the contributions from different terms.

5. The final result is obtained by applying the correct bias weighting and summing the individual contributions.

This structured approach ensures that the computation remains efficient and adaptable.

For M_{22}, the structure is similar but simplified since there is no $Z_1(\mathbf{k})$ outside the integral. This allows us to avoid computing the contributions from the b_1 and f terms separately, thus simplifying the selection of the correct angular averaging factor. In contrast to the previous case, where the presence of $Z_1(\mathbf{k})$ required isolating the dependence on b_1 and f before performing the integral, here the entire dependence on bias parameters is already included within the integral formulation. As a result, we can compute the integral

directly for each bias term without needing an intermediate separation step. Based on the implementation described above, the integration process is optimized by precomputing common terms and leveraging parallel computation to efficiently evaluate contributions from different bias terms.

The expansion of the product of Z kernels involved in the above description is given in Appendix B.

Chapter 4

Results: Model Fitting and Fisher Forecast

In this chapter, we delve into some key statistical concepts and apply the Fisher matrix formalism to derive constraints on cosmological and bias parameters using the marked power spectrum. We also compare these results with those obtained using the unmarked power spectrum.

As discussed in the previous chapters, particularly in Chapter 2, the current understanding of the large-scale structure of the universe posits that the observed matter distribution on cosmological scales originates from the growth of primordial small seed fluctuations in a homogeneous universe, amplified by gravitational instability. Testing cosmological theories, which help characterize these primordial seeds, inherently involves statistical methods for the following reasons: first, we lack direct observational access to the primordial fluctuations, leaving us without well-defined initial conditions; second, the timescale of cosmological evolution is vastly greater than the observational timescale, making it impossible to track the evolution of individual systems. As a result, studying the evolution of structures needs a statistical approach. The present universe is thus modeled as a stochastic realization of a statistical ensemble of possibilities. Consequently, the goal is to predict statistical realizations that depend on the statistical properties of the primordial perturbations responsible for the current configuration of the large-scale structure.

Before presenting results on cosmological and bias parameter constraints, we first validate our theoretical predictions and numerical pipeline against N-body simulations. This validation step is crucial to ensure the robustness

of the Fisher forecasts discussed later in this chapter.

4.1 Code validation

Before moving on to the Fisher forecast analysis, we begin by validating our numerical implementation of the model against the results from the QUIJOTE [44] and QUIJOTE-PNG [45] simulation suites. These are dark matter-only N-body simulations with volumes of 1 $h^{-1}\text{Gpc}^3$ and 512^3 particles per box, run using the TreePM code GADGET-III. The initial conditions were generated at redshift $z = 127$ using 2LPTIC [46] for the standard simulations, and 2LPTPNG [45, 47] for those including primordial non-Gaussianity (PNG). Our analysis focuses on dark matter halos, identified using the Friends-of-Friends algorithm [48] with a linking length of $b = 0.2$, considering only halos containing more than 20 particles. The cosmological parameters are fixed to their fiducial values: $\{\sigma_8, n_s, \Omega_b, \Omega_m, h\} = \{0.834, 0.9624, 0.049, 0.3175, 0.6711\}$. We test our perturbation theory (PT) model and numerical implementation at redshifts $z = \{0, 0.5, 1\}$ using the mark parameters $\{p = 1, R = 15\ h^{-1}\text{Mpc}, \delta_s = 0.25\}$. Keeping the cosmology fixed, we fit the bias, small-scale, and stochastic parameters $\{b_1, b_2, b_{G_2}, c_s^2, P_{\text{shot}}\}$ to the measured marked power spectrum from the simulations.

The results of this fit are shown in Figure 4.1, where we plot the mean marked power spectrum obtained from the PNG simulations, fitted up to $k_{\text{max}} = 0.30\ h/\text{Mpc}$. We show results for three scenarios: without PNG, and with both positive and negative values of $f_{\text{NL}}^{\text{equil}}$.

To assess the accuracy of our model, we estimate the data covariance from the scatter across different realizations of the simulations with fixed cosmology. The model's theoretical prediction reproduces the simulation results with high accuracy—typically within 1%—up to k_{max}, across all redshifts considered.

Since the redshift-space version of the model relies on the same core implementation as the real-space case tested here, this provides a strong validation of our framework.

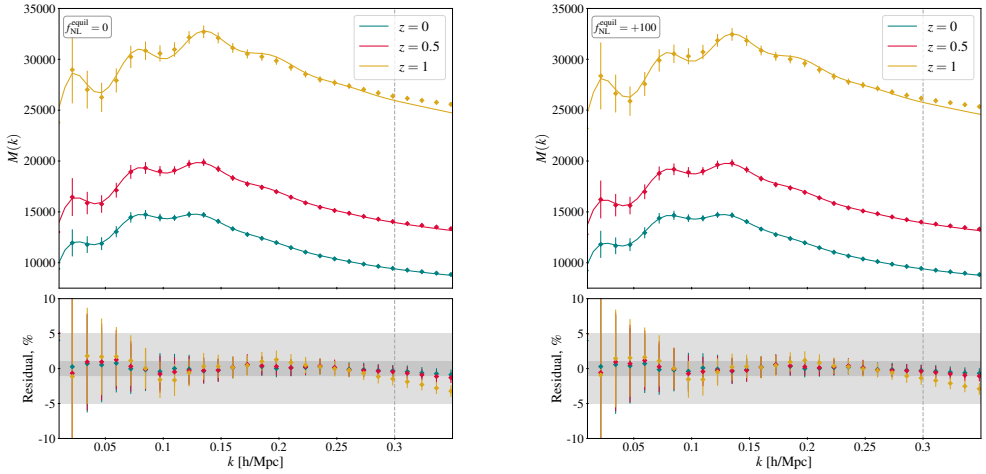

Figure 4.1: Results of the fitting of the marked power spectrum from the QUIJOTE simulations, shown without PNG (left panel) and with $f_{\rm NL}^{\rm equil} = 100$ (right panel), across different redshifts. The vertical dashed grey line indicates the value of $k_{\rm max}$ up to which the fit is performed. The diamond markers represent the mean marked power spectrum measured from the simulations, while the solid lines correspond to the results obtained from the theoretical model fit.

4.2 Parameter estimation

Following the approach outlined in [49], we begin by reviewing fundamental concepts frequently encountered in cosmological data analysis. Many of these problems fall under the category of "inverse problems," where we are given a dataset, denoted as $\mathbf{x}$, and seek to derive meaningful interpretations from it. One illustrative example is assessing whether large-scale structure observations support the hypothesis that the universe is spatially flat.

In cosmology, our primary task is to analyze collected data and interpret it within the framework of a theoretical model. This model is assumed to be valid and typically includes a set of parameters, represented as $\boldsymbol{\theta}$, which we aim to determine. This process is known as parameter estimation. The ultimate objective is to estimate these parameters along with their associated uncertainties, or ideally, to obtain the full probability distribution of $\boldsymbol{\theta}$

given the observed data $\mathbf{x}$. This distribution is referred to as the *posterior probability* and is expressed as:

$$p(\boldsymbol{\theta}|\mathbf{x}). \tag{4.2.1}$$

From this posterior distribution, one can compute both the expectation values of the parameters and their corresponding uncertainties.

Forward modeling

Instead of directly computing the posterior probability, it is often more practical to evaluate its counterpart:

$$p(\mathbf{x}|\boldsymbol{\theta}), \tag{4.2.2}$$

which is known as forward modeling. In this approach, given a set of known parameters, we determine the expected distribution of the data. Typical forward modeling distributions include commonly used ones such as Binomial, Poisson, and Gaussian distributions, as well as more intricate cases, like predictions for the large-scale structure (LSS) power spectrum based on cosmological parameters.
As an illustrative example, consider a model where the data follows a Gaussian distribution with mean μ and variance σ^2. This model is characterized by the parameters $\boldsymbol{\theta} = (\mu, \sigma)$. Given these parameters, the probability of a single data point x is expressed as:

$$p(x|\boldsymbol{\theta}) = \frac{1}{\sqrt{2\pi}\sigma} e^{-\frac{(x-\mu)^2}{2\sigma^2}}. \tag{4.2.3}$$

A key aspect of statistical inference is the connection between Eq. (4.2.3) and the posterior probability $p(\boldsymbol{\theta}|\mathbf{x})$, which is established via Bayes' theorem:

$$p(\boldsymbol{\theta}|\mathbf{x}) = \frac{p(\mathbf{x}|\boldsymbol{\theta})p(\boldsymbol{\theta})}{p(\mathbf{x})}. \tag{4.2.4}$$

Here, $p(\mathbf{x}|\boldsymbol{\theta})$ is referred to as the *likelihood*, often denoted as $L(\mathbf{x}, \boldsymbol{\theta})$. The term $p(\boldsymbol{\theta})$ represents the *prior*, encapsulating prior knowledge about the parameters before observing the data. This prior information may originate

from previous experiments or theoretical considerations. The denominator $p(\mathbf{x})$, known as the *evidence*, is given by:

$$p(\mathbf{x}) = \int d\boldsymbol{\theta}\, p(\mathbf{x}|\boldsymbol{\theta}) p(\boldsymbol{\theta}). \tag{4.2.5}$$

In scenarios where no prior information is available, it is common to invoke the principle of indifference, assuming a flat prior where all parameter values are equally likely. Under this assumption, setting $p(\boldsymbol{\theta}) = \text{const.}$, the posterior probability simplifies to:

$$p(\boldsymbol{\theta}|\mathbf{x}) \propto L(\mathbf{x};\boldsymbol{\theta}). \tag{4.2.6}$$

Errors

Now, let us assume we have a posterior probability distribution $p(\boldsymbol{\theta}|\mathbf{x})$. One common estimator of the parameters, which we indicate with the hat symbol, is the mean:

$$\hat{\boldsymbol{\theta}} = \int d\boldsymbol{\theta}\, p(\boldsymbol{\theta}|\mathbf{x})\boldsymbol{\theta}. \tag{4.2.7}$$

We define an estimator *unbiased* if its expectation value coincides with the true value of the parameter, $\boldsymbol{\theta}_0$:

$$\langle \hat{\boldsymbol{\theta}} \rangle = \boldsymbol{\theta}_0. \tag{4.2.8}$$

Now, for simplicity, we assume that the probability distribution is single-peaked. Moreover, we assume a flat prior, so that the posterior probability is proportional to the likelihood. We can therefore study the behavior of $L(\mathbf{x}|\boldsymbol{\theta})$ close to the peak, performing a Taylor expansion of the logarithm of the likelihood function:

$$\log L(\mathbf{x};\boldsymbol{\theta}) = \log L(\mathbf{x};\boldsymbol{\theta}_0) + \frac{1}{2}(\boldsymbol{\theta_\alpha} - \boldsymbol{\theta_{0\alpha}}) \frac{\partial^2 \ln L}{\partial \boldsymbol{\theta_\alpha} \partial \boldsymbol{\theta_\beta}} (\boldsymbol{\theta_\beta} - \boldsymbol{\theta_{0\beta}}) + \cdots, \tag{4.2.9}$$

which implies that, locally, $L(\mathbf{x};\boldsymbol{\theta})$ is a multivariate Gaussian in the parameter space:

$$L(\mathbf{x};\boldsymbol{\theta}) = L(\mathbf{x};\boldsymbol{\theta}_0) e^{-\frac{1}{2}(\boldsymbol{\theta_\alpha} - \boldsymbol{\theta_{0\alpha}}) H_{\alpha\beta} (\boldsymbol{\theta_\beta} - \boldsymbol{\theta_{0\beta}})}, \tag{4.2.10}$$

where we have used

$$H_{\alpha\beta} = -\frac{\partial^2 \ln L}{\partial \boldsymbol{\theta_\alpha} \partial \boldsymbol{\theta_\beta}}, \tag{4.2.11}$$

which is called the Hessian matrix. The Hessian indicates whether the estimates of θ_α and θ_β are correlated or not. In fact, if $H_{\alpha\beta}$ is not diagonal, it means that the estimates are correlated. Let us note that, even if the quantities themselves are uncorrelated, their estimates could have a similar effect on the data; in this case, the estimates would be actually correlated, therefore leading to a non-diagonal Hessian.

4.3 Fisher matrix formalism

In this section, we address an essential question: to what degree of precision can we estimate model parameters given a specific dataset? The precision, represented by the error bars associated with the measurement of cosmological parameters, can be effectively determined using the Fisher information matrix formalism.
Following a similar approach as in Sec. 4.2, we consider the dataset as an N-dimensional vector $\mathbf{x}$, where each component x_i could correspond, for instance, to the variations in galaxy density relative to the mean, across N independent bins covering the three-dimensional survey volume. This vector $\mathbf{x}$ is treated as a random variable, with an associated probability distribution function $L(\mathbf{x}, \boldsymbol{\theta})$ (the likelihood), which depends on a set of cosmological parameters $\boldsymbol{\theta}$. Our objective is to estimate these parameters.
To achieve this, we require the explicit formulation of the Fisher matrix, which is defined as the expectation value of the Hessian, as given by Eq. (4.2.11):

$$F_{ij} \equiv -\left\langle \frac{\partial^2 \ln L}{\partial\theta_i \partial\theta_j} \right\rangle . \tag{4.3.1}$$

The Cramer-Rao Bound

A particularly useful feature of this method is that the inverse of the Fisher matrix, $\mathbf{F}^{-1}$, serves as an optimal covariance matrix for the measurement uncertainties of the parameters. This leads to the fundamental inequality:

$$\Delta\theta_i \Delta\theta_j \geq (\mathbf{F}^{-1})_{ij}. \tag{4.3.2}$$

As a consequence, if all parameters—including the one of primary interest—are estimated from the data, then:

$$\Delta\theta_i \geq (\mathbf{F}^{-1})_{ii}^{1/2}. \tag{4.3.3}$$

However, in cases where all other parameters are held fixed, the uncertainty is given by:

$$\Delta\theta_i \geq \frac{1}{\sqrt{F_{ii}}}. \tag{4.3.4}$$

This expression is known as the Cramer-Rao inequality, which provides a fundamental lower bound on the variance of an unbiased estimator.

Constraints on Non-Local PNG

Here, we build upon the analysis presented in [38], extending the results to redshift space. To constrain non-local primordial non-Gaussianities, we will conduct a Fisher forecast up to mildly non-linear scales. In this analysis, we compute the marked power spectrum for two distinct cases: one using $p = 2$ to enhance underdense regions and another using $p = -1$ to highlight overdense ones.
We fix the fiducial values of the galaxy bias parameters using a semi-analytic model of galaxy formation. Although this model was originally developed for Euclid-like Hα galaxies [43], we also apply it to BOSS-like survey volumes. This choice is justified because our analysis focuses on the relative differences between statistics, rather than their absolute values:

$$b_1(z) = 0.9 + 0.4z\,. \tag{4.3.5}$$

For the higher order biases we adopt the following fitting formulae, obtained from a combination of N-body simulations and halo occupation modeling [19, 50]:

$$b_2(z) = -0.704 - 0.208z + 0.183z^2 - 0.00771z^3\,. \tag{4.3.6}$$

For $b_{\mathcal{G}_2}$ and b_{Γ_3} we use instead the co-evolution model [19, 51], which gives

$$b_{\mathcal{G}_2}(z) = -\frac{2}{7}\left(b_1(z) - 1\right), \quad b_{\Gamma_3}(z) = \frac{23}{42}\left(b_1(z) - 1\right). \tag{4.3.7}$$

For the higher-derivative term, we set $c_s^2 = 1$ [Mpc/h]^2, as it is expected to be of order unity in the context of the EFT of Large-Scale Structure.

z	b_1	b_2	$b_{\mathcal{G}_2}$	b_{Γ_3}	c_s^2 $[\mathrm{Mpc}/h]^2$	$P_{\rm shot}$ $[\mathrm{Mpc}/h]^3$
0.61	1.14	-0.38	-0.041	0.079	1	3333

Table 4.1: Table of fiducial values for the redshift, bias parameters, counterterm and shot-noise parameters adopted for the forecast.

For the PNG bias b_ζ, we adopt the universality relation introduced in Sec. 2.8, which we report here for completeness:

$$b_\zeta = \frac{18}{5}\delta_c(b_1 - 1) \tag{4.3.8}$$

Finally, the fiducial values for the stochastic terms are set to the Poisson sampling prediction

$$P_{\rm shot} = \bar{n}_g^{-1}. \tag{4.3.9}$$

We perform a forecast for BOSS CMASS2 redshift $z = 0.61$ and total volume $V_{\rm BOSS} = 3.83\,(\mathrm{Gpc/h})^3$, with number density $\bar{n}_g^{\rm BOSS} = 3{\times}10^{-4}\,(\mathrm{h/Mpc})^3$. The list of fiducial bias parameters is listed in Tab. 4.1.

Moreover, we vary the cosmological parameters, using their fiducial values as listed in Table 4.2.

A_s	n_s	ω_{cdm}	h	$f_{\rm NL}^{\rm equil}$	$f_{\rm NL}^{\rm ortho}$
2.089 10^{-9}	0.9624	0.2685 h^2	0.6711	0	0

Table 4.2: Table of fiducial values of the cosmological parameters varied in the forecast. These values correspond to the fiducial cosmology of the *Quijote* simulations. The value of $\omega_{\rm cdm}$ follows from $\Omega_b = 0.049$ and $\Omega_m = 0.3175$.

We consider diagonal Gaussian covariances, since, as noted in [38], this approximation accurately reproduces the results obtained from the Quijote simulations. Following [52], we have computed the explicit expressions for the redshift-space case, obtaining:

$$C_{P_0P_0} = \frac{2(2\pi)^3}{VV_s}\left(P_0^2(k) + \frac{1}{5}P_2^2(k)\right), \tag{4.3.10}$$

$$C_{P_0P_2} = \frac{2(2\pi)^3}{VV_s}\left(\frac{2}{7}P_2^2(k) + 2P_0(k)P_2(k)\right), \tag{4.3.11}$$

$$C_{P_2P_2} = \frac{2(2\pi)^3}{VV_s}\left(5P_0^2(k) + \frac{15}{7}P_2^2(k) + \frac{20}{7}P_0(k)P_2(k)\right). \tag{4.3.12}$$

The same expressions hold for the marked power spectrum by replacing the power spectrum with the marked power spectrum.

For the cross-covariances between the marked and unmarked power spectra, we obtain:

$$C_{P_0M_0} = \frac{(2\pi)^3}{VV_s}\left(P_0(k)M_0(k) + \frac{1}{5}P_2(k)M_2(k)\right), \tag{4.3.13}$$

$$C_{P_0M_2} = \frac{(2\pi)^3}{VV_s}\left(\frac{2}{7}P_2(k)M_2(k) + P_0(k)M_2(k) + P_2(k)M_0(k)\right), \tag{4.3.14}$$

$$C_{P_2M_2} = \frac{(2\pi)^3}{VV_s}\left(5P_0M_0(k) + \frac{15}{7}P_2(k)M_2(k) + \frac{10}{7}P_0(k)M_2(k) + \frac{10}{7}P_0(k)M_2(k)\right). \tag{4.3.15}$$

The results of our analysis for $f_{\rm NL}^{\rm equil}$ and $f_{\rm NL}^{\rm ortho}$ are shown in Fig. 4.2, while the plots for all the parameters involved in the analysis can be found in Appendix C.

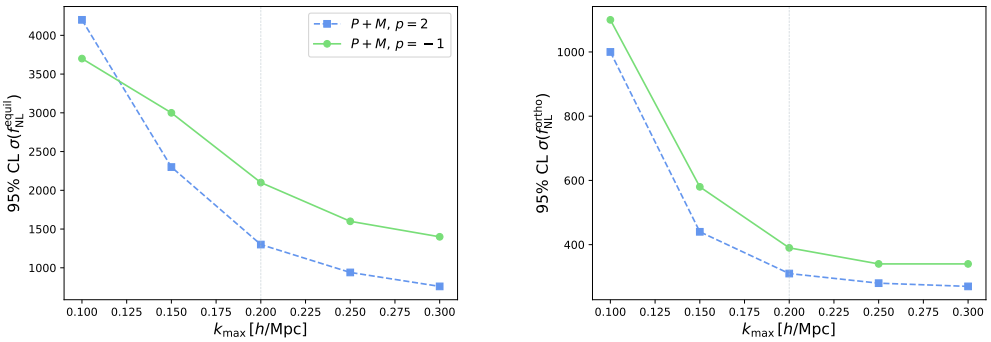

Figure 4.2: 2σ constraints from galaxies for cosmologies with Non-Local PNG and BOSS CMASS volume, number density and redshift described in the main text. The dashed vertical line represent the maximum wavevector adopted in standard analysis [40].

To understand the trend shown in Fig. 4.2, where tighter constraints on $f_{\rm NL}^{\rm equil}$ are obtained for positive values of p, we recall that—as noted in the real-space analyses of [38, 53]—the signal from equilateral PNG is enhanced in the presence of non-linear filamentary structures.

These structures form as the Universe evolves, when small initial density fluctuations grow under gravity and turn into a network of filaments and voids. Equilateral PNG, which couples modes of similar size (i.e., $k_1 \approx k_2 \approx k_3$), tends to boost small-scale fluctuations. This coupling causes the density to vary more rapidly over short distances, creating sharp features in the matter distribution. A positive bispectrum increases the contrast in overdense regions, while a negative one does the same in underdense areas. Over time, these early fluctuations grow into the complex structure we observe today — with filaments and void edges being the regions where the impact of equilateral PNG is most visible.
In this context, choosing a positive value of the density-weighting parameter p enhances the contribution from underdense environments, such as void boundaries and filamentary regions, where the signal from equilateral PNG is most prominent. This makes $p > 0$ an effective choice for improving sensitivity to this class of primordial non-Gaussianity.
The results of the forecast at 95% CL at $k_{\rm max} = 0.30$ are:

$$\sigma^{\rm equil}_{p=-1} = 1400, \quad \sigma^{\rm ortho}_{p=-1} = 340 \tag{4.3.16}$$

$$\sigma^{\rm equil}_{p=2} = 760, \quad \sigma^{\rm ortho}_{p=2} = 270 \tag{4.3.17}$$

We now compare our forecasted constraints with those obtained in [41], where a joint analysis of the one-loop power spectrum and the tree-level bispectrum was performed using BOSS DR12 data. Their 95% confidence level constraints read:

$$\sigma^{\rm equil}_{\rm lower} = -317.9, \quad \sigma^{\rm equil}_{\rm upper} = 2849 \tag{4.3.18}$$

$$\sigma^{\rm ortho}_{\rm lower} = -655.7, \quad \sigma^{\rm ortho}_{\rm upper} = 148.4 \tag{4.3.19}$$

While a direct comparison should be made with caution due to the different methodologies and assumptions, it is worth noting that our forecast—based solely on the combination of the standard power spectrum and the marked power spectrum—already shows competitive constraining power. This result is particularly encouraging given that our analysis does not include the bispectrum, which remains the main observable for detecting non-local shapes of PNG. The fact that meaningful constraints can be achieved using only two-point statistics suggests that marked observables may play a key role in future analyses.
In particular, the marked power spectrum effectively captures some of the non-Gaussian information encoded in specific bispectrum configurations, which

are relevant for equilateral and orthogonal PNG. Our results show that marked statistics can enhance sensitivity to these shapes by giving more weight to the regions of the density field where their imprint is strongest.

As also observed in real-space analyses such as [38], orthogonal PNG often yields tighter constraints than the equilateral shape. To understand this trend in our results, we analyzed the parameter correlations at $k_{\rm max} = 0.30\,h/{\rm Mpc}$ for both $p = -1$ and $p = 2$. The correlation matrices reveal that $f_{\rm NL}^{\rm equil}$ is significantly more degenerate with bias and nuisance parameters, particularly b_2, c_2, and $P_{\rm shot}$. For instance, in the $p = -1$ case we find $\rho(f_{\rm NL}^{\rm equil}, b_2) = -0.86$, $\rho(f_{\rm NL}^{\rm equil}, c_2) = -0.57$, and $\rho(f_{\rm NL}^{\rm equil}, P_{\rm shot}) = +0.53$. These strong correlations indicate that the equilateral signal partially overlaps with small-scale non-linear effects, which degrades the constraints after marginalization.

In contrast, $f_{\rm NL}^{\rm ortho}$ exhibits systematically weaker or more orthogonal correlations with the same parameters. In the $p = 2$ case, for example, we find $\rho(f_{\rm NL}^{\rm ortho}, c_2) = +0.098$, $\rho(f_{\rm NL}^{\rm ortho}, P_{\rm shot}) = +0.087$, and $\rho(f_{\rm NL}^{\rm ortho}, b_2) = +0.56$, all significantly smaller in magnitude than their equilateral counterparts. Interestingly, the only notable exception is a strong negative correlation with b_1, $\rho(f_{\rm NL}^{\rm ortho}, b_1) = -0.78$, suggesting sensitivity to large-scale amplitude, but overall the orthogonal PNG appears less entangled with nuisance directions in the parameter space.

Correlations with cosmological parameters such as n_s, h, $\omega_{\rm cdm}$, and A_s remain relatively small (typically $|\rho| < 0.3$), indicating that the observed behavior is primarily driven by late-time bias degeneracies rather than uncertainties in the background cosmology. These findings provide a natural explanation for why the constraints on orthogonal PNG are tighter in our analysis, despite both shapes contributing only at the one-loop level.

We also observe a clear improvement in constraints when switching from $p = -1$ to $p = 2$, particularly for equilateral PNG. This behavior is consistent with the idea that giving more weight to underdense regions (as done with $p > 0$) enhances the contribution from areas where the signal is stronger, such as void boundaries and the transitions between low- and high-density regions. The mark used in this work is the same as the one adopted in previous studies such as [34, 36]. More recently, [54] proposed to go beyond this simple power-law form by optimizing the mark function to enhance sensitivity to specific PNG shapes. These results suggest that further improvements could be achieved by tailoring the mark to the non-Gaussian signal of interest.

It is also important to stress that the Fisher analysis presented here relies

on an idealized setup. A realistic data analysis would need to account for survey geometry, redshift-space distortions, observational systematics, and nuisance parameters such as higher-order bias or counterterms. In particular, a proper treatment of the Alcock–Paczynski effect will be essential to model geometric distortions and extract unbiased constraints.
The bispectrum will ultimately remain a crucial ingredient for breaking degeneracies and accessing the full non-Gaussian signal. However, incorporating it into EFT-based analyses is computationally challenging: it requires dedicated bispectrum estimators, accurate modelling of the window function, and careful binning strategies. On the other hand, marked power spectra—as two-point statistics—are computationally simpler, better understood in terms of systematics, and more straightforward to apply to data. For these reasons, the combination of $P + M$ may provide a practical and powerful intermediate step between standard power spectrum analyses and full $P + B$ pipelines. In future work, it will be important to explore this synergy further, possibly integrating the bispectrum with marked statistics in a unified framework to maximize sensitivity to non-local primordial non-Gaussianity.

Chapter 5

Conclusions

Over the last decade, large-scale structure (LSS) observations have become an increasingly powerful tool for testing cosmological models and probing the physics of the early Universe. Upcoming galaxy surveys such as Euclid [1], DESI [2] and the Vera C. Rubin Observatory's LSST [3] will map the cosmic web over unprecedented volumes and with exquisite precision, offering an opportunity to extract cosmological information beyond what is accessible today. In this context, the development of accurate theoretical models and efficient statistical tools is crucial to fully exploit the potential of future data.

Standard analyses of the LSS based on the galaxy power spectrum and bispectrum, particularly within a perturbative and analytical framework, have already demonstrated the ability to deliver competitive constraints on fundamental parameters such as neutrino masses [40], dark energy properties [55], and primordial non-Gaussianities [41]. However, pushing beyond these standard observables—especially into mildly non-linear regimes—remains challenging due to theoretical and computational complexities, particularly in the treatment of higher-order correlators like the bispectrum and trispectrum.

In this landscape, marked statistics have emerged as a promising alternative [32, 33, 34, 35, 38], capable of enhancing sensitivity to specific physical effects by reweighting the galaxy density contrast field according to its local environment. Their simplicity as two-point functions, combined with their ability to capture higher-order information, positions them as valuable tools in the upcoming era of precision cosmology. This thesis contributes to this direction by extending the analytical modeling of marked statistics, exploring their potential to outperform standard analyses by specifically targeting regions where the imprint of primordial non-Gaussianity is enhanced.

We began by presenting the conventional tools used in cosmological analyses of the LSS: the galaxy power spectrum and the bispectrum. These observables were modeled using standard perturbation theory (SPT), with the power spectrum computed up to one-loop order and the bispectrum evaluated at tree level. To ensure a realistic modeling of the observables, we also accounted for galaxy bias and redshift-space distortions, which are essential ingredients when comparing theoretical predictions with data.

We then introduced the marked power spectrum, a modified two-point statistic in which the galaxy density field is weighted by a mark that depends on the local environment. This technique enables the enhancement or suppression of contributions from overdense or underdense regions, effectively highlighting specific structures where primordial non-Gaussianity may leave a stronger imprint. As such, marked statistics offer a promising avenue for probing non-Gaussian features that might remain hidden to standard analyses. Beyond primordial non-Gaussianity, the marked power spectrum has already shown strong potential in a variety of cosmological contexts. In particular, it has been proposed as a powerful probe of modified gravity models [33], and demonstrated to enhance sensitivity to cosmological parameters such as the sum of neutrino masses and the amplitude of matter fluctuations in simulation-based studies [32, 34]. More recently, its ability to constrain primordial non-Gaussianity was also pointed out in [42, 38].

We carried out an analytical study, using SPT, of the marked power spectrum at one-loop order, including the effects of non-local shapes of primordial non-Gaussianity (PNG), and extended the formalism to redshift space by building upon the framework developed in [35, 36, 38]. A dedicated numerical implementation of the model was developed and written by the author for this thesis, and its validity was confirmed by comparison with measurements from the *Quijote* simulations [44, 45]. Subsequently, it was used to perform a Fisher forecast based on the combination of the power spectrum and the marked power spectrum as observables. A key feature of this approach is its ability to upweight underdense regions, which are expected to be less affected by non-linear gravitational evolution and may therefore preserve a cleaner imprint of the primordial signal. This can lead to improved sensitivity to primordial non-Gaussianity, particularly for equilateral and orthogonal shapes, where standard power spectrum analyses offer limited constraining power.

We compared our forecast results with existing constraints obtained through a standard $P + B$ analysis performed on BOSS DR12 data [41]. Remarkably,

despite relying exclusively on two-point statistics, our combination of the standard power spectrum and the marked power spectrum yields constraints on non-local PNG of comparable magnitude. This result underscores the marked power spectrum's ability to capture a substantial portion of the information typically encoded in higher-order statistics.

Indeed, non-local shapes of primordial non-Gaussianity—such as the equilateral and orthogonal types—primarily affect the bispectrum and leave only subtle imprints on the standard power spectrum, appearing at one-loop order. However, by introducing a density-dependent weighting, marked statistics effectively incorporate higher-order information into a two-point function. This reweighting induces non-Gaussian features in the marked field, enhancing its sensitivity to the specific signatures of PNG that would otherwise require direct bispectrum measurements.

In contrast to the bispectrum, which requires the implementation of complex estimators and careful treatment of observational effects such as binning and survey window convolution, the marked power spectrum is less sensitive to these systematics and easier to model and interpret.

Moreover, it has been shown that neglecting off-diagonal terms in the bispectrum covariance can lead to a significant underestimation of parameter uncertainties, particularly for PNG [56], which are central to this study. On the other hand, the diagonal approximation for the marked power spectrum covariance has been tested and found to be more reliable for the class of marks considered in this work [32, 34]. This contributes to the practical advantage of marked statistics, making them easier to implement in realistic data analyses.

It is worth noting, however, that this property does not hold universally: recent work has shown that certain optimized marks—designed to maximize sensitivity to specific cosmological parameters—can lead to strongly non-diagonal covariances [54]. In such cases, a more careful treatment of the covariance may be required. Nonetheless, for the commonly used power-law marks explored in this thesis, the diagonal approximation remains a reasonable and validated choice, and enables a tractable yet informative forecast analysis.

Building upon this validated modeling framework, we applied it to a Fisher forecast analysis aimed at quantifying the constraining power of the marked power spectrum on primordial non-Gaussianity. To do so, we derived—for the first time—the full redshift-space contribution from equilateral and orthogonal PNG to the marked power spectrum, extending previous

results in the literature.

After validating the implementation through comparison with measurements from the *Quijote* simulations, we applied it to Fisher forecast analyses combining the standard power spectrum and the marked power spectrum. Our results show that this combination can yield competitive constraints on non-local PNG even without relying on the bispectrum. In particular, we find that the marked power spectrum is especially effective for the equilateral shape, leading to a significant tightening of the constraint—by nearly a factor of two in the forecasted error—when using a positive density-weighting parameter. For orthogonal PNG, the method also performs well and benefits from reduced degeneracies with nuisance parameters.

These results suggest that marked statistics can serve as a practical and informative alternative or complementary to the bispectrum in PNG studies, especially given their reduced sensitivity to observational systematics and computational efficiency. Future developments should focus on optimizing the mark itself and extending the analysis to real data, building upon the numerical framework developed in this work. We note that, in the analysis presented in this thesis, we adopt a perturbative model whose validity is limited to mildly nonlinear scales, up to $k_{\rm max} \simeq 0.25\,h/{\rm Mpc}$. However, simulation-based approaches [42, 57] may allow access to significantly more nonlinear regimes, potentially extending to $k_{\rm max} \simeq 0.5\,h/{\rm Mpc}$, where the cosmic web encodes additional information. These small-scale modes are particularly relevant for constraining neutrino masses, testing modified gravity models, and probing PNG with higher precision.

Future developments will require the inclusion of full observational effects, such as the Alcock–Paczynski distortion, binning, and survey geometry, within a complete pipeline suitable for real data applications. Moreover, in [36], the authors proposed a low-k correction to the marked power spectrum, motivated by the slower convergence of the perturbative series compared to the standard power spectrum. This correction introduces two additional parameters, one of which is entirely degenerate with the shot noise term. Although the impact is expected to be small also in redshift space, future investigations could shed light on its significance.

Furthermore, combining our analytical framework with numerical optimization techniques, such as Gaussian Process-based methods [54], could enable a generalized and adaptive definition of the mark function aimed at maximizing the information content on PNG. This type of optimization holds the potential to significantly enhance the utility of marked statistics in ad-

dressing key questions in cosmology and will be explored in future research.

In summary, through a combination of analytical modeling, numerical implementation, and forecast analysis, we have highlighted the strengths and practical advantages of the marked power spectrum as a complementary observable to traditional approaches.

Marked statistics offer a fresh and promising perspective—one that captures the subtle imprints of the early universe by weighting the cosmic web in novel ways. By shifting the focus toward the environmental context of cosmic structures, they enable us to access regions of parameter space that remain elusive to standard tools.

As we look ahead to the era of increasingly precise and expansive galaxy surveys, the marked power spectrum stands as a powerful probe—both elegant and efficient—capable of guiding us closer to the fingerprints of inflation and the fundamental physics that shaped the primordial cosmos. In this sense, marked statistics do not just refine our measurements; they invite us to see the universe differently, and perhaps, to uncover its earliest secrets through a new lens.

Appendix A

Power Spectrum and FFTlog

This section presents the computation of the main terms in the one-loop power spectrum and bispectrum. Additionally, we briefly discuss the numerical treatment using the FFTlog method, which is the core technique employed in the CLASS-PT library. In the following calculations, we consider equal-time correlators, and therefore, the time dependence has been omitted.

A.1 Power Spectrum

Let's consider the expressions for the two point correlator at one-loop order (2.4.12). There are two non trivial terms that are computed in the following. For the second term, using the Wick theorem (2.4.7), we obtain:

$$\begin{aligned}
\langle \delta^{(2)}(\mathbf{k}_1)\delta^{(2)}(\mathbf{k}_2)\rangle &= \Big\langle \int \frac{d^3q_1}{(2\pi)^3}\int \frac{d^3q_2}{(2\pi)^3}\,(2\pi)^3\delta_D(\mathbf{k}_1-\mathbf{q}_1-\mathbf{q}_2)F_2(\mathbf{q}_1,\mathbf{q}_2)\delta^{(1)}(\mathbf{q}_1)\delta^{(1)}(\mathbf{q}_2)\\
&\quad\times\int \frac{d^3p_1}{(2\pi)^3}\int \frac{d^3p_2}{(2\pi)^3}\,(2\pi)^3\delta_D(\mathbf{k}_2-\mathbf{p}_1-\mathbf{p}_2)F_2(\mathbf{p}_1,\mathbf{p}_2)\delta^{(1)}(\mathbf{p}_1)\delta^{(1)}(\mathbf{p}_2)\Big\rangle\\
&= \int \frac{d^3q_1}{(2\pi)^3}\int \frac{d^3p_1}{(2\pi)^3}\,F_2(\mathbf{q}_1,\mathbf{k}_1-\mathbf{q}_1)F_2(\mathbf{p}_1,\mathbf{k}_2-\mathbf{p}_1)\\
&\quad\times\langle\delta^{(1)}(\mathbf{q}_1)\delta^{(1)}(\mathbf{k}_1-\mathbf{q}_1)\delta^{(1)}(\mathbf{p}_1)\delta^{(1)}(\mathbf{k}_2-\mathbf{p}_1)\rangle\\
&= \int \frac{d^3q_1}{(2\pi)^3}\int \frac{d^3p_1}{(2\pi)^3}F_2(\mathbf{q}_1,\mathbf{k}_1-\mathbf{q}_1)F_2(\mathbf{p}_1,\mathbf{k}_2-\mathbf{p}_1)\\
&\quad\times\Big[\langle\delta(\mathbf{q}_1)\delta(\mathbf{k}_1-\mathbf{q}_1)\rangle\langle\delta(\mathbf{p}_1)\delta(\mathbf{k}_2-\mathbf{p}_1)\rangle
\end{aligned}$$

$$
\begin{aligned}
&+ \langle\delta(\mathbf{q}_1)\delta(\mathbf{p}_1)\rangle\langle\delta(\mathbf{k}_1-\mathbf{q}_1)\delta(\mathbf{k}_2-\mathbf{p}_1)\rangle \\
&+ \langle\delta(\mathbf{q}_1)\delta(\mathbf{k}_2-\mathbf{p}_1)\rangle\langle\delta(\mathbf{k}_1-\mathbf{q}_1)\delta(\mathbf{p}_1)\rangle\Big] \\
&= \int\frac{d^3q_1}{(2\pi)^3}\int\frac{d^3p_1}{(2\pi)^3}F_2(\mathbf{q}_1,\mathbf{k}_1-\mathbf{q}_1)F_2(\mathbf{p}_1,\mathbf{k}_2-\mathbf{p}_1) \\
&\times(2\pi)^6\Big[\delta_D(\mathbf{k}_1)\delta_D(\mathbf{k}_2)P_L(|\mathbf{k}_1-\mathbf{q}_1|)P_L(|\mathbf{k}_2-\mathbf{p}_1|) \\
&+ \delta_D(\mathbf{q}_1+\mathbf{p}_1)\delta_D(\mathbf{k}_1+\mathbf{k}_2-\mathbf{q}_1-\mathbf{p}_1)P_L(q_1)P_L(|\mathbf{k}_1-\mathbf{q}_1|) \\
&+ \delta_D(\mathbf{q}_1+\mathbf{k}_2-\mathbf{p}_1)\delta_D(\mathbf{k}_1+\mathbf{p}_1-\mathbf{q}_1)P_L(q_1)P_L(|\mathbf{k}_1-\mathbf{q}_1|)\Big] \\
&= \int\frac{d^3q_1}{(2\pi)^3}F_2(\mathbf{q}_1,\mathbf{k}_1-\mathbf{q}_1)F_2(\mathbf{q}_1-\mathbf{k}_1,-\mathbf{q}_1) \\
&\times(2\pi)^3\Big[\delta_D(\mathbf{k}_1+\mathbf{k}_2)P_L(q_1)P_L(|\mathbf{k}_1-\mathbf{q}_1|) \\
&+ \delta_D(\mathbf{k}_1+\mathbf{k}_2)P_L(q_1)P_L(|\mathbf{k}_1-\mathbf{q}_1|)\Big] \\
&= (2\pi)^3\delta_D(\mathbf{k}_1+\mathbf{k}_2)\,2\int\frac{d^3q}{(2\pi)^3}\left[F_2(\mathbf{q},\mathbf{k}_1-\mathbf{q})\right]^2P_L(q)P_L(|\mathbf{k}_1-\mathbf{q}|),
\end{aligned}
\tag{A.1.1}
$$

where in the last step we used the property $F_2(\mathbf{q}_1,\mathbf{k}_1-\mathbf{q}_1)=F_2(\mathbf{q}_1-\mathbf{k}_1,-\mathbf{q}_1)$.
For the third term:

$$
\begin{aligned}
\langle\delta^{(3)}(\mathbf{k}_1)\delta^{(1)}(\mathbf{k}_2)\rangle &= 2\Big\langle\int\frac{d^3q_1}{(2\pi)^3}\int\frac{d^3q_2}{(2\pi)^3}\int\frac{d^3q_3}{(2\pi)^3}(2\pi)^3\delta_D(\mathbf{k}_1-\mathbf{q}_1-\mathbf{q}_2-\mathbf{q}_3) \\
&\times F_3(\mathbf{q}_1,\mathbf{q}_2,\mathbf{q}_3)\delta(\mathbf{q}_1)\delta(\mathbf{q}_2)\delta(\mathbf{q}_3)\delta(\mathbf{k}_2)\Big\rangle \\
&= 2\int\frac{d^3q_1}{(2\pi)^3}\int\frac{d^3q_2}{(2\pi)^3}F_3(\mathbf{q}_1,\mathbf{q}_2,\mathbf{k}_1-\mathbf{q}_1-\mathbf{q}_2) \\
&\times\langle\delta(\mathbf{q}_1)\delta(\mathbf{q}_2)\delta(\mathbf{k}_1-\mathbf{q}_1-\mathbf{q}_2)\delta(\mathbf{k}_2)\rangle \\
&= 2\int\frac{d^3q_1}{(2\pi)^3}\int\frac{d^3q_2}{(2\pi)^3}F_3(\mathbf{q}_1,\mathbf{q}_2,\mathbf{k}_1-\mathbf{q}_1-\mathbf{q}_2) \\
&\times(2\pi)^6\Big[\delta_D(\mathbf{q}_1+\mathbf{q}_2)P_L(q_1)\delta_D(\mathbf{k}_1+\mathbf{k}_2-\mathbf{q}_1-\mathbf{q}_2)P_L(|\mathbf{k}_1-\mathbf{q}_1-\mathbf{q}_2|) \\
&+ \delta_D(\mathbf{k}_1-\mathbf{q}_2)P_L(q_1)\delta_D(\mathbf{k}_2+\mathbf{q}_2)P_L(k_2) \\
&+ \delta_D(\mathbf{q}_1+\mathbf{k}_2)P_L(q_1)\delta_D(\mathbf{k}_1-\mathbf{q}_1)P_L(|\mathbf{k}_1-\mathbf{q}_1-\mathbf{q}_2|)\Big] \\
&= (2\pi)^3\delta_D(\mathbf{k}_1+\mathbf{k}_2)\,2\int\frac{d^3q_1}{(2\pi)^3}F_3(\mathbf{q}_1,-\mathbf{q}_1,\mathbf{k}_1)\Big[P_L(q_1)P_L(k_1)
\end{aligned}
$$

$$+ P_L(q_1)P_L(k_2) + P_L(q_1)P_L(k_1)\Big]$$
$$= (2\pi)^3\,\delta_D(\mathbf{k}_1+\mathbf{k}_2)\,6\int \frac{d^3q}{(2\pi)^3}\,F_3(\mathbf{q},-\mathbf{q},\mathbf{k}_1)P_L(q)P_L(k_1) \tag{A.1.2}$$

A.2 Bispectrum

Now, let's compute the bispectrum, whose result is presented in Eq. (2.4.17): Using perturbation theory and applying Wick's theorem, the tree-level bispectrum consists of three terms. These terms arise from considering the expansion of the nonlinear density field, $\delta = \delta^{(1)} + \delta^{(2)} + \cdots$, where $\delta^{(1)}$ is the linear (Gaussian) contribution and $\delta^{(2)}$ represents the second-order (nonlinear) correction. The three terms correspond to contributions where one of the fields is $\delta^{(2)}$ and the other two are $\delta^{(1)}$:

$$\begin{aligned}\langle\delta(\mathbf{k}_1)\delta(\mathbf{k}_2)\delta(\mathbf{k}_3)\rangle &= \langle\delta^{(2)}(\mathbf{k}_1)\delta^{(1)}(\mathbf{k}_2)\delta^{(1)}(\mathbf{k}_3)\rangle \\ &+ \langle\delta^{(1)}(\mathbf{k}_1)\delta^{(2)}(\mathbf{k}_2)\delta^{(1)}(\mathbf{k}_3)\rangle \\ &+ \langle\delta^{(1)}(\mathbf{k}_1)\delta^{(1)}(\mathbf{k}_2)\delta^{(2)}(\mathbf{k}_3)\rangle. \end{aligned}\tag{A.2.1}$$

In this expansion, the terms involving only $\delta^{(1)}$ vanish because, according to the Wick theorem, the three-point correlator of a Gaussian field is zero. Hence, the bispectrum originates from the contributions of the second-order term $\delta^{(2)}$, which introduces non-Gaussianity via nonlinear mode coupling. Let us calculate the first term explicitly. Using Eq. (2.3.17), we have:

$$\begin{aligned}&\langle\delta^{(2)}(\mathbf{k}_1)\delta^{(1)}(\mathbf{k}_2)\delta^{(1)}(\mathbf{k}_3)\rangle \\ &= \left\langle \int \frac{d^3q}{(2\pi)^3}\int \frac{d^3p}{(2\pi)^3}\,(2\pi)^3\delta_D(\mathbf{k}_1-\mathbf{q}-\mathbf{p})F_2(\mathbf{q},\mathbf{p})\delta(\mathbf{q})\delta(\mathbf{p})\delta(\mathbf{k}_2)\delta(\mathbf{k}_3)\right\rangle \\ &= \int \frac{d^3q}{(2\pi)^3}\int \frac{d^3p}{(2\pi)^3}\,(2\pi)^3\delta_D(\mathbf{k}_1-\mathbf{q}-\mathbf{p})F_2(\mathbf{q},\mathbf{p})\langle\delta(\mathbf{q})\delta(\mathbf{p})\delta(\mathbf{k}_2)\delta(\mathbf{k}_3)\rangle. \end{aligned}\tag{A.2.2}$$

Now, due to the Wick theorem, Eq. (2.4.7), we can arrange the term in brackets as follows:

$$\begin{aligned}\langle\delta(\mathbf{q})\delta(\mathbf{p})\delta(\mathbf{k}_2)\delta(\mathbf{k}_3)\rangle &= \langle\delta(\mathbf{q})\delta(\mathbf{p})\rangle\langle\delta(\mathbf{k}_2)\delta(\mathbf{k}_3)\rangle + \langle\delta(\mathbf{q})\delta(\mathbf{k}_2)\rangle\langle\delta(\mathbf{p})\delta(\mathbf{k}_3)\rangle \\ &+ \langle\delta(\mathbf{q})\delta(\mathbf{k}_3)\rangle\langle\delta(\mathbf{p})\delta(\mathbf{k}_2)\rangle. \end{aligned}\tag{A.2.3}$$

Therefore, Eq. (A.2.2) becomes:

$$
\begin{aligned}
&= \int \frac{d^3q}{(2\pi)^3} \int \frac{d^3p}{(2\pi)^3} (2\pi)^3 \delta_D(\mathbf{k}_1 - \mathbf{q} - \mathbf{p}) F_2(\mathbf{q}, \mathbf{p}) \Big[\langle \delta(\mathbf{q})\delta(\mathbf{p})\rangle \langle \delta(\mathbf{k}_2)\delta(\mathbf{k}_3)\rangle \\
&\quad + \langle \delta(\mathbf{q})\delta(\mathbf{k}_2)\rangle \langle \delta(\mathbf{p})\delta(\mathbf{k}_3)\rangle + \langle \delta(\mathbf{q})\delta(\mathbf{k}_3)\rangle \langle \delta(\mathbf{p})\delta(\mathbf{k}_2)\rangle \Big] \\
&= \int \frac{d^3q}{(2\pi)^3} F_2(\mathbf{q}, \mathbf{k}_1 - \mathbf{q}) (2\pi)^6 \Big[\delta_D(\mathbf{k}_1)\delta_D(\mathbf{k}_2 + \mathbf{k}_3) P_L(q) P_L(k_2) \\
&\quad + \delta_D(\mathbf{q} + \mathbf{k}_2)\delta_D(\mathbf{k}_1 + \mathbf{k}_3 - \mathbf{q}) P_L(k_2) P_L(k_3) \\
&\quad + \delta_D(\mathbf{q} + \mathbf{k}_3)\delta_D(\mathbf{k}_1 + \mathbf{k}_2 - \mathbf{q}) P_L(k_3) P_L(k_2) \Big],
\end{aligned}
\tag{A.2.4}
$$

where in the last passage we have used the definition of the power spectrum, Eq. (2.4.3). Moreover, since the first term in square brackets vanishes, we obtain:

$$
\langle \delta^{(2)}(\mathbf{k}_1)\delta^{(1)}(\mathbf{k}_2)\delta^{(1)}(\mathbf{k}_3)\rangle = (2\pi)^3 \delta_D(\mathbf{k}_1 + \mathbf{k}_2 + \mathbf{k}_3)\, 2F_2(\mathbf{k}_2, \mathbf{k}_3) P_L(k_2) P_L(k_3). \tag{A.2.5}
$$

Finally, considering all terms of Eq. (A.2.1), we arrive at:

$$
\begin{aligned}
\langle \delta(\mathbf{k}_1)\delta(\mathbf{k}_2)\delta(\mathbf{k}_3)\rangle = (2\pi)^3 \delta_D(\mathbf{k}_1 + \mathbf{k}_2 + \mathbf{k}_3) \times \\
\Big[2F_2(\mathbf{k}_2, \mathbf{k}_3) P_L(k_2) P_L(k_3) \\
+ 2F_2(\mathbf{k}_1, \mathbf{k}_3) P_L(k_1) P_L(k_3) \\
+ 2F_2(\mathbf{k}_1, \mathbf{k}_2) P_L(k_1) P_L(k_2) \Big],
\end{aligned}
\tag{A.2.6}
$$

obtaining a final form for the bispectrum computed at tree level:

$$
B(\mathbf{k}_1, \mathbf{k}_2, \mathbf{k}_3) = 2F_2(\mathbf{k}_1, \mathbf{k}_2) P_L(k_1) P_L(k_2) + \text{cyc.} \tag{A.2.7}
$$

A.3 FFTlog Method

In this section, we briefly outline the core methodology of the CLASS-PT library[1], which is used for calculating loop corrections in cosmological perturbation theory. More detailed discussions can be found in [58, 18]. The method relies on approximating a ΛCDM-like cosmology as a finite sum of complex power-law universes. This decomposition is naturally achieved using the FFTLog algorithm.
A key advantage of this approach is that the computationally demanding part of the calculation, which is independent of the specific cosmology, only needs to be performed once. The results can then be reused for various predictions, making the method highly efficient. The evaluation of standard loop diagrams is ultimately reduced to a simple matrix multiplication.

Before performing any integrals, the linear power spectrum is expressed as a superposition of self-similar, power-law cosmologies. This is achieved using a Fourier transform in logarithmic wavenumber space ($\log k$). For a given range of wavenumbers, $[k_{\rm min}, k_{\rm max}]$, and N sampling points, the linear power spectrum can be approximated as:

$$\bar{P}_{\rm lin}(k_n) = \sum_{m=-N/2}^{N/2} c_m k_n^{\nu+i\eta_m}, \tag{A.3.1}$$

where the coefficients c_m and the frequencies η_m are given by:

$$c_m = \frac{1}{N}\sum_{l=0}^{N-1} P_{\rm lin}(k_l) k_l^{-\nu} k_{\rm min}^{-i\eta_m} e^{-2\pi i m l/N}, \quad \eta_m = \frac{2\pi m}{\log(k_{\rm max}/k_{\rm min})}. \tag{A.3.2}$$

Here, the parameter ν, referred to as the *bias*, is an arbitrary real number. The decomposition in Eq. (A.3.1) is particularly useful because it separates the cosmology-dependent part, which is entirely encoded in the coefficients c_m, from the loop calculations. These calculations are then performed for simpler, idealized cosmologies.
For fixed values of ν, $k_{\rm min}$, $k_{\rm max}$, and the number of sampling points N, the most computationally intensive part of the calculation (involving momentum integrals) can be performed once and stored as a table of precomputed values. This makes the method highly reusable for various cosmological models.

[1] github.com/michalychforever/CLASS-PT

We can then observe that F_n kernels in terms of integer powers of k^2, q^2, and $|\mathbf{k}-\mathbf{q}|^2$. Consequently, the one-loop power spectrum is expressed as a sum of simpler momentum integrals of the form:

$$\int_{\mathbf{q}} \frac{1}{q^{2\nu_1}|\mathbf{k}-\mathbf{q}|^{2\nu_2}} \equiv k^{3-2\nu_{12}} I(\nu_1,\nu_2), \tag{A.3.3}$$

where ν_1 and ν_2 are, in general, complex numbers, and $\nu_{12} = \nu_1 + \nu_2$. The function $I(\nu_1,\nu_2)$, which depends on Gamma functions, can be determined analytically.
Using this formalism, the one-loop integrals for P_{22} and P_{13} can be approximated as:

$$\bar{P}_{22}(k) = k^3 \sum_{m_1,m_2} c_{m_1} k^{-2\nu_1} \cdot M_{22}(\nu_1,\nu_2) \cdot c_{m_2} k^{-2\nu_2}, \tag{A.3.4}$$

$$\bar{P}_{13}(k) = k^3 P_{\rm lin}(k) \sum_{m_1} c_{m_1} k^{-2\nu_1} \cdot M_{13}(\nu_1), \tag{A.3.5}$$

where $M_{22}(\nu_1,\nu_2)$ is a matrix proportional to $I(\nu_1,\nu_2)$, and $M_{13}(\nu_1)$ is a vector dependent on ν_1.
This method forms the core of the CLASS-PT approach. In the referenced papers, this framework is extended to compute the one-loop power spectrum for biased tracers, redshift-space distortions, and the bispectrum. The results exhibit excellent agreement with direct numerical integration while being significantly faster.

Appendix B

Marked Power Spectrum Details

Firstly, we remember some useful Legendre polynomials:

$$\begin{aligned}
\mathcal{L}_0(\mu) &= 1 \quad \text{(monopole)} \\
\mathcal{L}_2(\mu) &= \frac{3\mu^2 - 1}{2} \quad \text{(quadrupole)} \\
\mathcal{L}_4(\mu) &= \frac{35\mu^4 - 30\mu^2 + 3}{8} \quad \text{(hexadecapole)}
\end{aligned} \tag{B.0.1}$$

where in our applications, μ is the cosine of the angle between the wavevector and the line of sight. We can write:

$$\mu^2 \equiv \cos^2(\theta) = \frac{2}{3}\mathcal{L}_2(\mu) + \frac{1}{3}\mathcal{L}_0(\mu), \tag{B.0.2}$$

$$\mu^4 = \frac{8}{35}L_4(\mu) + \frac{4}{7}L_2(\mu) + \frac{1}{5}L_0(\mu) \tag{B.0.3}$$

The first-order kernel Z_1 in redshift space is

$$Z_1(\mathbf{k}) = b_1 + f\mu^2, \tag{B.0.4}$$

where here we are neglecting the $\mathbf{k}$ pedix on μ for simplicity. Writing it in terms of Legendre polynomials, we get:

$$Z_1(k, \mu) = \left(b_1 + \frac{f}{3}\right)\mathcal{L}_0(\mu) + \frac{2f}{3}\mathcal{L}_2(\mu) \tag{B.0.5}$$

Now we compute the multipole expansion for Z_1^2 that will be useful:

$$Z_1^2(k,\mu) = \left(b_1 + f\mu^2\right)^2 = b_1^2 + 2b_1 f\mu^2 + f^2\mu^4, \tag{B.0.6}$$

and substituting the expansions of μ^2 and μ^4 we get:

$$Z_1^2(k,\mu) = b_1^2 + 2b_1 f\left(\frac{1}{3}L_0(\mu) + \frac{2}{3}L_2(\mu)\right) + f^2\left(\frac{1}{5}L_0(\mu) + \frac{4}{7}L_2(\mu) + \frac{8}{35}L_4(\mu)\right).$$

This gives the final multipole expansion:

$$Z_1^2(k,\mu) = \left(b_1^2 + \frac{2}{3}b_1 f + \frac{1}{5}f^2\right)L_0(\mu) + \left(\frac{4}{3}b_1 f + \frac{4}{7}f^2\right)L_2(\mu) + \frac{8}{35}f^2 L_4(\mu) \tag{B.0.7}$$

We now expand the product of the kernels involved in the M_{22}^B integral, i.e., $Z_1(\mathbf{p})Z_1(\mathbf{k}-\mathbf{p})Z_2(\mathbf{p},\mathbf{k}-\mathbf{p})$, in powers of $\mu_{\mathbf{p}}$ and $\mu_{\mathbf{k}}$ for each combination of bias terms that arise from the multiplication of the Z kernels. To organize the result systematically, we label each term by $\left(\alpha,\beta\right)$, where α is the power of $\mu_{\mathbf{p}}$ and β is the power of $\mu_{\mathbf{k}}$. Hence, a typical contribution has the form

$$(\text{bias factors}) \times \mu_{\mathbf{p}}^{\alpha}\,\mu_{\mathbf{k}}^{\beta}.$$

For b_1: (B.0.8)

$$(0,4): \left(-\frac{f^2k^4}{14\,|\mathbf{k}-\mathbf{p}|^4}+\frac{f^2k^5\,x}{2\,p\,|\mathbf{k}-\mathbf{p}|^4}-\frac{3\,f^2k^4\,x^2}{7\,|\mathbf{k}-\mathbf{p}|^4}\right),$$

$$(1,3): \left(\frac{f^2k^3\,p}{7\,|\mathbf{k}-\mathbf{p}|^4}-\frac{f^2k^4\,x}{|\mathbf{k}-\mathbf{p}|^4}+\frac{6\,f^2k^3\,p\,x^2}{7\,|\mathbf{k}-\mathbf{p}|^4}\right),$$

$$(1,5): \left(\frac{f^3k^5}{2\,p\,|\mathbf{k}-\mathbf{p}|^4}\right),$$

$$(2,2): \left(\frac{f^2k^4}{7\,|\mathbf{k}-\mathbf{p}|^4}-\frac{f^2k^2\,p^2}{7\,|\mathbf{k}-\mathbf{p}|^4}+\frac{f^2k^5\,x}{p\,|\mathbf{k}-\mathbf{p}|^4}+\frac{8\,f^2k^3\,p\,x}{7\,|\mathbf{k}-\mathbf{p}|^4}\right.$$
$$\left.-\frac{15\,f^2k^4\,x^2}{7\,|\mathbf{k}-\mathbf{p}|^4}-\frac{6\,f^2k^2\,p^2\,x^2}{7\,|\mathbf{k}-\mathbf{p}|^4}+\frac{6\,f^2k^3\,p\,x^3}{7\,|\mathbf{k}-\mathbf{p}|^4}\right),$$

$$(2,4): \left(-\frac{f^3k^4}{|\mathbf{k}-\mathbf{p}|^4}\right),$$

$$(3,1): \left(-\frac{3\,f^2k^3\,p}{7\,|\mathbf{k}-\mathbf{p}|^4}-\frac{f^2k^4\,x}{|\mathbf{k}-\mathbf{p}|^4}+\frac{10\,f^2k^3\,p\,x^2}{7\,|\mathbf{k}-\mathbf{p}|^4}\right),$$

$$(3,3): \left(\frac{f^3k^5}{p\,|\mathbf{k}-\mathbf{p}|^4}+\frac{f^3k^3\,p}{|\mathbf{k}-\mathbf{p}|^4}-\frac{2\,f^3k^4\,x}{|\mathbf{k}-\mathbf{p}|^4}\right),$$

$$(4,0): \left(\frac{3\,f^2k^2\,p^2}{14\,|\mathbf{k}-\mathbf{p}|^4}+\frac{f^2k^3\,p\,x}{2\,|\mathbf{k}-\mathbf{p}|^4}-\frac{5\,f^2k^2\,p^2\,x^2}{7\,|\mathbf{k}-\mathbf{p}|^4}\right),$$

$$(4,2): \left(-\frac{3\,f^3k^4}{2\,|\mathbf{k}-\mathbf{p}|^4}-\frac{f^3k^2\,p^2}{2\,|\mathbf{k}-\mathbf{p}|^4}+\frac{3\,f^3k^3\,p\,x}{|\mathbf{k}-\mathbf{p}|^4}\right),$$

$$(5,1): \left(\frac{f^3k^3\,p}{2\,|\mathbf{k}-\mathbf{p}|^4}-\frac{f^3k^2\,p^2\,x}{|\mathbf{k}-\mathbf{p}|^4}\right).$$

For b_1^2: (B.0.9)

$$(0,2): \left(\frac{f\,k^4}{7\,|\mathbf{k}-\mathbf{p}|^4} - \frac{f\,k^2\,p^2}{14\,|\mathbf{k}-\mathbf{p}|^4} + \frac{f\,k^5\,x}{p\,|\mathbf{k}-\mathbf{p}|^4} + \frac{9\,f\,k^3\,p\,x}{14\,|\mathbf{k}-\mathbf{p}|^4} - \frac{15\,f\,k^4\,x^2}{7\,|\mathbf{k}-\mathbf{p}|^4} - \frac{3\,f\,k^2\,p^2\,x^2}{7\,|\mathbf{k}-\mathbf{p}|^4} + \frac{6\,f\,k^3\,p\,x^3}{7\,|\mathbf{k}-\mathbf{p}|^4} \right),$$

$$(0,4): \left(\frac{f^2\,k^4}{2\,|\mathbf{k}-\mathbf{p}|^4} \right),$$

$$(1,1): \left(-\frac{3\,f\,k^3\,p}{7\,|\mathbf{k}-\mathbf{p}|^4} - \frac{f\,k^4\,x}{|\mathbf{k}-\mathbf{p}|^4} + \frac{10\,f\,k^3\,p\,x^2}{7\,|\mathbf{k}-\mathbf{p}|^4} \right),$$

$$(1,3): \left(\frac{f^2\,k^5}{p\,|\mathbf{k}-\mathbf{p}|^4} - \frac{f^2\,k^3\,p}{2\,|\mathbf{k}-\mathbf{p}|^4} - \frac{2\,f^2\,k^4\,x}{|\mathbf{k}-\mathbf{p}|^4} \right),$$

$$(2,0): \left(\frac{3\,f\,k^4}{14\,|\mathbf{k}-\mathbf{p}|^4} + \frac{3\,f\,k^2\,p^2}{7\,|\mathbf{k}-\mathbf{p}|^4} + \frac{f\,k^5\,x}{2\,p\,|\mathbf{k}-\mathbf{p}|^4} + \frac{4\,f\,k^3\,p\,x}{7\,|\mathbf{k}-\mathbf{p}|^4} - \frac{12\,f\,k^4\,x^2}{7\,|\mathbf{k}-\mathbf{p}|^4} - \frac{10\,f\,k^2\,p^2\,x^2}{7\,|\mathbf{k}-\mathbf{p}|^4} + \frac{10\,f\,k^3\,p\,x^3}{7\,|\mathbf{k}-\mathbf{p}|^4} \right),$$

$$(2,2): \left(-\frac{f^2\,k^4}{|\mathbf{k}-\mathbf{p}|^4} + \frac{f^2\,k^2\,p^2}{2\,|\mathbf{k}-\mathbf{p}|^4} + \frac{2\,f^2\,k^3\,p\,x}{|\mathbf{k}-\mathbf{p}|^4} \right),$$

$$(3,1): \left(\frac{f^2\,k^5}{2\,p\,|\mathbf{k}-\mathbf{p}|^4} + \frac{f^2\,k^3\,p}{|\mathbf{k}-\mathbf{p}|^4} - \frac{2\,f^2\,k^4\,x}{|\mathbf{k}-\mathbf{p}|^4} - \frac{2\,f^2\,k^2\,p^2\,x}{|\mathbf{k}-\mathbf{p}|^4} + \frac{2\,f^2\,k^3\,p\,x^2}{|\mathbf{k}-\mathbf{p}|^4} \right).$$

For b_1^3: (B.0.10)

$$(0,0): \left(\frac{3\,k^4}{14\,|\mathbf{k}-\mathbf{p}|^4}+\frac{3\,k^2\,p^2}{14\,|\mathbf{k}-\mathbf{p}|^4}+\frac{k^5\,x}{2\,p\,|\mathbf{k}-\mathbf{p}|^4}+\frac{k^3\,p\,x}{14\,|\mathbf{k}-\mathbf{p}|^4}\right.$$
$$\left.-\frac{12\,k^4\,x^2}{7\,|\mathbf{k}-\mathbf{p}|^4}-\frac{5\,k^2\,p^2\,x^2}{7\,|\mathbf{k}-\mathbf{p}|^4}+\frac{10\,k^3\,p\,x^3}{7\,|\mathbf{k}-\mathbf{p}|^4}\right),$$

$$(0,2): \left(\frac{f\,k^4}{2\,|\mathbf{k}-\mathbf{p}|^4}+\frac{f\,k^2\,p^2}{2\,|\mathbf{k}-\mathbf{p}|^4}-\frac{f\,k^3\,p\,x}{|\mathbf{k}-\mathbf{p}|^4}\right),$$

$$(1,1): \left(\frac{f\,k^5}{2\,p\,|\mathbf{k}-\mathbf{p}|^4}+\frac{f\,k^3\,p}{2\,|\mathbf{k}-\mathbf{p}|^4}-\frac{2\,f\,k^4\,x}{|\mathbf{k}-\mathbf{p}|^4}-\frac{f\,k^2\,p^2\,x}{|\mathbf{k}-\mathbf{p}|^4}+\frac{2\,f\,k^3\,p\,x^2}{|\mathbf{k}-\mathbf{p}|^4}\right).$$

For b_2: (B.0.11)

$$(2,2): \left(\frac{f^2\,k^4}{2\,|\mathbf{k}-\mathbf{p}|^4}+\frac{f^2\,k^2\,p^2}{2\,|\mathbf{k}-\mathbf{p}|^4}-\frac{f^2\,k^3\,p\,x}{|\mathbf{k}-\mathbf{p}|^4}\right),$$

$$(3,1): \left(-\frac{f^2\,k^3\,p}{|\mathbf{k}-\mathbf{p}|^4}-\frac{f^2\,k\,p^3}{|\mathbf{k}-\mathbf{p}|^4}+\frac{2\,f^2\,k^2\,p^2\,x}{|\mathbf{k}-\mathbf{p}|^4}\right),$$

$$(4,0): \left(\frac{f^2\,k^2\,p^2}{2\,|\mathbf{k}-\mathbf{p}|^4}+\frac{f^2\,p^4}{2\,|\mathbf{k}-\mathbf{p}|^4}-\frac{f^2\,k\,p^3\,x}{|\mathbf{k}-\mathbf{p}|^4}\right).$$

For $b_1 b_2$: (B.0.12)

$$(0,2): \left(\frac{f\,k^4}{2\,|\mathbf{k}-\mathbf{p}|^4}+\frac{f\,k^2\,p^2}{2\,|\mathbf{k}-\mathbf{p}|^4}-\frac{f\,k^3\,p\,x}{|\mathbf{k}-\mathbf{p}|^4}\right),$$

$$(1,1): \left(-\frac{f\,k^3\,p}{|\mathbf{k}-\mathbf{p}|^4}-\frac{f\,k\,p^3}{|\mathbf{k}-\mathbf{p}|^4}+\frac{2\,f\,k^2\,p^2\,x}{|\mathbf{k}-\mathbf{p}|^4}\right),$$

$$(2,0): \left(\frac{f\,k^4}{2\,|\mathbf{k}-\mathbf{p}|^4}+\frac{3\,f\,k^2\,p^2}{2\,|\mathbf{k}-\mathbf{p}|^4}+\frac{f\,p^4}{|\mathbf{k}-\mathbf{p}|^4}-\frac{2\,f\,k^3\,p\,x}{|\mathbf{k}-\mathbf{p}|^4}-\frac{3\,f\,k\,p^3\,x}{|\mathbf{k}-\mathbf{p}|^4}+\frac{2\,f\,k^2\,p^2\,x^2}{|\mathbf{k}-\mathbf{p}|^4}\right).$$

For $b_1^2 b_2$: (B.0.13)

$$(0,0): \left(-\frac{k^4}{|\mathbf{k}-\mathbf{p}|^4}-\frac{k^2\,p^2}{|\mathbf{k}-\mathbf{p}|^4}+\frac{2\,k^3\,p\,x}{|\mathbf{k}-\mathbf{p}|^4}+\frac{k^4\,x^2}{|\mathbf{k}-\mathbf{p}|^4}+\frac{k^2\,p^2\,x^2}{|\mathbf{k}-\mathbf{p}|^4}-\frac{2\,k^3\,p\,x^3}{|\mathbf{k}-\mathbf{p}|^4}\right).$$

For $b_{\mathcal{G}_2}$: (B.0.14)

$$(2,2): \left(-\frac{f^2k^4}{|\mathbf{k}-\mathbf{p}|^4}+\frac{f^2k^4\,x^2}{|\mathbf{k}-\mathbf{p}|^4}\right),$$

$$(3,1): \left(2\,\frac{f^2k^3\,p}{|\mathbf{k}-\mathbf{p}|^4}\;-\;2\,\frac{f^2k^3\,p\,x^2}{|\mathbf{k}-\mathbf{p}|^4}\right),$$

$$(4,0): \left(-\frac{f^2k^2\,p^2}{|\mathbf{k}-\mathbf{p}|^4}+\frac{f^2k^2\,p^2\,x^2}{|\mathbf{k}-\mathbf{p}|^4}\right).$$

For $b_1 b_{\mathcal{G}_2}$: (B.0.15)

$$(0,2): \left(-\frac{f\,k^4}{|\mathbf{k}-\mathbf{p}|^4}+\frac{f\,k^4\,x^2}{|\mathbf{k}-\mathbf{p}|^4}\right),$$

$$(1,1): \left(\frac{2\,f\,k^3\,p}{|\mathbf{k}-\mathbf{p}|^4}\;-\;\frac{2\,f\,k^3\,p\,x^2}{|\mathbf{k}-\mathbf{p}|^4}\right),$$

$$(2,0): \left(-\frac{f\,k^4}{|\mathbf{k}-\mathbf{p}|^4}-\frac{2\,f\,k^2\,p^2}{|\mathbf{k}-\mathbf{p}|^4}+\frac{2\,f\,k^3\,p\,x}{|\mathbf{k}-\mathbf{p}|^4}+\frac{f\,k^4\,x^2}{|\mathbf{k}-\mathbf{p}|^4}+\frac{2\,f\,k^2\,p^2\,x^2}{|\mathbf{k}-\mathbf{p}|^4}-\frac{2\,f\,k^3\,p\,x^3}{|\mathbf{k}-\mathbf{p}|^4}\right).$$

For $b_1^2 b_{\mathcal{G}_2}$: (B.0.16)

$$(0,0): \left(\frac{k^2\left(-1+x^2\right)}{|\mathbf{k}-\mathbf{p}|^2}\right).$$

For the term with no bias: (B.0.17)

$$(2,4): \left(-\frac{f^3\,k^4}{14\,|\mathbf{k}-\mathbf{p}|^4}+\frac{f^3\,k^5\,x}{2\,p\,|\mathbf{k}-\mathbf{p}|^4}-\frac{3\,f^3\,k^4\,x^2}{7\,|\mathbf{k}-\mathbf{p}|^4}\right),$$

$$(3,3): \left(\frac{f^3\,k^3\,p}{7\,|\mathbf{k}-\mathbf{p}|^4}-\frac{f^3\,k^4\,x}{|\mathbf{k}-\mathbf{p}|^4}+\frac{6\,f^3\,k^3\,p\,x^2}{7\,|\mathbf{k}-\mathbf{p}|^4}\right),$$

$$(3,5): \left(\frac{f^4\,k^5}{2\,p\,|\mathbf{k}-\mathbf{p}|^4}\right),$$

$$(4,2): \left(-\frac{f^3\,k^2\,p^2}{14\,|\mathbf{k}-\mathbf{p}|^4}+\frac{f^3\,k^3\,p\,x}{2\,|\mathbf{k}-\mathbf{p}|^4}-\frac{3\,f^3\,k^2\,p^2\,x^2}{7\,|\mathbf{k}-\mathbf{p}|^4}\right),$$

$$(4,4): \left(-\frac{3\,f^4\,k^4}{2\,|\mathbf{k}-\mathbf{p}|^4}\right),$$

$$(5,3): \left(\frac{3\,f^4\,k^3\,p}{2\,|\mathbf{k}-\mathbf{p}|^4}\right),$$

$$(6,2): \left(-\frac{f^4\,k^2\,p^2}{2\,|\mathbf{k}-\mathbf{p}|^4}\right).$$

Now, we write the same expansion for the $Z_1(\mathbf{k})Z_1(\mathbf{p})Z_2(\mathbf{k},-\mathbf{p})$ term that is involved in M_{13}^B.

For b_1: (B.0.18)

$$(0,2): \left(\frac{3\,f\,k^2}{7\,|\mathbf{k}-\mathbf{p}|^2} - \frac{f\,k^3\,x}{2\,p\,|\mathbf{k}-\mathbf{p}|^2} - \frac{f\,k\,p\,x}{2\,|\mathbf{k}-\mathbf{p}|^2} + \frac{4\,f\,k^2\,x^2}{7\,|\mathbf{k}-\mathbf{p}|^2}\right),$$

$$(1,1): \left(\frac{6\,f\,k\,p}{7\,|\mathbf{k}-\mathbf{p}|^2} - \frac{f\,k^2\,x}{|\mathbf{k}-\mathbf{p}|^2} - \frac{f\,p^2\,x}{|\mathbf{k}-\mathbf{p}|^2} + \frac{8\,f\,k\,p\,x^2}{7\,|\mathbf{k}-\mathbf{p}|^2}\right),$$

$$(1,3): \left(-\frac{f^2\,k^3}{2\,p\,|\mathbf{k}-\mathbf{p}|^2} - \frac{f^2\,k\,p}{2\,|\mathbf{k}-\mathbf{p}|^2} + \frac{f^2\,k^2\,x}{|\mathbf{k}-\mathbf{p}|^2}\right),$$

$$(2,0): \left(\frac{5\,f}{7} - \frac{f\,k\,x}{2\,p} - \frac{f\,p\,x}{2\,k} + \frac{2\,f\,x^2}{7} + \frac{3\,f\,p^2}{7\,|\mathbf{k}-\mathbf{p}|^2} - \frac{f\,k\,p\,x}{2\,|\mathbf{k}-\mathbf{p}|^2} - \frac{f\,p^3\,x}{2\,k\,|\mathbf{k}-\mathbf{p}|^2} + \frac{4\,f\,p^2\,x^2}{7\,|\mathbf{k}-\mathbf{p}|^2}\right),$$

$$(2,2): \left(\frac{f^2}{2} + \frac{f^2\,k^2}{|\mathbf{k}-\mathbf{p}|^2} + \frac{f^2\,p^2}{|\mathbf{k}-\mathbf{p}|^2} - \frac{2\,f^2\,k\,p\,x}{|\mathbf{k}-\mathbf{p}|^2}\right),$$

$$(3,1): \left(-\frac{f^2\,k}{2\,p} - \frac{f^2\,p}{2\,k} - \frac{f^2\,k\,p}{2\,|\mathbf{k}-\mathbf{p}|^2} - \frac{f^2\,p^3}{2\,k\,|\mathbf{k}-\mathbf{p}|^2} + \frac{f^2\,p^2\,x}{|\mathbf{k}-\mathbf{p}|^2}\right),$$

$$(4,0): \left(\frac{f^2}{2}\right).$$

For b_1^2: (B.0.19)

$$(0,0): \left(\frac{5}{7} - \frac{k\,x}{2\,p} - \frac{p\,x}{2\,k} + \frac{2\,x^2}{7}\right),$$

$$(0,2): \left(\frac{f}{2}\right),$$

$$(1,1): \left(-\frac{f\,k}{2\,p} - \frac{f\,p}{2\,k}\right),$$

$$(2,0): \left(\frac{f}{2}\right).$$

For b_2: (B.0.20)

$$(2,0): \frac{f}{2}.$$

For $b_1 b_2$: (B.0.21)

$$(0,0): \frac{1}{2}.$$

For $b_{\mathcal{G}_2}$: (B.0.22)

$$(2,0): -f + f x^2.$$

For $b_1 b_{\mathcal{G}_2}$: (B.0.23)

$$(0,0): -1 + x^2$$

For the term with no bias: (B.0.24)

$$(2,2): \left(\frac{3\,f^2\,k^2}{7\,|\mathbf{k}-\mathbf{p}|^2} - \frac{f^2\,k^3\,x}{2\,p\,|\mathbf{k}-\mathbf{p}|^2} - \frac{f^2\,k\,p\,x}{2\,|\mathbf{k}-\mathbf{p}|^2} + \frac{4\,f^2\,k^2\,x^2}{7\,|\mathbf{k}-\mathbf{p}|^2}\right),$$

$$(3,1): \left(\frac{6\,f^2\,k\,p}{7\,|\mathbf{k}-\mathbf{p}|^2} - \frac{f^2\,k^2\,x}{|\mathbf{k}-\mathbf{p}|^2} - \frac{f^2\,p^2\,x}{|\mathbf{k}-\mathbf{p}|^2} + \frac{8\,f^2\,k\,p\,x^2}{7\,|\mathbf{k}-\mathbf{p}|^2}\right),$$

$$(3,3): \left(-\frac{f^3\,k^3}{2\,p\,|\mathbf{k}-\mathbf{p}|^2} - \frac{f^3\,k\,p}{2\,|\mathbf{k}-\mathbf{p}|^2} + \frac{f^3\,k^2\,x}{|\mathbf{k}-\mathbf{p}|^2}\right),$$

$$(4,0): \left(\frac{3\,f^2\,p^2}{7\,|\mathbf{k}-\mathbf{p}|^2} - \frac{f^2\,k\,p\,x}{2\,|\mathbf{k}-\mathbf{p}|^2} - \frac{f^2\,p^3\,x}{2\,k\,|\mathbf{k}-\mathbf{p}|^2} + \frac{4\,f^2\,p^2\,x^2}{7\,|\mathbf{k}-\mathbf{p}|^2}\right),$$

$$(4,2): \left(\frac{f^3\,k^2}{|\mathbf{k}-\mathbf{p}|^2} + \frac{f^3\,p^2}{|\mathbf{k}-\mathbf{p}|^2} - \frac{2\,f^3\,k\,p\,x}{|\mathbf{k}-\mathbf{p}|^2}\right),$$

$$(5,1): \left(-\frac{f^3\,k\,p}{2\,|\mathbf{k}-\mathbf{p}|^2} - \frac{f^3\,p^3}{2\,k\,|\mathbf{k}-\mathbf{p}|^2} + \frac{f^3\,p^2\,x}{|\mathbf{k}-\mathbf{p}|^2}\right).$$

In the end, we write the expansion for the terms of M_{12} computed using the same approach used for M_{13}^B and M_{22}^B, as discussed in Sec. 3.5. We start with the expansion needed for M_{12}^A.

For b_1: (B.0.25)

$$(0,2): \Big(\frac{f\,k^2}{2\,|\mathbf{k}-\mathbf{q}|^2}\Big),$$

$$(1,1): \Big(-\frac{f\,k\,q}{2\,|\mathbf{k}-\mathbf{q}|^2} + \frac{f\,k}{2\,q}\Big).$$

For the term with no bias: (B.0.26)

$$(2,2): \Big(\frac{f^2k^2}{2\,|\mathbf{k}-\mathbf{q}|^2} - \frac{f^2k^2}{|\mathbf{k}-\mathbf{q}|^2}\Big),$$

$$(1,3): \Big(\frac{f^2k^3}{2\,|\mathbf{k}-\mathbf{q}|^2\,q}\Big).$$

Now, we give the expansion needed for M_{12}^B, that is the expansion of $Z_1(\mathbf{q})Z_1(\mathbf{k}-\mathbf{q})$.

For b_1: (B.0.27)

$$(2,2): \Big(\frac{f\,k^2}{|\mathbf{k}-\mathbf{q}|^2}\Big),$$

$$(1,1): \Big(-\frac{2\,f\,k\,q}{|\mathbf{k}-\mathbf{q}|^2}\Big),$$

$$(2,0): \Big(f + \frac{f\,q^2}{|\mathbf{k}-\mathbf{q}|^2}\Big).$$

For b_1^2: (B.0.28)

$$(1,1): 1.$$

For the term with no bias: (B.0.29)

$$(2,2) : \Big(\frac{f^2k^2}{|\mathbf{k}-\mathbf{q}|^2}\Big),$$

$$(3,1) : \Big(-\frac{2f^2kq}{|\mathbf{k}-\mathbf{q}|^2}\Big),$$

$$(4,0) : \Big(\frac{f^2q^2}{|\mathbf{k}-\mathbf{q}|^2}\Big).$$

Appendix C

Full Fisher Forecast Plots

Here we present the full Fisher plots with all parameters varied in the analysis of the forecast described in Chapter 4.

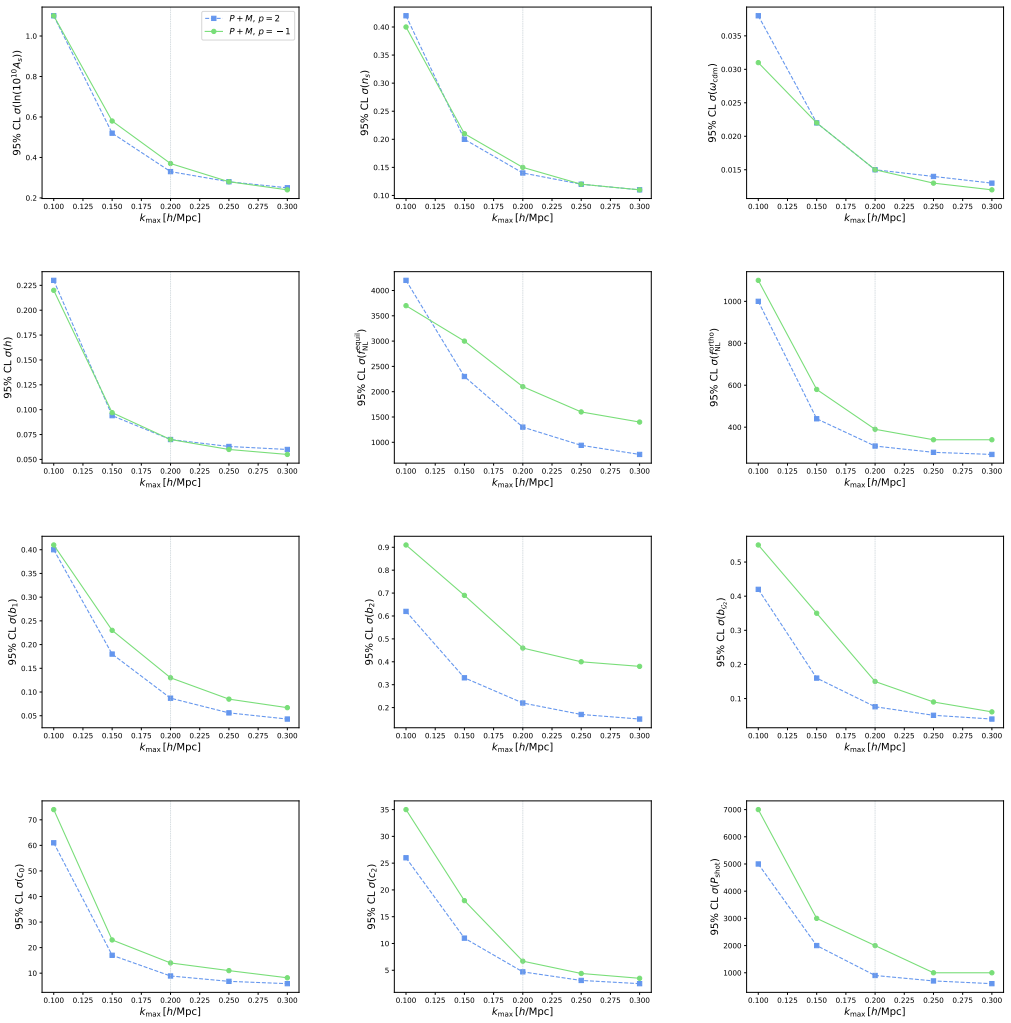

Figure C.1: Full 2σ (95% C. L.) Fisher forecast constraints from galaxies for cosmologies with Non-Local PNG, using the BOSS CMASS volume, number density, and redshift as described in the main text. All relevant parameters are varied in this analysis. The dashed vertical line indicates the maximum wavevector adopted in standard analyses [40].

Bibliography

[1] R. Laureijs et al. Euclid Definition Study Report. *arXiv e-prints*, 2011. [1110.3193].

[2] DESI Collaboration et al. The Completed SDSS-IV Extended Baryon Oscillation Spectroscopic Survey: Final Data Release and Cosmological Implications. *arXiv e-prints*, page arXiv:2302.04130, 2023. [2302.04130].

[3] LSST Science Collaboration. LSST Science Book, Version 2.0. 2009. [0912.0201].

[4] Planck Collaboration et al. Planck 2018 Results. I. Overview and the Cosmological Legacy of Planck. 2019. [1807.06205].

[5] Steven Weinberg. *Gravitation and Cosmology: Principles and Applications of the General Theory of Relativity*. John Wiley and Sons, Canada, 1972.

[6] Scott Dodelson. *Modern Cosmology*. Academic Press, Amsterdam, 2003.

[7] Daniel Baumann. TASI Lectures on Inflation. *arXiv*, 2009. [0907.5424].

[8] Planck Collaboration et al. Planck 2018 results. VI. Cosmological parameters. *arXiv*, 2018. [1807.06209].

[9] David H. Lyth and Andrew R. Liddle. *The Primordial Density Perturbation: Cosmology, Inflation and the Origin of Structure*. Cambridge University Press, Cambridge, UK, 2009.

[10] Edward W. Kolb and Michael S. Turner. *The Early Universe*. Addison-Wesley, Redwood City, CA, 1988.

[11] F. Bernardeau, S. Colombi, E. Gaztanaga, and R. Scoccimarro. Large-Scale Structure of the Universe and Cosmological Perturbation Theory. *Physics Reports*, 367, 2002. [0112551].

[12] Diego Blas, Mathias Garny, and Thomas Konstandin. On the non-linear scale of cosmological perturbation theory. *Journal of Cosmology and Astroparticle Physics*, 2013. [1304.1546].

[13] Tobias Baldauf, Mehrdad Mirbabayi, Marko Simonović, and Matias Zaldarriaga. Equivalence Principle and the Baryon Acoustic Peak. *Physical Review D*, 92(4), 2015. [1504.04366].

[14] Tobias Baldauf, Lorenzo Mercolli, Mehrdad Mirbabayi, and Enrico Pajer. The Bispectrum in the Effective Field Theory of Large Scale Structure. *Journal of Cosmology and Astroparticle Physics*, 2015. [1406.4135].

[15] Mikhail M. Ivanov. Effective Field Theory for Large-Scale Structure: Review of the 1-Loop Power Spectrum. 2022. [2212.08488].

[16] P. J. E. Peebles. *The Large-Scale Structure of the Universe*. Princeton University Press, Princeton, NJ, 1980.

[17] Mikhail M. Ivanov and Sergey Sibiryakov. Infrared Resummation for Biased Tracers in Redshift Space. *Journal of Cosmology and Astroparticle Physics*, 2018(07):053, 2018. [1804.05080].

[18] Chudaykin, Ivanov, Philcox, and Simonović. Non-linear perturbation theory extension of the Boltzmann code CLASS. *arXiv*, 2020. [2004.10607].

[19] Vincent Desjacques, Donghui Jeong, and Fabian Schmidt. Large-Scale Galaxy Bias. *Physics Reports*, 2018. [1611.09787].

[20] Valentin Assassi, Daniel Baumann, Daniel Green, and Matias Zaldarriaga. Renormalized Halo Bias. 2014. [1402.5916].

[21] L. Senatore and M. Zaldarriaga. Redshift Space Distortions in the Effective Field Theory of Large Scale Structures. 2014. [1409.1225].

[22] A. Perko, L. Senatore, E. Jennings, and R. H. Wechsler. Biased Tracers in Redshift Space in the EFT of Large-Scale Structure. 2016. [1610.09321].

[23] J. C. Jackson. Fingers of God: A critique of Rees' theory of primordial gravitational radiation. *Mon. Not. Roy. Astron. Soc.*, 1972. [0810.3908].

[24] M. Schmittfull, M. Simonović, V. Assassi, and M. Zaldarriaga. Modeling Biased Tracers at the Field Level. *Phys. Rev. D*, 100, 2019. [1811.10640].

[25] Mikhail M. Ivanov, Oliver H. E. Philcox, Giovanni Cabass, Takahiro Nishimichi, Marko Simonović, and Matias Zaldarriaga. Cosmology with the Galaxy Bispectrum Multipoles: Optimal Estimation and Application to BOSS Data. *Physical Review D*, 107(8), 2023. [2302.04414].

[26] L. Senatore, K. M. Smith, and M. Zaldarriaga. Non-Gaussianities in Single Field Inflation and their Optimal Estimation. *JCAP*, 01:028, 2010. [0905.3746].

[27] C. Cheung, P. Creminelli, A. L. Fitzpatrick, J. Kaplan, and L. Senatore. The Effective Field Theory of Inflation. *JHEP*, 03:014, 2008. [0709.0293].

[28] Y. Akrami and others (Planck Collaboration). Planck 2018 results. IX. Constraints on primordial non-Gaussianity. *Astron. Astrophys.*, 641:A9, 2020. [1905.05697].

[29] Planck Collaboration. Planck 2018 results. X. Constraints on inflation. *Astron. Astrophys.*, 641:A10, 2020. [1807.06211].

[30] Fabian Schmidt and Marc Kamionkowski. Halo Clustering with Non-Local Non-Gaussianity. *Phys. Rev. D*, 82:103002, 2010. [1008.0638].

[31] H. Gil-Marín, J. Noreña, L. Verde, W. J. Percival, C. Wagner, M. Manera, et al. The power spectrum and bispectrum of SDSS DR11 BOSS galaxies - I. Bias and gravity. *Mon. Not. Roy. Astron. Soc.*, 451:539, 2015. [1407.5668].

[32] E. Massara, F. Villaescusa-Navarro, S. Ho, N. Dalal, and D. N. Spergel. Using the Marked Power Spectrum to Detect the Signature of Neutrinos in Large-Scale Structure. *arXiv e-prints*, 2020. [2001.11024].

[33] M. White. A marked correlation function for constraining modified gravity models. *JCAP*, 11:057, 2016. [1609.08632].

[34] E. Massara, F. Villaescusa-Navarro, C. Hahn, M. M. Abidi, M. Eickenberg, S. Ho, et al. Cosmological Information in the Marked Power Spectrum of the Galaxy Field. *Astrophys. J.*, 951:70, 2023. [2206.01709].

[35] O. H. E. Philcox, E. Massara, and D. N. Spergel. What does the marked power spectrum measure? Insights from perturbation theory. *Phys. Rev. D*, 102:043516, 2020. [2006.10055].

[36] O. H. E. Philcox, A. Aviles, and E. Massara. Modeling the Marked Spectrum of Matter and Biased Tracers in Real- and Redshift-Space. *JCAP*, 03:038, 2021. [2010.05914].

[37] H. Ebina and M. White. An Analytically Tractable Marked Power Spectrum. *arXiv e-prints*, 2024. [2409.17133].

[38] Marco Marinucci, Gabriel Jung, and Michele Liguori et al. The constraining power of the Marked Power Spectrum: an analytical study. *arXiv e-prints*, 2024. [2411.14377].

[39] J. Clampitt, Y.-C. Cai, and B. Li. Voids in modified gravity: excursion set predictions. *Mon. Not. Roy. Astron. Soc.*, 431:749–766, May 2013. [1212.2216].

[40] M. M. Ivanov, M. Simonović, and M. Zaldarriaga. Cosmological parameters from the BOSS galaxy power spectrum. *JCAP*, 2020:042, 2020. [1909.05277].

[41] G. Cabass, M. M. Ivanov, O. H. E. Philcox, M. Simonović, and M. Zaldarriaga. Constraints on Single-Field Inflation from the BOSS Galaxy Survey. *Phys. Rev. Lett.*, 129:021301, 2022. [2201.07238].

[42] Gabriel Jung, Andrea Ravenni, Michele Liguori, Marco Baldi, William R. Coulton, Francisco Villaescusa-Navarro, et al. Quijote-PNG: Optimizing the Summary Statistics to Measure Primordial Non-Gaussianity. *The Astrophysical Journal*, 976(1):109, 2024. [2403.00490].

[43] Anton Chudaykin and Mikhail M. Ivanov. Measuring neutrino masses with large-scale structure: Euclid forecast with controlled theoretical error. *JCAP*, 12:034, 2019. [1907.06666].

[44] Francisco Villaescusa-Navarro, ChangHoon Hahn, and et al. Elena Massara. The Quijote Simulations. *The Astrophysical Journal Supplement Series*, 250(2):2, 2020. [1909.05273].

[45] William R. Coulton, Francisco Villaescusa-Navarro, Drew Jamieson, Marco Baldi, Gabriel Jung, Dionysios Karagiannis, Michele Liguori, Licia Verde, and Benjamin D. Wandelt. Quijote-PNG: Simulations of Primordial Non-Gaussianity and the Information Content of the Matter Field Power Spectrum and Bispectrum. *The Astrophysical Journal*, 943(1):64, 2023. [2206.01619].

[46] M. Crocce, S. Pueblas, and R. Scoccimarro. Transients from Initial Conditions in Cosmological Simulations. *Mon. Not. Roy. Astron. Soc.*, 373:369–381, 2006. [0606505].

[47] Roman Scoccimarro, Lam Hui, Marc Manera, and K. C. Chan. Large-scale Bias and Efficient Generation of Initial Conditions for Non-Local Primordial Non-Gaussianity. *Phys. Rev. D*, 85:083002, 2012. [1108.5512].

[48] M. Davis, G. Efstathiou, C. S. Frenk, and S. D. M. White. The Evolution of Large Scale Structure in a Universe Dominated by Cold Dark Matter. *Astrophysical Journal*, 292:371, 1985. Astrophys. J. 292 (1985) 371.

[49] Alan Heavens. Statistical techniques in cosmology. *arXiv e-prints*, 2010. [0906.0664v3].

[50] Victoria Yankelevich and Cristiano Porciani. Cosmological information in the redshift-space bispectrum. *Monthly Notices of the Royal Astronomical Society*, 483(2):2078–2103, 2019. [1807.07076].

[51] Muntazir Mehdi Abidi and Tobias Baldauf. Cubic Halo Bias in Eulerian and Lagrangian Space. *JCAP*, 07:029, 2018. [1802.07622].

[52] Naonori S. Sugiyama, Shun Saito, Florian Beutler, and Hee-Jong Seo. Perturbation theory approach to predict the covariance matrices of the galaxy power spectrum and bispectrum in redshift space. [1908.06234].

[53] Antony Lewis. The real shape of non-Gaussianities. *JCAP*, 10:026, 2011. [1107.5431].

[54] Jessica A. Cowell, David Alonso, and Jia Liu. Hitting the mark: Optimising Marked Power Spectra for Cosmology. *Monthly Notices of the Royal Astronomical Society*, 535(4):3129–3140, 2024. [2409.05695].

[55] Mikhail M. Ivanov, Evan McDonough, and J. Colin Hill et al. Constraining Early Dark Energy with Large-Scale Structure. *Phys. Rev. D*, 102(10):103502, 2020. [2006.11235].

[56] Thomas Flöss, Matteo Biagetti, and P. Daniel Meerburg. Primordial non-Gaussianity and non-Gaussian Covariance. *JCAP*, 10:013, 2022. [2206.10458].

[57] Elena Massara, ChangHoon Hahn, and et al. Eickenberg, Michael. SimBIG: Cosmological Constraints using Simulation-Based Inference of Galaxy Clustering with Marked Power Spectra. *arXiv preprint arXiv:2404.04228*, 2024. [2404.04228].

[58] Marko Simonović, Tobias Baldauf, Matias Zaldarriaga, John Joseph Carrasco, and Juna A. Kollmeier. Cosmological Perturbation Theory Using the FFTLog: Formalism and Connection to QFT Loop Integrals. *arXiv:1708.08130*, 2017. [1708.08130].